

EXPERIMENTAL AND NUMERICAL HYDRODYNAMIC STUDY OF SUBMERGED ICE COLLISION

By

© Subodh Chander

B.Tech, IIT Kharagpur, 2010

A thesis submitted to the
School of Graduate Studies
in partial fulfillment of the requirements for the degree of
Master of Engineering

Faculty of Engineering and Applied Science
Memorial University of Newfoundland
Major: Ocean and Naval Architectural Engineering

October 2015

St. John's, Newfoundland & Labrador, Canada

ABSTRACT

Most of the research done on ice-structure interaction to date deals with the ice at the sea surface. However the majority of ice strengthened regions of ships and offshore structures are well below the waterline. The aim of this research is to examine the mechanics of ice loads caused by submerged ice blocks colliding with the structure. The kinematics of this process is an essential determinant of the energy that is available to drive the ice crushing process during the collision. The present research aims to develop a model to represent the mechanics of such collisions and set a direction for future work. This study includes experimental and numerical components. Various physical experiments have been conducted using a submerged ice model moving solely due to its buoyancy.

Using a high speed camera, the experiments are recorded and analysed to determine the kinematics of collision. These include location, velocity and acceleration of the model ice as a function of time. In parallel, numerical simulations have being conducted using FLOW3D™ software. The results of the experiments are used to validate the numerical model of the underwater collision.

ACKNOWLEDGEMENTS

To begin with this thesis, I would like to express my sincerest appreciation to my supervisor's Dr. Ayhan Akinturk and Dr. Bruce Colbourne for their excellent support, direction, and guidance. I am also thankful to STEPS² program for their generous financial support.

This thesis would be impossible without the help and support from a few great people. I would also like to state my great gratitude to the following:

Dr. Claude Daley, professor at MUN, for bringing me to this outstanding university.

Trevor Clark, Lab Technologist Ocean and Architectural Engineering for his technical support and assistance while conducting my experiments.

Matt Curtis, Lab. Technologist Ocean and Naval Architectural/Civil Engineering for his advice on data acquisition systems and high speed cameras.

Dr. Mike Hinckey for his expert advice on FLOW3D™ software.

Finally, I would like to thank my family for their understanding and patience throughout my entire time at Memorial University.

Table of Contents

ABSTRACT	i
ACKNOWLEDGEMENTS	iii
Table of Contents	iv
List of Figures	vii
List of Symbols, Nomenclature or Abbreviations	xii
Chapter 1 - Introduction	1
1.1: Scope of work.....	3
1.2: Literature Review and Theory.....	3
1.3: Ship Icebreaking Mechanism.....	4
1.4: Collision Physics.....	6
1.5: Equation of Motion.....	8
1.6: Added mass numerical investigation.....	10
1.7: Added mass Coefficent for a spherical particle near a wall using potential theory..	14
1.8: Immersed collision	19
1.9: Literature Summary and Problem Statement.	22
Chapter 2 – Experimental model.....	23
2.1: Ship model.....	23
2.2: Dynamic load cell	25

2.3: Load cell unit.....	26
2.4: Aluminium plate frequency response	27
2.5: Ice Model	34
2.6: Release Mechanism	35
2.7: Lab View.....	36
Chapter 3 – Image Analysis.....	37
3.1: High speed video...	37
3.2: Error estimation arising due to intrinsic, extrinsic and lens distortion parameters of camera...	41
Chapter 4 – Results.....	44
4.1: Displacement and velocity of Ice model from Matlab data.....	44
a) Depth 2cm release test.....	44
b) Depth 3.5cm release test.....	45
c) Depth 5cm release test.....	46
d) Depth 6.5cm release test.....	46
e) Depth 8cm release test.....	47
f) Depth 10cm release test.....	47
4.2: Experimental data analysis.....	49
4.2.1: Depth 2 cm Analysis.	50
4.2.2:Depth 3.5 cm Analysis.....	53
4.2.3: Depth 5cm Analysis.....	55

4.2.4: Depth 6.5cm Analysis.....	57
4.2.5: Depth 8cm Analysis.....	59
4.2.6: Depth 10cm Analysis.....	61
4.3: Error Analysis.....	65
4.3: Coefficient of Restitution.....	68
Chapter 5 – Numerical Model.....	71
5.1: Meshing.....	71
5.2: GMO Model.....	73
5.3: VOF Method.....	74
5.4: FAVOR (Fractional area volume obstacle representation).....	75
5.5: Boundary conditions.....	76
5.6: Comparison of FLOW3D™ results with experimental data.....	78
Chapter 6 – Conclusion and reccomendations.....	82
Bibliography	85
References.....	89
Appendices	
Appendix A Matlab Code For Image Processing	92
Appendix B Matlab code to filter data	95
Appendix C Camera calibration code.....	98

List of Figures

Figure 1.1: Ice breaking process.....	5
Figure 1.2: Hydrodynamic forces on spherical model.....	7
Figure 1.3: Added mass coefficient of sphere near a wall by H. Chung & S.S. Chen.....	16
Figure 1.4: Theoretical and Experimental added mass coefficient, Cm by Wallis S.Hamilton and Gerald L.Courtney	17
Figure 1.5: Immersed Collision.....	19
Figure 1.6: Effective coefficient of restitution.....	21
Figure 2.1: Lexan ship model with aluminium frame	23
Figure 2.2: Hatch arrangement for bottom plate.....	24
Figure 2.3: Dynamic Load cell DLC101.....	25
Figure 2.4: Load cell unit.....	27
Figure 2.5: Flowchart to determine the dimension of the aluminum plate used for ice collision.....	29
Figure 2.6: Aluminium plate mesh with a load cell for Modal Analysis.....	30
Figure 2.7: Eigen frequencies of Aluminium plate with different mesh density.....	31
Figure 2.8: Eigen frequencies of Aluminum Plate.....	32
Figure 2.9: Ice Model.....	34
Figure 2.10: Ice model release mechanism.....	35
Figure 2.11: LabVIEW.....	36
Figure 3.1: Calibration for the high speed video recording.....	37

Figure 3.2: Conversion to Binary Image in Matlab™.....	39
Figure 3.3: Displacement pixels: v/s time sec.....	40
Figure 3.4: Checkered pattern used for calibration of camera.....	41
Figure 3.5: Matlab analysis of calibration images from camera.....	42
Figure 3.6: Mean error arising due to camera parameters in pixels.....	43
Figure 4.1: Force, displacement experimental data 2cm depth.....	44
Figure 4.2: Force, displacement experimental data 3.5cm depth.....	45
Figure 4.3: Force, displacement experimental data 3.5cm depth.....	46
Figure 4.4: Force, displacement experimental data 6.5cm depth.....	46
Figure 4.5: Force, displacement experimental data 8cm depth.....	47
Figure 4.6: Force, displacement experimental data 10cm depth.....	47
Figure 4.7: Data Filtering using moving average.....	49
Figure 4.8: Displacement, Velocity before collision for 2cm depth.....	49
Figure 4.9: Ca added mass coefficient before collision for 2cm depth.....	51
Figure 4.10: Impact force, Velocity during collision for 2cm depth.....	52
Figure 4.11: Ca added mass coefficient during collision for 2cm depth.....	52
Figure 4.12: Displacement, Velocity before collision for 3.5cm depth.....	53
Figure 4.13: Ca added mass coefficient before collision for 3.5cm depth.....	53
Figure 4.14: Impact force, Velocity during collision for 3.5cm depth.....	54
Figure 4.15: Ca added mass coefficient during collision for 3.5cm depth.....	54
Figure 4.16: Displacement, Velocity before collision for 5cm depth.....	55
Figure 4.17: Ca added mass coefficient before collision for 5cm depth.....	55

Figure 4.18: Impact force, Velocity during collision for 5cm depth.....	56
Figure 4.19: Ca added mass coefficient during collision for 5cm depth.....	56
Figure 4.20: Displacement, Velocity before collision for 6.5cm depth.....	57
Figure 4.21: Ca added mass coefficient before collision for 6.5cm depth.....	57
Figure 4.22: Impact force, Velocity during collision for 6.5cm depth.....	58
Figure 4.23: Ca added mass coefficient during collision for 6.5cm depth.....	58
Figure 4.24: Displacement, Velocity before collision for 8cm depth.....	59
Figure 4.25: Ca added mass coefficient before collision for 8cm depth.....	59
Figure 4.26: Impact force, Velocity during collision for 8cm depth.....	60
Figure 4.27: Ca added mass coefficient during collision for 8cm depth.....	60
Figure 4.28: Displacement, Velocity before collision for 10cm depth.....	61
Figure 4.29: Ca added mass coefficient before collision for 10cm depth.....	61
Figure 4.30: Impact force, Velocity during collision for 10cm depth.....	62
Figure 4.31: Ca added mass coefficient during collision for 10cm depth.....	62
Figure 4.32: Reynolds Number against time.....	63
Figure 4.33: Added mass coefficient Ca values during collision.....	64
Figure 4.34 Added mass coefficient comparison for tests at 2cm depth.....	65
Figure 4.35 Mean value of added mass for tests at 2cm depth.....	66
Figure 4.36 Added mass coefficients comparison for tests at 5cm depth.....	67
Figure 4.37 Mean value of added mass for tests at 5cm depth.....	67
Figure 4.38: Effective Coefficient of Restitution.....	68

Figure 4.39: Effective Coefficient of restitution of ice model versus Stokes number.....	69
Figure 5.1: Mesh for the underwater ice collision with the aluminum plate.....	72
Figure 5.2: Boundary Conditions.....	76
Figure 5.3: Flow3d TM simulation of submerged ice sphere colliding with a solid aluminum plate.....	77
Figure 5.4: Flow3d TM / experimental displacement, velocity data comparison for 2cm depth.....	78
Figure 5.5: Flow3d TM /experimental displacement, velocity data comparison for 3.5cm depth.....	79
Figure 5.6: Flow3d TM /experimental displacement, velocity data comparison for 5cm depth.....	80

List of Symbols, Nomenclature or Abbreviations

M_{add}	Added mass
T_k	Kinetic energy of fluid
U_i	Cartesian components of fluid velocity
ρ	density of water
ν	kinematic viscosity
T	characteristic time
L	characteristic length
Sl	Strouhal number = $\frac{L}{T*U}$
Re	Reynold's number = $\frac{U*L}{\nu}$
Ro	Roshko number = $Sl * Re = \frac{L^2}{T*\nu}$
μ	dynamic viscosity
F_v	viscous force
F_a	added mass force
F_h	history force
C_v	drag coefficient
R	radius of spherical model
A_o	amplitude
ω	angular velocity
A_c	acceleration number

F_D	drag force
m_p	mass of particle
m_f	mass of fluid displaced by particle
St	stokes number
e	coefficient of restitution
kHz	kilohertz
\vec{T}_G	Torque
[J]	Moment of inertia
\vec{F}_G	Gravitational force.
\vec{F}_H	Hydraulic force
\vec{F}_c	Net control force
\vec{F}_{ni}	Net non-inertial force
FAVOR	Fractional Area Volume Obstacle Representation
GMRES	Generalized Minimal Residual solver
VOF	Volume of fluid
GMO	General moving object
FPS	Frame per second
BBO	Basset-Boussinesq-Oseen

Chapter 1 Introduction

On September 17, 2014, sea ice extent dropped to 5.02 million square kilometers (1.94 million square miles). This appears to have been the lowest extent of the year. In response to the setting sun and falling temperatures, ice extent will now climb through autumn and winter. However, a shift in wind patterns or a period of late season melt could still push the ice extent lower. The minimum extent was reached two days later than the 1981 to 2010 average minimum date of September 15.” [National Snow and Ice Data center]

Since the onset of the Industrial revolution we have seen a rise in greenhouse gases. This has been one of the causes of global warming and melting of arctic ice. Although reduction in ice is a concern, it has led to more activities in the Arctic. The melting ice has made it more feasible to use the North West passage as a profitable shipping route. The North West passage route reduces the distance and draft restrictions for ships sailing to Europe/Asia, compared to the Panama Canal route. This means more cargo carrying capacity, due to increased draft and lesser greenhouse gases due to less fuel consumption.

One example has been set by MS Nordic Orion, a 225m ice strengthened bulk carrier, loaded with coal set to sail from Port Metro Vancouver, Canada to Port of Pori, Finland via North West Passage. This route led to the fuel savings of around \$80,000 and shipping of 15,000 tons extra cargo.

In addition to the shorter shipping route, the Arctic holds a lot of untapped natural resources. In recent years we have seen offshore activities in the region. With the increased interest in arctic shipping and exploration activities, an increase in research on ice

strengthening of ship and offshore structures is warranted. Although most of the research is focussed on ice loads at the sea surface, much less work has been done on loads caused by submerged ice blocks that pass under the hull of floating ships and structures. Even the ship damage data which is available is limited as far as this issue is concerned.

This thesis describes a research study intended to throw some light on the issue of submerged ice collisions. The main focus of the study is to determine the mechanics of ice loads caused by submerged ice collisions, which can further be used to determine the structural response during a collision. The major part of the work studied here is the kinematics of submerged ice pieces during a collision. The kinematics is an essential determinant of the energy that is available to drive the ice crushing process during the collision.

The present research aims to develop a model to represent the mechanics of such collisions and set a direction for future work. The study includes experimental and numerical modeling of the collision process for simplified geometries. Various physical experiments have been conducted using a submerged model ice piece moving solely due to its buoyancy. Using a high speed camera, the experiments were recorded and analyzed to determine the kinematics of collision. These include location, velocity and acceleration of the model ice as a function of time. In parallel, numerical simulations have been conducted using FLOW 3D™ software. The results of the experiments were used to validate a numerical model of the underwater ice collision. The study also considers the effects of the coefficient of restitution which is an important parameter of collision. The results show that added mass plays an important role during the underwater impact collisions.

1.1 Scope Of Work.

This research involves experimental study of submerged ice collision during ice breaking. A model ship (1.82m in length, 0.3m in breadth and 0.25 cm in height) was fabricated with the load cell attachments to record the ice loads.

Although there is no full scale or experimental data available for submerged ice collision, we have used previous research on underwater collision of simple geometrical objects as a starting point. The idea is to find the kinematics of collision and determine the added mass of the accelerating ice model. Knowing the actual value of added mass helps in explaining the real energy transfer to the structure during collision.

1.2 Literature Review and Theory.

A review of all the current and past literature in the area of ice-ship collisions, has revealed that there have been almost no specific studies on the hydrodynamics of submerged ice collisions with the ship's hull. This lack of work, as well as the practical importance of the subject was the main reason for performing this research. The literature pertaining to design of ice class vessels, collision and impact mechanics, hydrodynamics of underwater collision, added mass effects (wet collision and its effects on coefficient of restitution) and computational fluid dynamics were reviewed and adapted as required.

The available literature deals with head on ice-ship collisions, ice collision forces can be determined by energy considerations. Claude Daley (Daley, 1999) proposed the Indentation energy functions for various geometrical shapes ,by using pressure area relationships.

Due to the availability of literature on the study of hydrodynamics of spheres in fluids, we have used spherical shape for the ice model. Since the collision occurs in the fluid, buoyancy force and weight remains constant (assuming there is no loss of mass during the collision) whereas damping and added mass forces vary with time. The added mass term is proportional to the acceleration of the model while the damping term is proportional to the velocity. An intial approach to handle added mass and damping forces was discussed by Lamb (Lamb, 1932), (Milne-Thomson, 1968) using potential flow theory, where the image method was used to account for the presence of wall. In this approach the fluid flow is considered inviscid and irrotational.

1.3 Ship Icebreaking Mechanism

Ice breaking ships generally force the surface ice downward to break in flexure. Normally a ship breaks ice steadily and continuously in operating conditions. But as the ice thickness increases the ship changes to backing and ramming mode.

As the bow rams against the ice edge it pushes it down , the water below is pressed quickly and rushes out of the way, generating high pressure. The broken ice pieces slides down the hull as the ship moves forward.

The forces experienced by a ship transiting in a level ice can be divided into four categories (D.B. Colbourne, 1989):

- a) Deforming, crushing , bending and fracturing of ice to break the main ice sheet into smaller pieces. These forces depends on the the material strength properties of ice.
- b) Moving the newly separated ice pieces as the ship moves forward. This involves submerging and moving ice pieces out of the way, by pushing them down and to the sides.

Since the ice blocks are fully submerged in the fluid it involves hydrodynamic forces in addition to buoyancy and inertia. This is discussed in detail in this thesis.

- c) As the ship proceeds in a field of broken ice pieces, its hydrodynamic drag forces which include skin friction, form drag and wave making resistance are influenced by the presence of ice pieces moving around it, since the flow around the hull is effected by the presence of ice pieces.
- d) Forces arising due to friction between hull and ice. This influences breaking forces, clearing forces and hydrodynamic forces. A rough high friction hull experiences higher forces compared to a smooth hull. The hull friction is further increased with the service life due to the abrasive nature of ice.

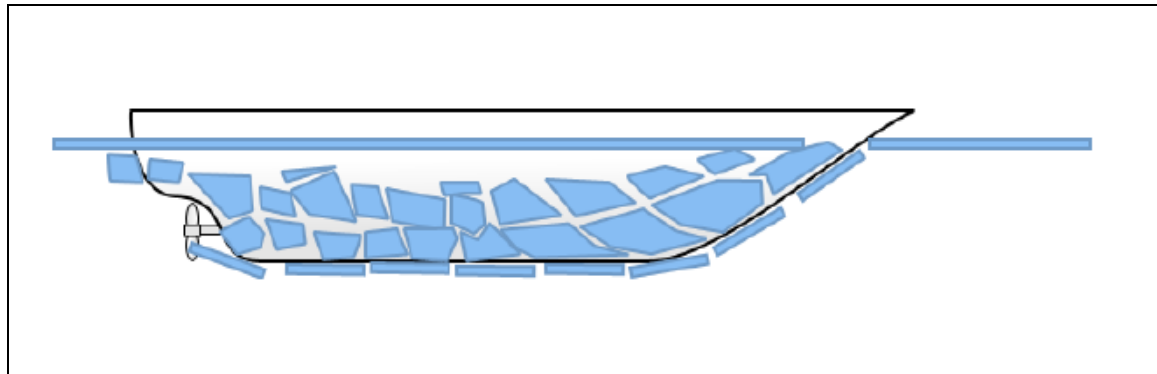


Fig.1.1 Ice breaking process.

1.4 Collision Physics

Collisions and impact events between ships and other objects account for the major part of ship/offshore damages. This may also include grounding. This makes the study of collision an important area of research in naval architecture. In the case of ships sailing in ice infested regions the knowledge of ice loads plays a crucial role in determining the designed structural strength of a ship, although not much information is available on underwater ice loads on hull.

The impact during ice block collision with a ship can be divided into two cases (Pedersen and Zhang, 1998):

- External Dynamics.
- Internal Mechanics.

The external dynamics account for the kinematics of the collision, the energy dissipated during the collision, the effect of surrounding water on the collision and the rigid motions. The internal mechanics deals with the structural response and the damage during the collision. In other words external dynamics determines the ice loads on the structure. Internal mechanics uses the predicted ice loads to determine the structural response of the structure during impact. These two cases of collision can be studied independently or coupled depending on the analysis.

This thesis focuses completely on the external dynamics of collision. This includes the kinematics of the ice block, the hydrodynamic forces during impact, and the effect of the surrounding fluid on the coefficient of restitution, etc.

To simplify the terms in the equation of motion we are using a spherical ice model to study the submerged ice collision. The spherical ice model in the close proximity to the model ship is released to determine the impact forces arising due to collision. The impact force is influenced by the presence of surrounding fluid.

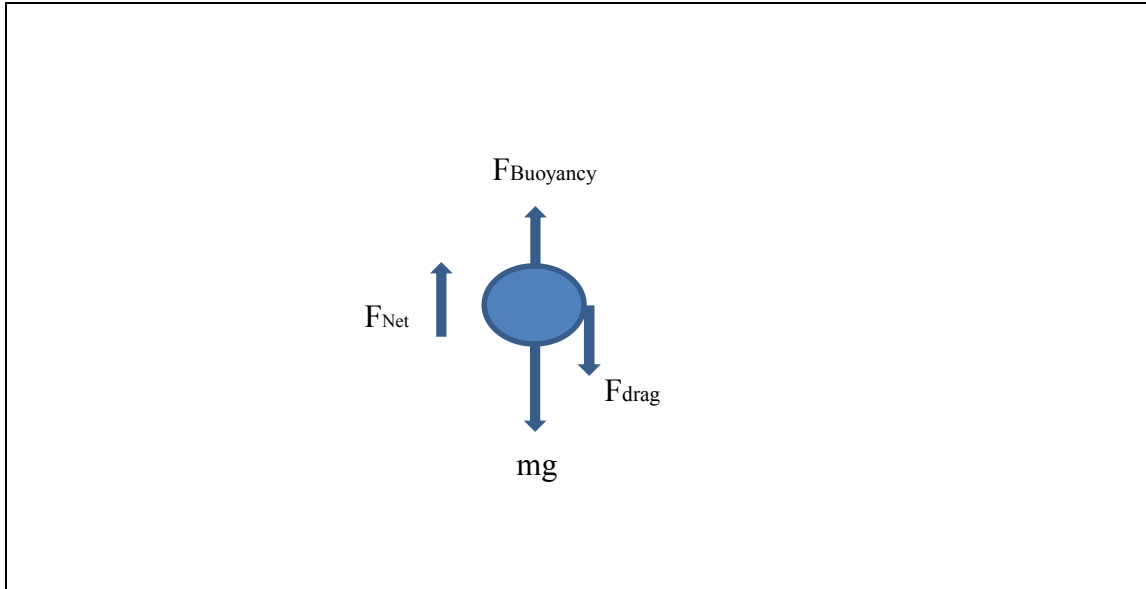


Fig 1.2 Hydrodynamic forces on spherical model.

1.5 Equation of Motion.

For an object accelerating through a stationary fluid apart from buoyancy and drag force, the missing force is the inertia of the fluid being accelerated out of the way of the moving body. Whereas in case of a fluid flow over a stationary object it is the difference of the inertia force of fluid with and without the object. Initial work in this area by Du Buat (Du Buat,1984) shows that the inertial fluid force is proportional to the acceleration of the moving object. He proposed that in order to account for these forces, an additional mass M_{add} has to be added to the mass M , undergoing acceleration in the fluid. Although the term added mass maybe misleading, as there is no actual addition or subtraction of mass to the moving body but the change in inertia or change in kinetic energy of the control volume, due to the motion, which can be either negative or positive. It should be noted that “Added mass” is just an approach to handle this additional force arising due to the fluid acceleration. It plays an important role in accelerating, non-uniform motion resulting in fluid acceleration around the body.

The simplest way to look at added mass is the amount of work done to change the kinetic energy of the fluid. [Lamb,1945]

$$T = \frac{\rho}{2} \int_V (u_1^2 + u_2^2 + u_3^2) dV \quad (1.1)$$

Where $u_i (i = 1,2,3)$ represents the Cartesian components of the fluid velocity and V is the entire domain or volume of fluid. Although this approach does not take into account the effects of viscosity and compressibility of the fluid.

The added mass force in a particular direction can be due to the motion of the object in different directions (translational and rotational). This makes the calculation of added mass for an arbitrary body a complex problem. Considering all the six degrees of freedom the added mass matrix can have 6x6 terms, that is 36 scalars. This problem can be reduced by using geometric symmetry and this is the primary reason to model the ice as a sphere.

Considering the effects of viscosity and compressibility of the fluid, the major effect is the formation of wake, which interacts with the drag and inertial forces and makes it more difficult to accurately calculate the forces. The added mass varies with the shape and volume of the wake as well as its rate of change [Sarpkaya,1975]

The wake generated due the motion has more influence on lighter bodies (density of ice < density of water). This introduces some lateral motion in a free rising object.

1.6 Added Mass Numerical Investigation.

In 1851 Stokes investigated the simple harmonic motion of sphere oscillating in a fluid. He omitted the convective terms in Navier-Stokes equation and derived the force expression. The Navier-Stokes equation is Newton's second law applied to fluid dynamics. Like Newton's second law it obeys the conservation of momentum.

Let the relative velocity of the fluid due to the moving object be v , dynamic viscosity η , and the fluid density by ρ . The external forces acting on fluid are denoted by f . We can write Navier-Stokes equation for an incompressible fluid as:

$$\frac{\delta \vec{v}}{\delta t} * \rho + \rho \vec{v} \nabla \vec{v} = -\nabla p + \eta \nabla^2 \vec{v} + \vec{f} \quad (1.2)$$

To better understand the problem we will write the Navier-Stokes in non-dimensional form. Assuming the characteristic length as L , characteristic time as T , which is the fastest time scale in the problem the inherent nature of fluid to change or the time taken to change the boundary conditions and U as a characteristic velocity.

$$v' = \frac{v}{U}, p' = \frac{p}{\rho U^2}, \nabla' = L \nabla, t' = \frac{t}{T}$$

We can now write the non-dimensionalized Navier-Stokes equation as:

$$\begin{aligned} \frac{L}{T * U} \frac{\delta v'}{\delta t'} + v' * \nabla' v' &= -\nabla' p' + \frac{v}{L * U} \nabla'^2 v' + f_{ext} \\ Sl \frac{\delta v'}{\delta t'} + v' * \nabla' v' &= -\nabla' p' + \frac{1}{Re} \nabla'^2 v' + f_{ext} \end{aligned}$$

$$\underbrace{\frac{Ro}{\delta t'} \frac{\delta v'}{\delta t'} + \underbrace{Re \ v' * \nabla' v'}_{convective term}}_{Inertial terms} = - \underbrace{Re \ \nabla' p'}_{pressure term} + \underbrace{\nabla'^2 v'}_{viscous term} + f_{ext} \quad (1.3)$$

Where Strouhal number $Sl = \frac{L}{T^* U}$, Reynold's number $Re = \frac{U^* L}{v}$, Roshko number $Ro =$

$$Sl * Re = \frac{L^2}{T^* v}$$

For very small values of Strouhal number the flow is steady and the unsteady terms can be neglected. If the Reynolds number is small the inertial terms can be neglected and the flow is dominated by the viscous term. If the Reynolds number is high but the Strouhal number is low, only the convective term has to be included. Both these terms are non-linear in nature. In cases of high Reynolds number and high Strouhal number both unsteady and convective terms have to be included.

Later Basset (1888), Boussinesq (1885) and Oseen (1927) studied the rectilinear motion of a sphere released in water. Although they also omitted the convective terms in the Navier-Stokes equations, they introduced an integral term, proving that the instantaneous force not only depends on instantaneous acceleration and velocity but also on the history of the acceleration.

$$-F = 6\pi R \mu V + \frac{1}{2} \left(\frac{4}{3} \pi R^3 \right) \rho a + 6R^2 (\pi \mu \rho)^{\frac{1}{2}} \int_0^t \frac{a(t')}{(t-t')^{\frac{1}{2}}} dt' \quad (1.4)$$

μ = Viscosity of the fluid

V = Velocity of the sphere

R= Radius of the sphere

a=Acceleration of the sphere

The first term on right hand side represents (F_V) viscous force, the second term represents the forces due to acceleration of the fluid also known as added mass (F_A) and the third term represents the history forces (F_H).

Since the convective terms are neglected, the motion corresponds to low Reynolds number.

Odar & Hamilton (Fuat Odar & Wallis S.Hamilton, 1964) further extended BBO equation to include convective terms. They introduced added mass force as $F_A = C_A \frac{4}{3} \pi R^3 \rho a$,

where the value of C_A was determined experimentally, and drag force as $F_V = \frac{1}{2} C_V \pi R^2 \rho |V| V$, where C_V is drag coefficient. C_V is also determined experimentally. C_H is the history force coefficient which was also determined experimentally.

So the equation (1.4) can be written:

$$-F = \frac{1}{2} C_V \pi R^2 \rho |V| V + C_A \frac{4}{3} \pi R^3 \rho a + C_H R^2 (\pi \mu \rho)^{\frac{1}{2}} \int_0^t \frac{a(t')}{(t-t')^{\frac{1}{2}}} dt' \quad (1.5)$$

For a sphere oscillating in simple harmonic motion $x = A_o \cos \omega t$, and amplitude of A_o in a viscous liquid, the final expression can be written as:

$$\begin{aligned} F = C_V \pi R^2 \frac{1}{2} \rho A_o^2 \omega^2 |\sin \omega t| \sin \omega t + C_A \frac{4}{3} \pi R^3 \rho A_o \omega^2 \cos \omega t \\ + C_H \pi R^2 \left(\frac{1}{2} \mu \rho\right)^{\frac{1}{2}} A_o \omega^{\frac{3}{2}} (\cos \omega t + \sin \omega t). \end{aligned} \quad (1.6)$$

*This equation excludes the buoyancy term and is valid for low Reynolds number (Re < 62).

$$C_A = 2.1 - \frac{0.132}{A_C^2 - 0.12} \quad \text{Where } A_C \text{ is the acceleration number defined by: } A_C = \frac{2U^2}{a \left| \frac{du}{dt} \right|}$$

C_H is determined experimentally as : $C_H = 0.48 - \frac{0.32}{(A_C+1)^3}$ (Fuat Odar & Wallis S.Hamilton, 1964).

From the Navier-Stokes equation we know that the effect of convective inertia increases with increase in Reynolds Number. Although analytic expressions are not known for Reynolds number but C_d as a function of Reynolds number is well documented, for a range of Reynolds number for a sphere moving in a fluid [Clift et al., 1978].

$$\text{So we can write the steady drag as: } F_D = -6\pi R \mu_f U \emptyset(Re) \quad (1.7)$$

Where $\emptyset(Re)$ is a function of Reynolds number.

From the experimental tests it was found that the Reynolds number is within the range of $3*10^5$.

$$\emptyset = \left(1 + 0.15 Re_p^{0.687}\right) + \frac{1.75 \times 10^{-2} Re_p}{1 + 4.25 \times 10^4 Re_p^{-1.16}} \quad \forall Re_p < 3 \times 10^5 \quad (1.8)$$

Including the effect of buoyancy force at higher Reynolds number (M.Rostami, A.Ardeshit, G.Ahmadi and P.J.Thomas, 2006).

$$m_p \frac{dv}{dt} = -6\pi R \mu_f V \emptyset(Re) - \frac{1}{2} C_A m_f \frac{dv}{dt} + (m_p - m_f)g - 6R^2 C_H \sqrt{\pi \mu_f \rho_f} \int_0^t \frac{\frac{dv}{d\tau}}{\sqrt{(t-\tau)}} d\tau. \quad (1.9)$$

Apart from the effects of buoyancy, weight ,drag and added mass forces Eq(1.9), also includes the effects of the history of acceleration on the instantaneous force. Although history force values are significant only for low reynolds number flows. As the velocity increases the effects of history forces becomes negligible.

During the time of collision an extra term $F_I(t)$, impact force is introduced to include the effects of impact force on the model. So the Eq (1.9) can be rewritten as :

$$m_p \frac{dv}{dt} - F_I(t) = -6\pi R \mu_f V \emptyset(Re) - \frac{1}{2} C_A m_f \frac{dv}{dt} + (m_p - m_f)g - 6R^2 C_H \sqrt{\pi \mu_f \rho_f} \int_0^t \frac{\frac{dv}{d\tau}}{\sqrt{(t-\tau)}} d\tau \quad (1.10)$$

1.7 Added mass Coefficent for a spherical particle near a wall using potential theory.

The analytical study using potential flow theory of sphere moving in an unbounded incompressible fluid shows that the added mass coefficient is close to 0.5. The presence of a solid wall leads to an increase of the added mass as the sphere approaches the wall. As a consequence of the added-mass dependence on the distance of the sphere to the wall, a force arises that is proportional to the square of the sphere velocity (Lamb H,1932).

Stokes derived an expression for the fluid potential and calculated the added mass for distances much larger than the sphere radius (Stokes GG, 1843). He considered the motion induced by the sphere in the absence of the wall, the motion induced by the second sphere that is the mirror reflection of the first sphere in the plane of the wall, and the motion induced by the first sphere that compensates the motion of the sphere reflection. Then the three motions were superposed to obtain the result.

Hicks (Hicks WM, 1880) expanded the image method to calculate the added mass of sphere approaching a wall and moving parallel to the wall. He was able to calculate the

velocity field from a sequence of dipoles. For the axissymmetric case he calculated the added mass coefficient of sphere as 0.803.

Davis (A.M.J Davis, 1976) did a numerical study of heaving spheres near a wall. He calculated the added mass using bi-spherical co-ordinate system (μ, η, θ). The velocity potential was defined as an even function of μ .

Cox and Cooker (Simon J. Cox & Mark J. Cooker, 2000) found the velocity potential of an ideal incompressible fluid past a sphere moving in contact with a wall. The sphere was free to move due to the fluid impact force. The unknown function was found numerically to a high degree of accuracy and then a detailed presentation was given of the potential near the sphere. The added-mass coefficient was found to be equal to 0.621. They used matched asymptotic expansions to the problem of sphere separated by a small distance $h \rightarrow 0$ there is a singularity in the fluid velocity near the point of contact. The potential near the point of contact was analysed separately using a theory appropriate to cervices regions.

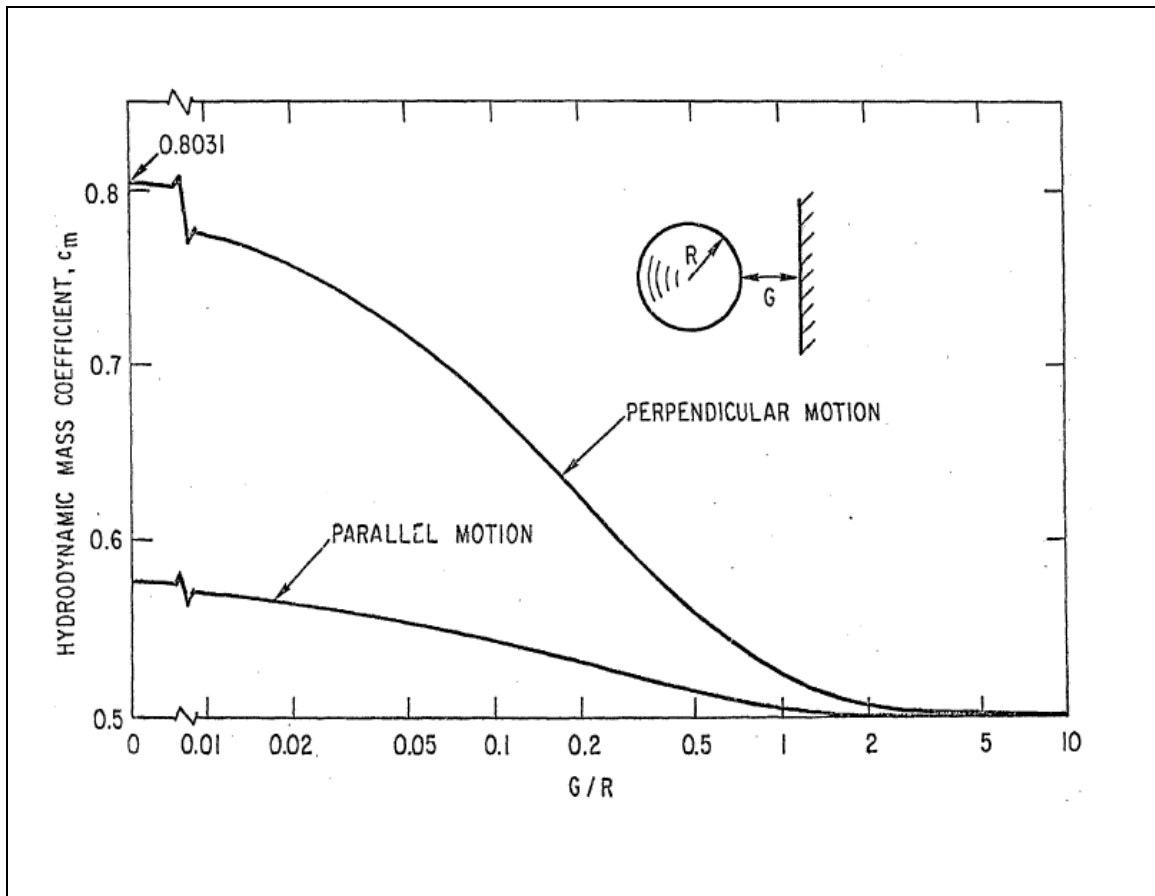


Fig 1.3 Added mass coefficient of sphere near a wall by H. Chung & S.S. Chen.

Chung & Chen (H.Chung & S.S.Chen, 1976) did a numerical study of sphere added mass near the wall, using potential theory. The results showed that the added mass increases as the gap reduces.

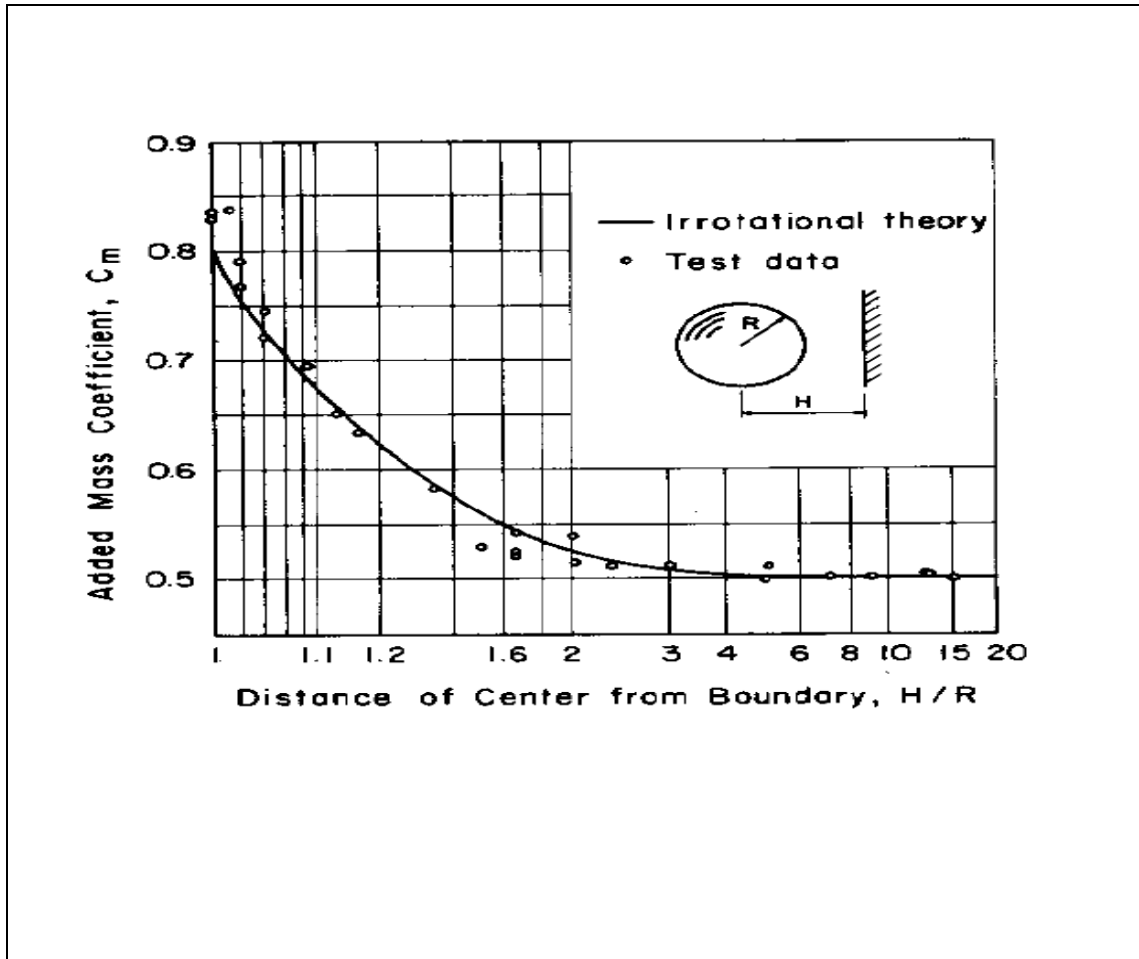


Fig 1.4 Theoretical and Experimental added mass coefficient, C_m by Wallis S.Hamilton and Gerald L.Courtney.

Hamilton and Courtney (Wallis S.Hamilton & Gerald L.Courtney, 1976) conducted a study to compare the theoretical and experimental added mass coefficient of sphere accelerating away from a wall. The theoretical added mass was calculated from irrotational theory. These experiments were conducted at low Reynolds number values in order to maintain a laminar boundary layer. The results shows the amplification of added mass coefficient due

to the presence of a nearby boundary which gradually drops to a constant value of 0.5 as the sphere travels away from the boundary.

Although potential flow theory does not include the characteristics of fluids encountered in real world but these results can be used to determine the deviation from the real experimental data. Since the sphere was completely submerged in the water, away from the free surface and at low Reynolds number the effects of free surface were not included while determining the added mass.

1.8 Immersed Collision.

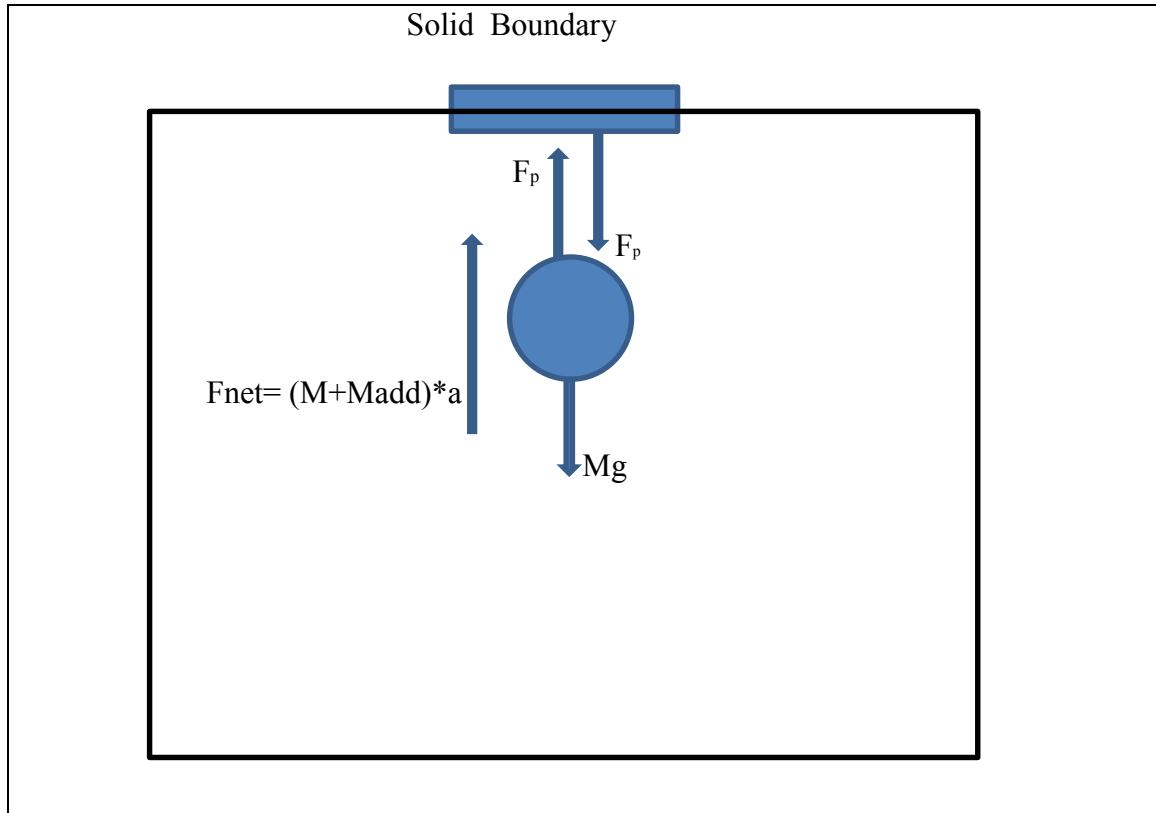


Fig 1.5 Immersed collision.

An elastic collision is usually defined as a compression process followed by a restitution phase. During collision solid deforms and stores a part of the kinetic energy as strain energy. Some other kinetic energy propagates into the body as shear, compression or surface Rayleigh waves. The object rebounds during the restitution phase by recovering elastic strain energy into kinetic energy. An important parameter describing the collision is

the coefficient of elastic restitution, defined as the ratio of the velocity just after the collision to the velocity just before this collision.

There is much less work done on the influence of a surrounding fluid on solid-solid collisions compared to the dry solid-solid collisions.

The strain energy idea was extended to include the variation of the density and viscosity of the fluid layer with pressure (Barnocky & Davis, 1989). They observed that an increase in density of the fluid during compression could enhance the rebound of a impacting particle, even when the particle was completely rigid. The increase in viscosity with pressure results in the fluid behaving like an elastic solid, significantly affecting the deformation of an elastic particle and enhancing the rebound of the particle from a surface.

For the fluid structure interaction problems, especially in elastohydrodynamic approaches

Stokes number is more significant than the Reynolds number. Stokes number $St = \frac{2}{9} \rho_s \frac{UR}{\mu}$

$= \frac{1}{9} \frac{\rho_s}{\rho_f}$, which compares particle inertia to the viscous force (Barnocky & Davis, 1989).

For low Stokes number flows the particle does not show any rebound as all the elastic strain energy stored in the solid is dissipated in the fluid. For higher Stokes number the particle shows a rebound and the collision approaches to an elastic collision as the Stokes number increases.

The collision of ice with the structure is a more complex subject, due to its viscoelastic nature, which is not covered in this thesis. Rather the focus is on the kinematics of submerged ice as it collides with the hull .

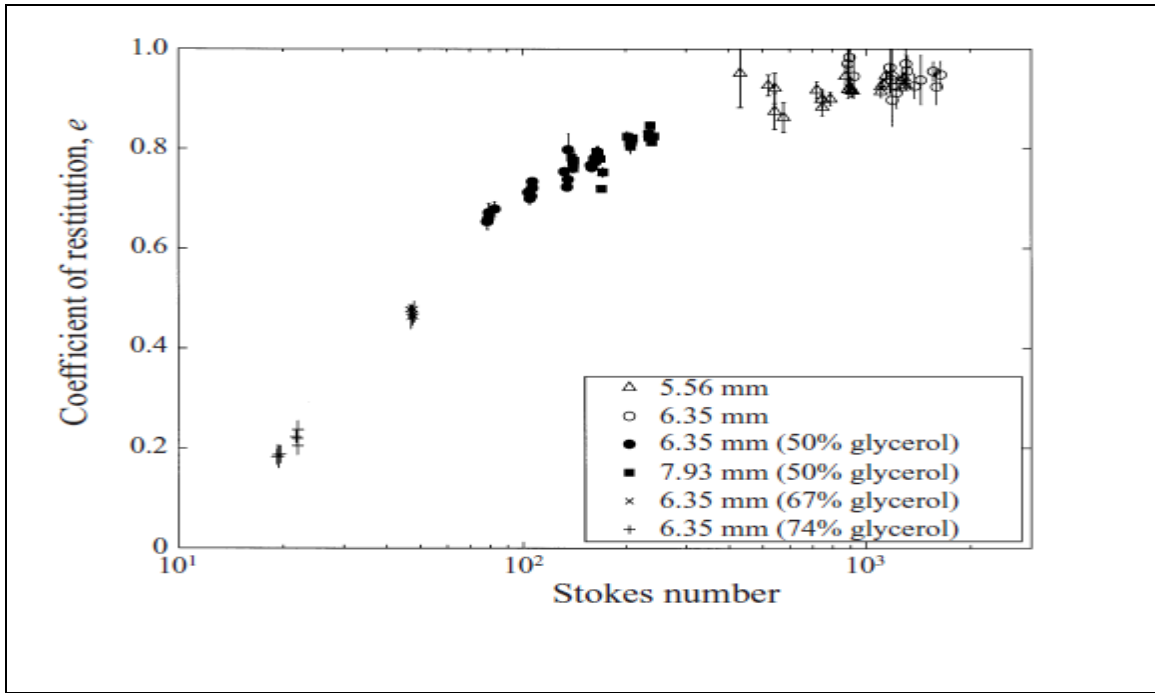


Fig 1.6 Effective coefficient of restitution as a function of particle Stokes number for immersed particle collision in water and glycerol-water mixtures.(G.G. Joesph, R.Zenit, M.L.Hunt and A.M. Rosenwinkel, 2001).

The study of effective coefficient of restitution as a function of particle stokes number for immersed particle collision in water and glycerol-water mixtures was studied by G.G. Joesph, R.Zenit, M.L.Hunt and A.M. Rosenwinkel. It was shown that the effective coefficient of restitution increases with the increase in Stokes number and approaches to and the collision approaches to elastic collision at high Stokes number.

1.9 Literature Summary and Problem Statement.

Although there has been a significant amount of work on ice structure interaction, not much emphasis is given on the study of submerged ice interactions. Even the full scale data for submerged ice collisions is limited. Hydrodynamics plays an important role in such type of interactions.

There have been experimental and theoretical studies to determine the hydrodynamic forces and coefficients of spherical particle approaching a rigid boundary. This study is extended to determine the hydrodynamic forces during submerged ice collision.

Numerical study using potential flow theory for a spherical particle moving towards a rigid boundary, gives an idea about the nature of added mass of spherical particle as it approaches the rigid boundary.

The coefficient of restitution is an important parameter which defines the energy transfer during impact. Due to the presence of fluid boundary between the rigid wall and sphere the values of coefficient of restitution are modified.

In the present work an experimental setup is designed to study the hydrodynamics of submerged ice collisions. These experiments are used to study the kinematics of such collisions, there is no actual indentation or crushing of the ice, the idea is to study the kinematics of collision rather than actual crushing.

The objective of the present work is to study the nature of submerged ice structure interactions and propose a first model to determine the hydrodynamics of such collisions.

CHAPTER 2 – EXPERIMENTAL MODEL

This chapter discusses the details of experimental design developed for the hydrodynamic tests. A detailed design of ship model was prepared using Rhino™. Structural strength was determined to make sure the rigidity of the model. The model was attached with a dynamic load cell to record the ice loads. Modal analysis was used to design the aluminium plate for impact with ice model.

2.1 SHIP MODEL

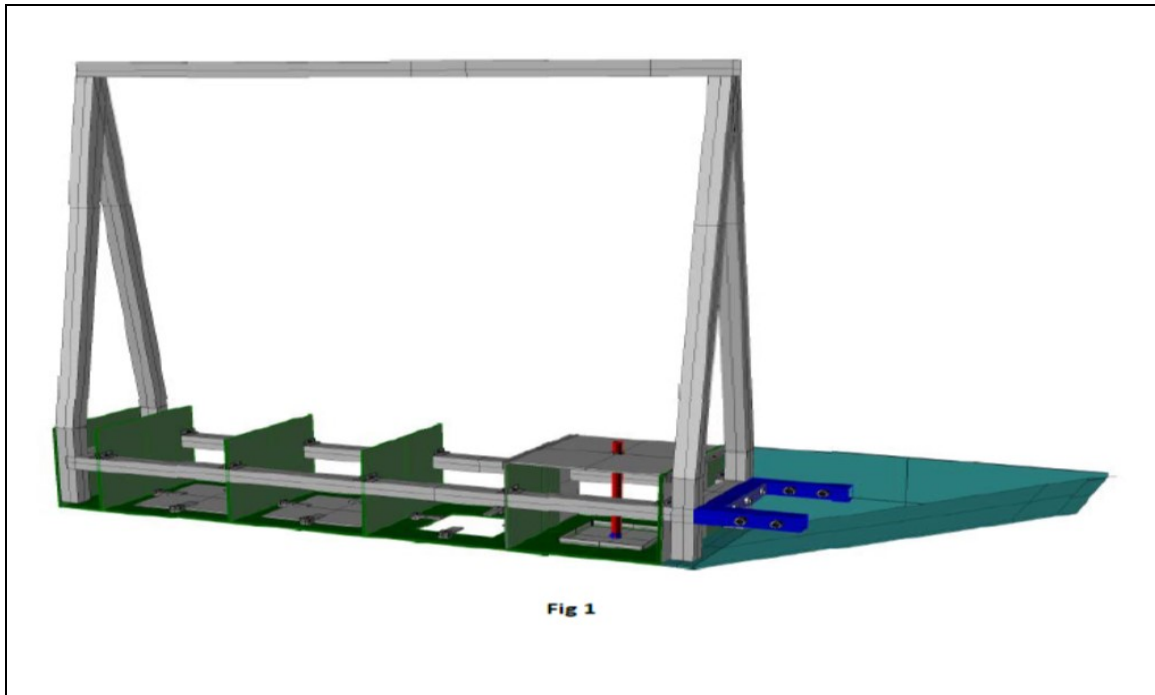


Fig 2.1 Lexan ship model with aluminium frame (side panels are not shown in image for inside view of the model.)

A lexan ship model 1.82m x 0.30m x 0.25m was designed with the support of Technical Services at Memorial University. The model was fabricated around an aluminium frame as shown in fig (3.1) to provide the structural rigidity. It was subdivided into four compartments to restrict the flooding during the experiments. Each compartment bottom was given a cut out 15.2cm x15.2cm to provide an opening for the load cell unit. These openings provided the different positions to install the load cell unit while conducting experiments. The unused openings were closed by a hatch which can be easily removed when a particular opening is being used.

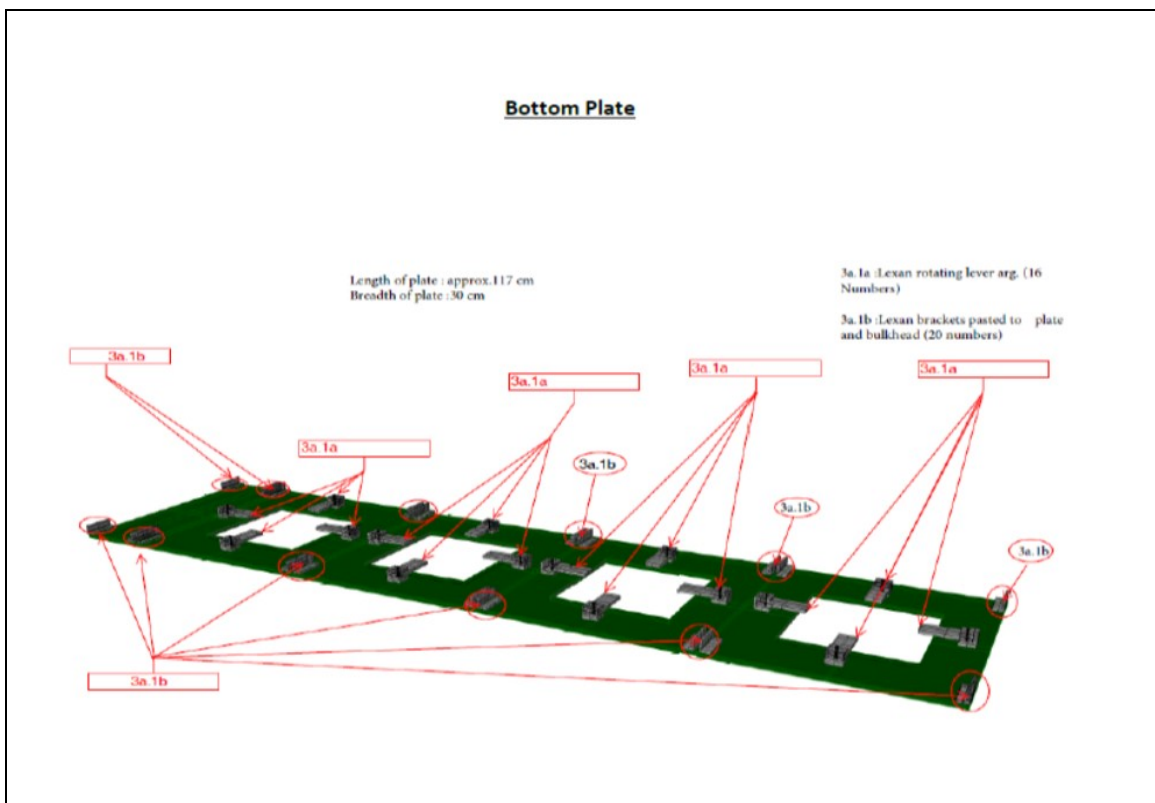


Fig 2.2 Hatch arrangement for bottom plate.

The bottom plate was designed with a closing arrangement, which can easily rotate so that the hatch cover can be lifted out to install the load cell unit. Water proof tape was used to further secure the leakage through the openings.

2.2 DYNAMIC LOAD CELL

In order to measure the forces during the collision, a dynamic load cell was used since the collision forces were impulsive in nature. Omega DLC101-50, dynamic load cell with tension and compression range of 0-50 lb was used during experiments to measure the impact loads. It has a frequency range of 25kHz. This load cell contains a thin piezoelectric crystal which generates an analog voltage signal in response to applied dynamic force.



Fig 2.3 Dynamic Load cell DLC101.

2.3 LOAD CELL UNIT

DLC101 load cell was attached to the centre of the aluminium plate of 15cm x 15cm using a screw. A lexan plate was used to make an enclosed watertight compartment (height 20cm) to avoid any damage due to flooding. PVC glue was used on the connecting edges to make it watertight.

A cylindrical steel rod 27cm in length and 1.9cm in diameter was attached to the load cell, which could be detached easily from the load cell compartment. The rod was attached to a circular flange through screws, and the flange was screwed to a rigid steel plate 0.5cm thick. The plate sits on the bulkheads of the compartment and can be screwed to it, making a rigid arrangement in order to avoid any unwanted loss of energy due to vibrations in the structure during collision.

It was made sure that the load cell unit sits inside the hatch opening without touching the edges of the bottom hull, so as to avoid any force transfer to the model. The idea was to have a collision with the aluminum plate attached to load cell without having any losses in order to record accurate ice loads.



Fig 2.4 Load cell unit.

2.4 ALUMINUM PLATE FREQUENCY RESPONSE

The underwater ice collision with the aluminum plate is dynamic in nature so we need to determine the plate vibration characteristics and its response to dynamic loading. A natural frequency study of aluminum plates of different dimensions was done to determine the plate best suited for the tests, some preliminary tests done using the ice model showed that the frequency of collision is around 1650Hz.

This frequency of collision of ice loads was used as a limiting value for determining the frequency response and optimal dimensions of the plate.

The natural frequency of the plate is used to determine accurate load transfer to the load cell without any vibration losses in the plate during the collision. This information is used

to determine the time step, frequency of data acquisition in order to capture the output voltage signal accurately.

Modal analysis of a plate comprises calculating the Natural frequencies and Modes of vibrations.

Below is a solution to the equation of motion with suitable boundary conditions and Initial conditions.

General Equation of Motion:

$$[M] \{ \ddot{u} \} + [C] \{ \dot{u} \} + [K] \{ u \} = \{ F(t) \} \quad (2.1)$$

$[M]$ = Mass matrix.

$[C]$ = Viscous damping matrix.

$[K]$ = Stiffness matrix.

$\{ \ddot{u} \}$ = Time history of acceleration.

$\{ \dot{u} \}$ = Time history of velocity.

$\{ u \}$ = Time history of displacement.

$\{ F(t) \}$ = Time history of force excitation.

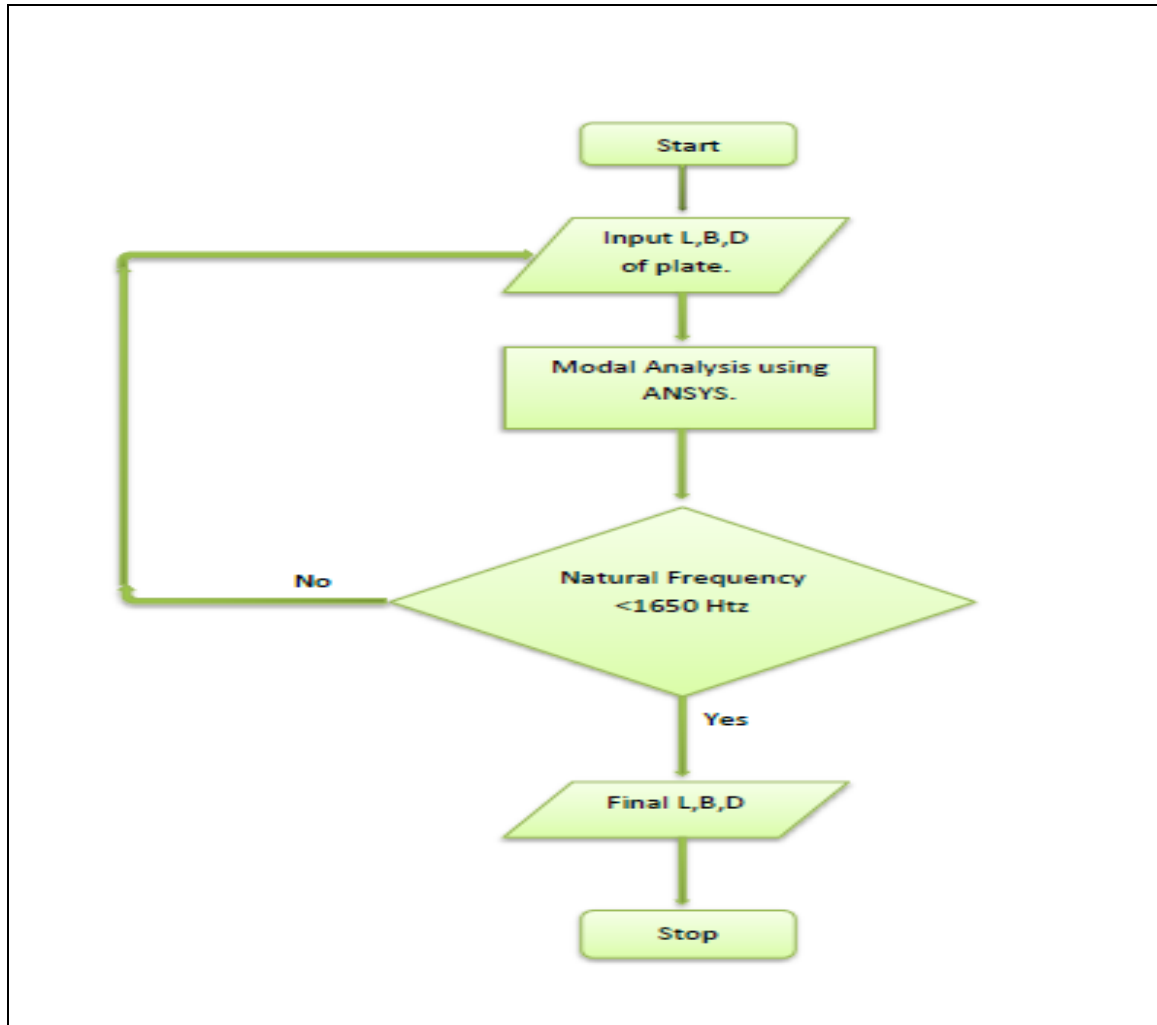


Fig 2.5 Flowchart to determine the dimensions of the aluminum plate used for ice collision.

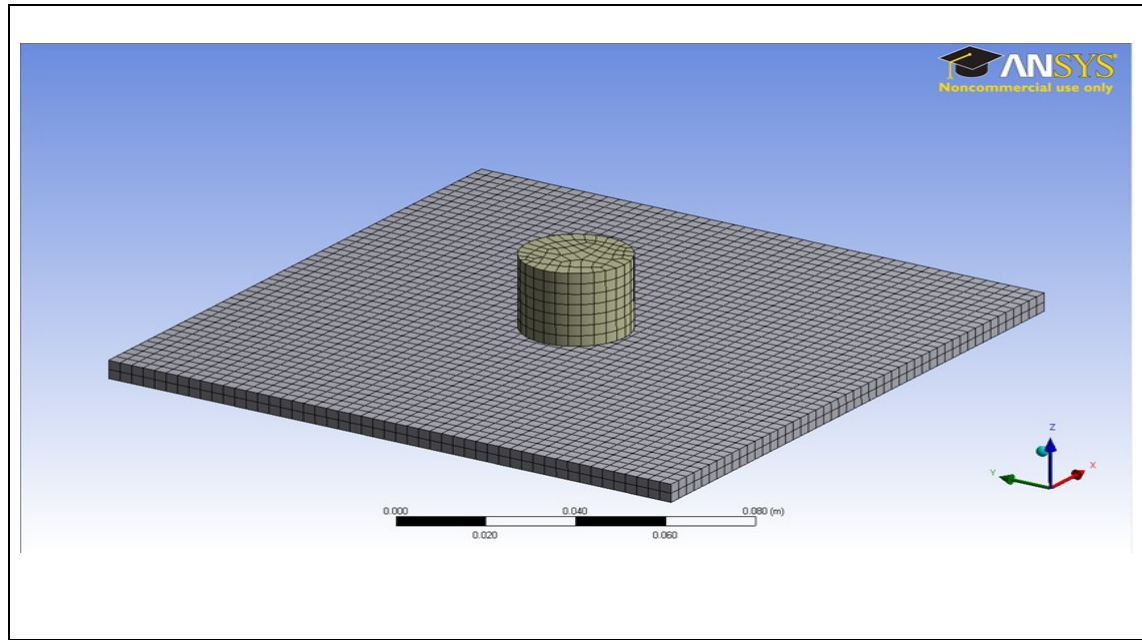


Fig 2.6 Aluminium plate mesh with a load cell at the centre for Modal Analysis.

Modal analysis of an Aluminum plate 15cm x15cm was performed in ANSYSTTM for varying mesh sizes: 2.5mm, 5mm, 10mm, 15mm to study the effect of mesh size on the solution and to choose the optimum mesh size.

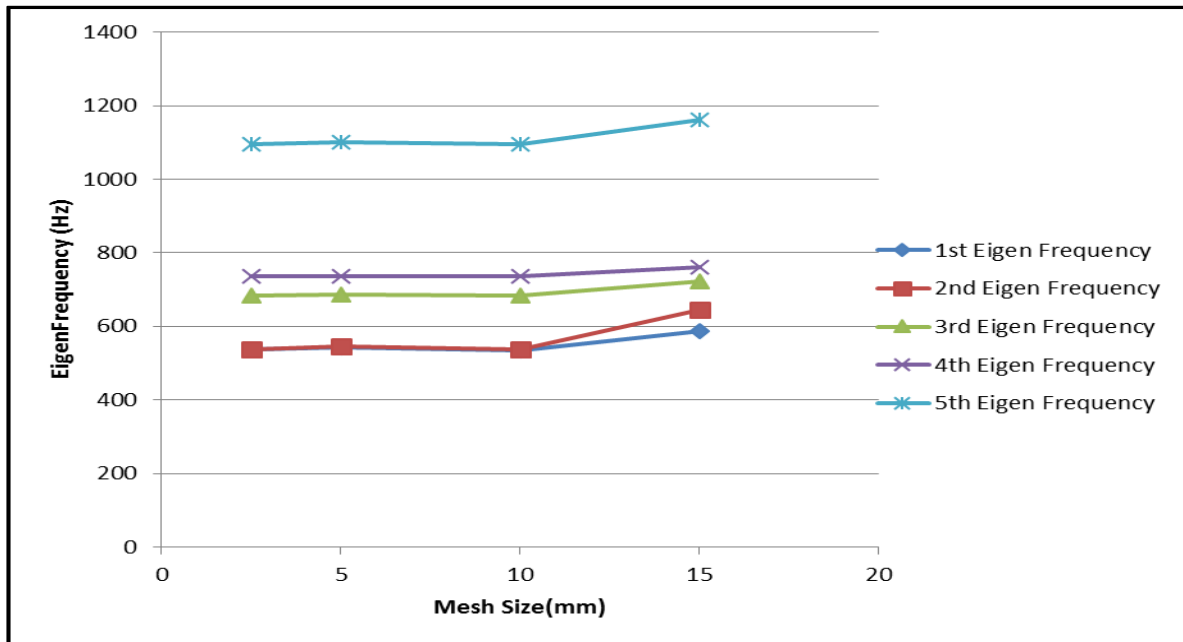


Fig 2.7 Eigen frequencies of Aluminium plate with different mesh density

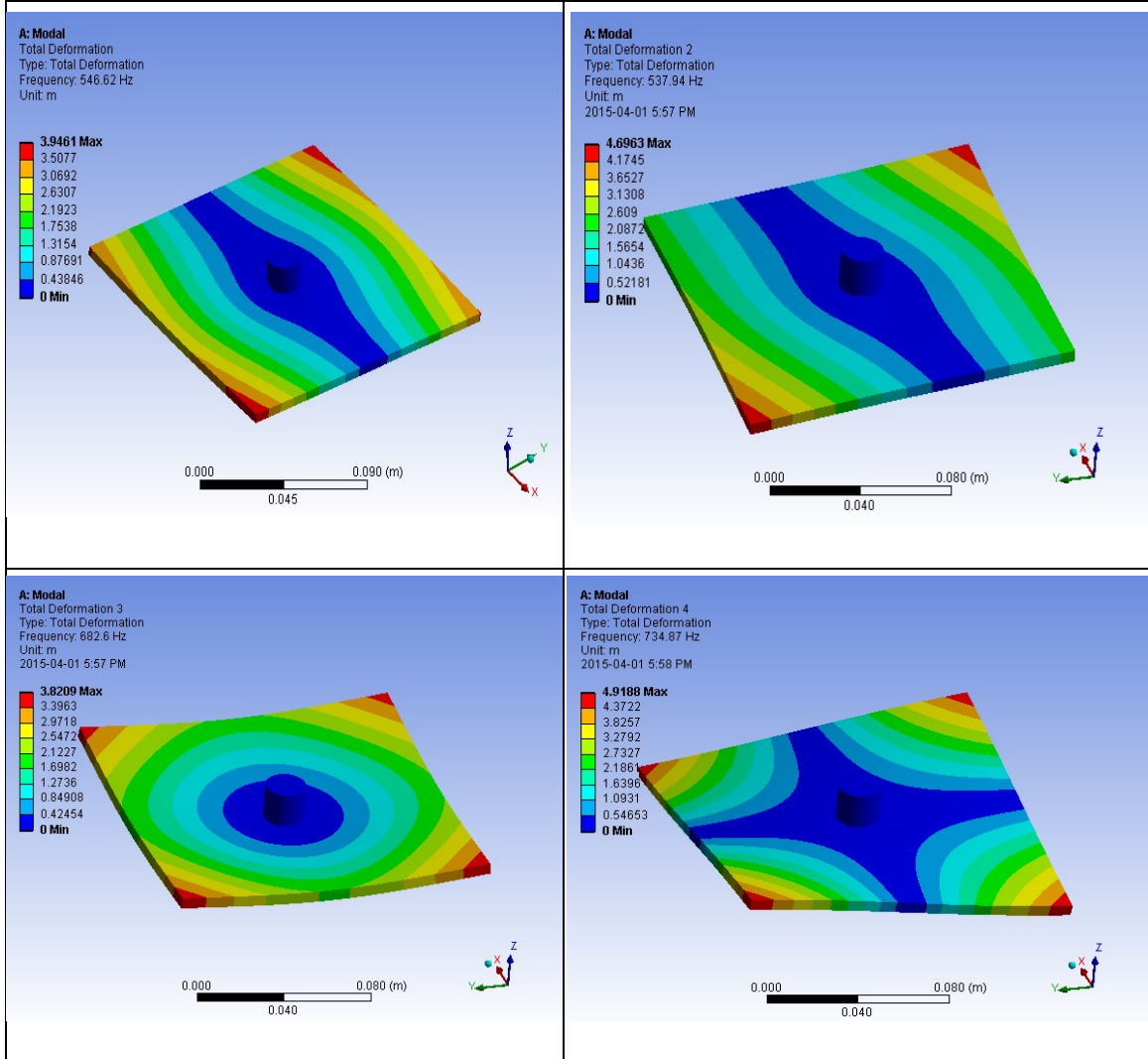
For mesh 2.5mm first five eigen frequencies are: 536.87Hz, 537.56Hz, 682.44 Hz, 734.81 Hz, 1065.9Hz.

For mesh 5mm first five eigen frequencies are: 545.56Hz, 546.62Hz, 682.6Hz, 734.87Hz, 1096.1Hz.

For mesh size 10mm first five eigen frequencies are: 534.36Hz, 536.98Hz, 683.53Hz, 735.16Hz, 1094.8Hz.

For mesh size 15mm first five eigen frequencies are: 586.48Hz, 644.99Hz, 723.86Hz , 760.86Hz, 1161.3Hz.

The results indicate that the mesh size does not influence the solution significantly, so the results of 5mm mesh were used in the analysis.



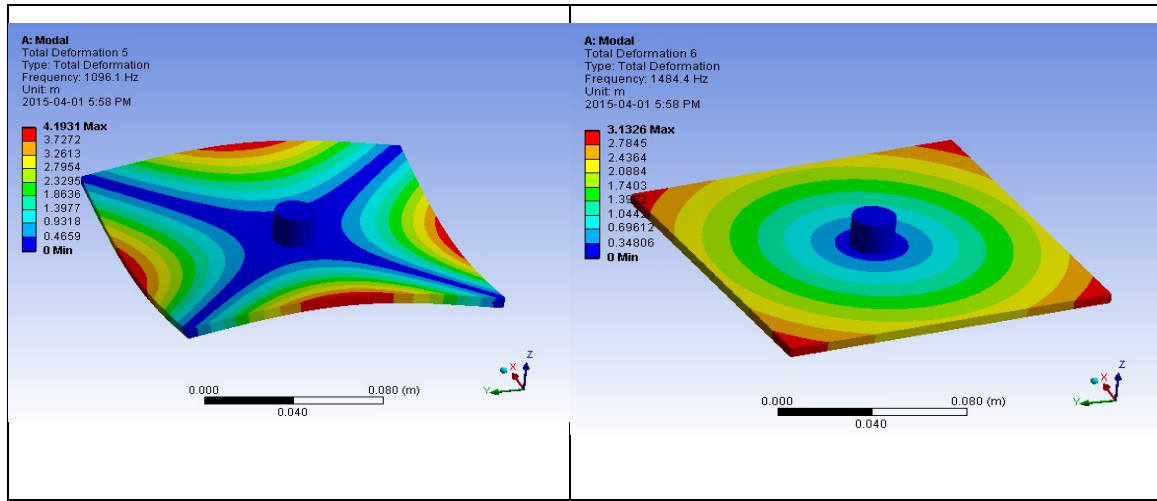


Fig 2.8 Eigen frequencies of Aluminum Plate

2.5 ICE MODEL

Since the use of real ice required maintaining low temperatures during the tests, a polypropylene material was used to simulate the ice, as the density of polypropylene is very close to that of ice.

Rather than looking into the actual crushing of ice we are looking into the hydrodynamics of collision, so using a polypropylene model to emulate the real ice hydrodynamics under normal laboratory conditions suits the purpose of these experiments.



Fig 2.9 Ice Model (Diameter = 10cm)

2.6 RELEASE MECHANISM

In order to position the ice model inside the tank, an L shaped stainless steel bar with two adjustable hooks at each end was fabricated. A fishing line passing through these hooks was used to position the ice model at different heights (Figure 2.10).

After adjusting the position of the model, the opposite end of the fishing line was held until the water was calm. It was then released so that the ice model moves up freely, driven by buoyancy, to collide with the aluminium plate.

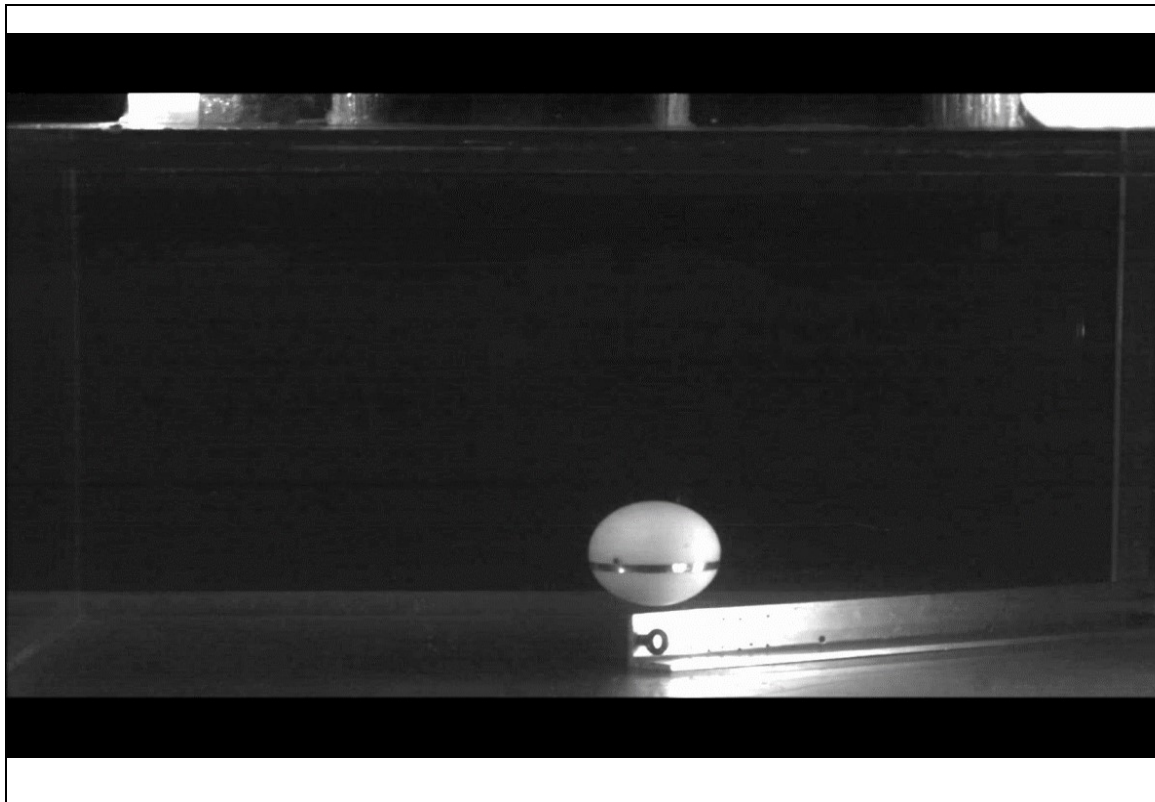


Fig 2.10 Ice model release mechanicsm.

2.7 LAB VIEW

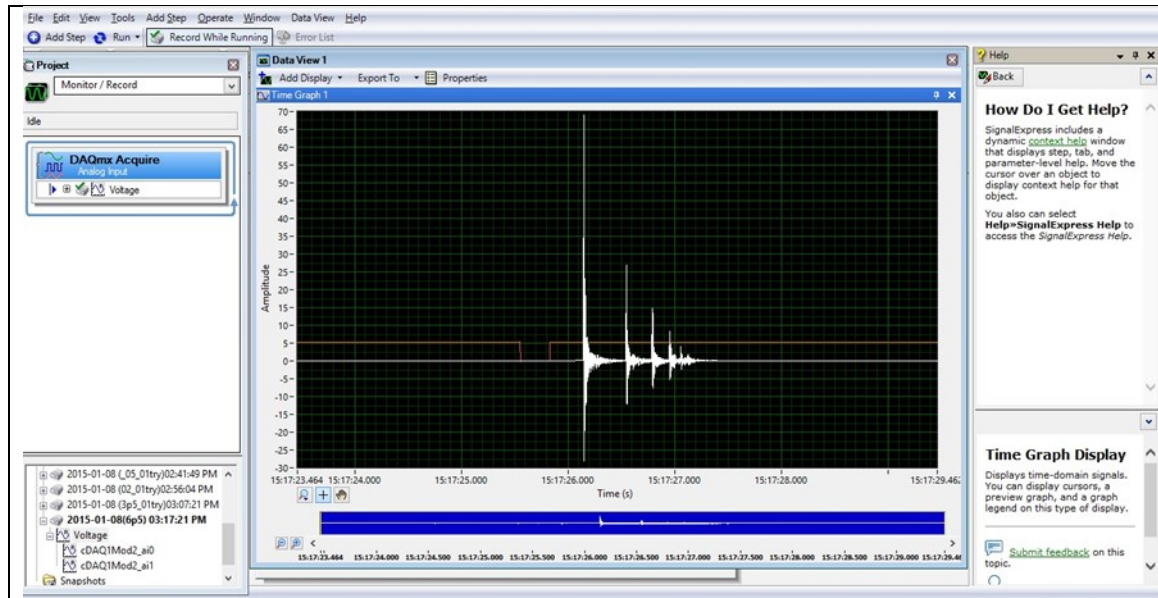


Fig 2.11 LabView.

The load cell was connected to the first channel of data aquistion system NI9239 through an amplifier while the camera trigger was connected to the second channel on DAQ. NI compact DAQ was connected to the LabViewTM, for each run camera trigger marks the point of the release of ice model, in order to synchronize the displacement data from high speed video with the load cell data. The data was recorded at the smapling rate of 25 Khz. The LabViewTM project for the load cell was calibrated dynamically using a load hammer and weights to get a conversion equation from voltage to lbf (4.448 N).

CHAPTER 3 IMAGE ANALYSIS

3.1 HIGH SPEED VIDEO

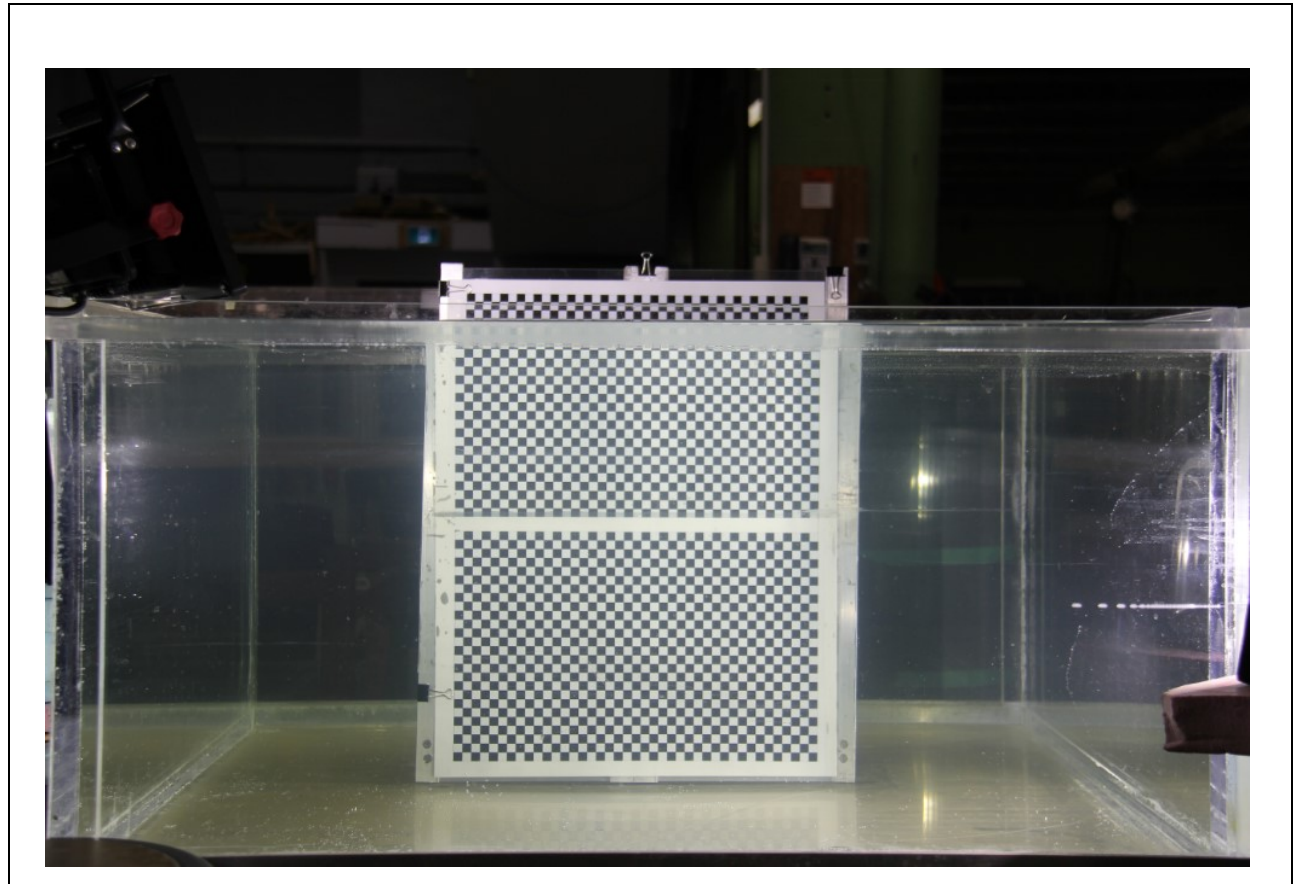


Fig 3.1 Calibration for the high speed video recording.

A high speed camera was used to record the experiments. The video was used to analyse the ice model position & velocity at each time steps. From the preliminary tests using the dynamic load cell, it was determined that the duration of first impact was about 500

microseconds (5×10^{-4} sec). Since the collision takes place at such a short time interval, in order to accurately capture the images during collision, high speed camera at 30,000 frames per second was used. It was made sure that the camera was parallel to the ground and perpendicular to the tank surface to avoid any error arising due to the camera position. A chequered frame was used to calibrate the camera pixels to the measurements units (meters). The frame was positioned approximately parallel and near the position of the release of ice model. Each square in chequered frame is 1cm x 1cm. The recorded video was converted to images at 30,000fps using video to image converting software. The algorithm was developed in MatlabTM to read and convert images into binary format by tuning the grayscale. Gray conversion was done mainly to convert a RGB image (three dimensional matrix) to gray scale (two dimensional matrix) having pixel values ranging from 0 to 255. Various types of unwanted noise get added to the video during recording. Contrasts and filters were used to reduce the noise in the images. The filtered greyscale image was converted to binary image which is a two-dimensional image with pixel values either 0 (black) or 1 (white).

Edge detection technique ‘Sobel’ is used to mark the objects boundary. This can be done only when the gray scale image is converted to binary. This is done by applying ‘graythresh’ function on gray image and then ‘im2bw’ and ‘bwareaopen’ functions on the previous output consecutively. (MatlabTM Help).

‘Grain’ command was used to detect the objects boundaries in image and select the ice model boundary, once the boundary was selected. The ‘bounding box’ command was used to track the position of the ice model, it gave the output in terms of centroids and location

of the edges of bounding box. ‘Bounding box’ command determines the time evolution of trajectory during the experiment.

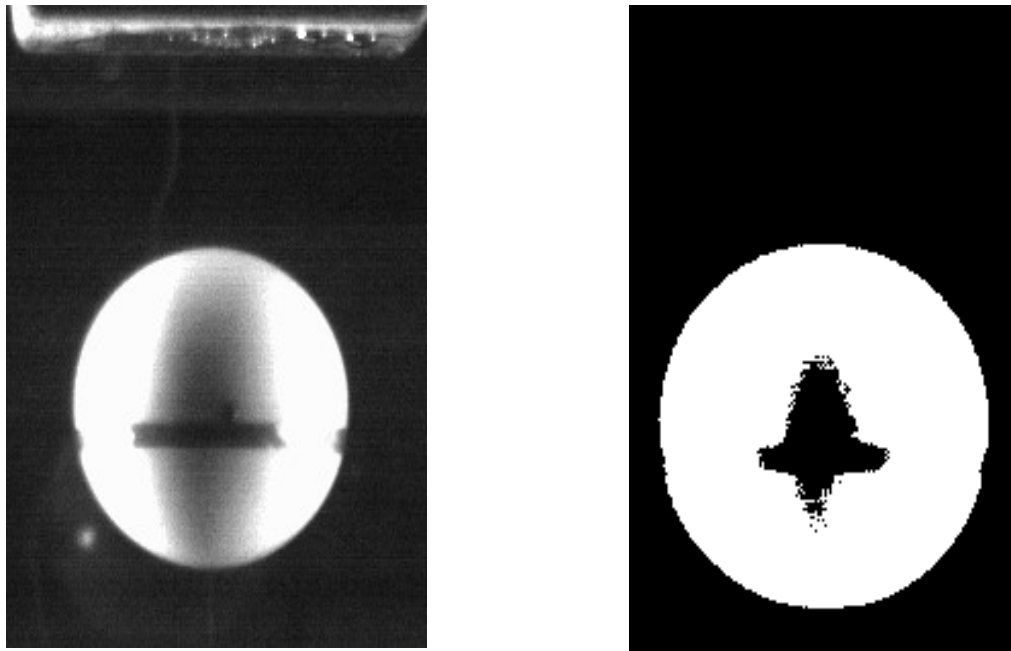


Fig.3.2 Conversion to Binary Image in MatlabTM

A typical displacement output from Matlab is shown below:

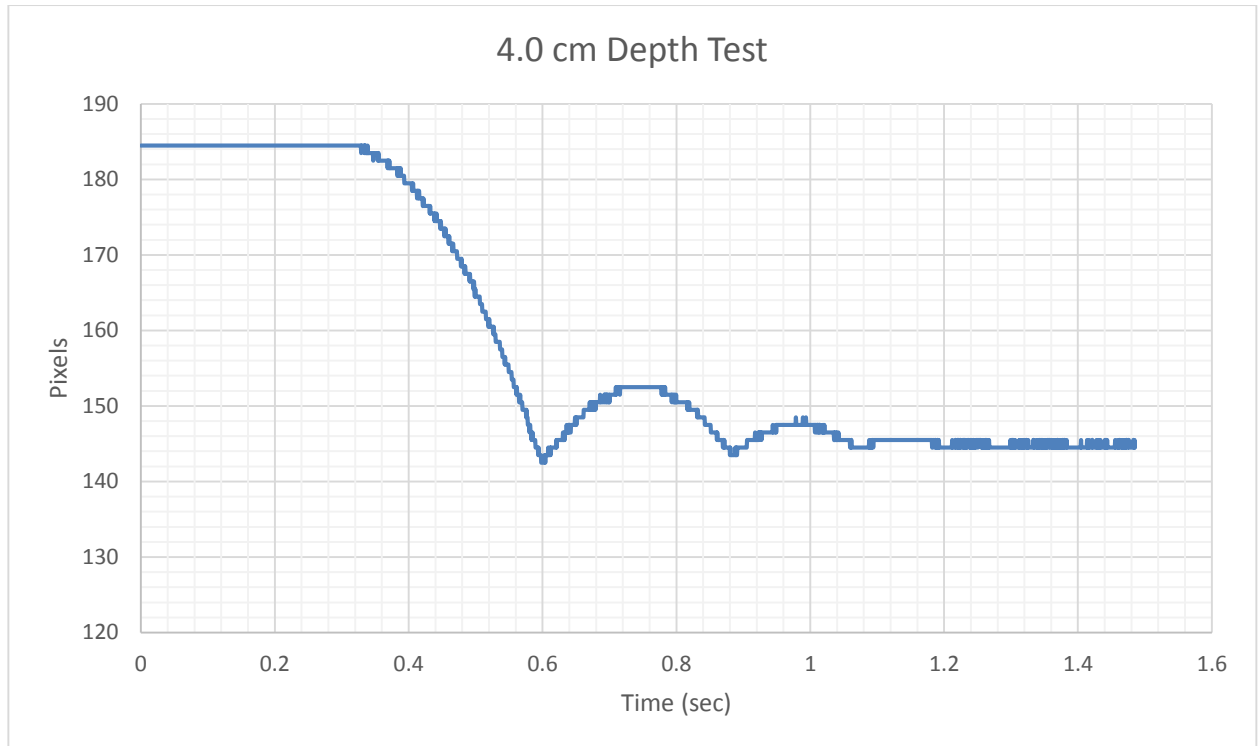


Fig 3.3 Displacement (pixels) v/s time (sec) for ice model released from 4cm depth.

The Matlab™ for tracking the position of the ice model at each time interval gives the output in pixels, which is converted to metric units using the conversion factor. The conversion factor is determined using the checkered board placed parallel to the plane of ice model ,each square in checkered board is of size 1cm x 1cm. The image of checkered board was used to calculate the conversion factor from pixels to metric units (Fig 3.1). The plot shows a peak at each point of contact. Due to the high frequency of data being processed there was a noticeable noise in the output data.

3.2 Error estimation arising due to the intrinsic, extrinsic and lens distortion parameters of camera .

Error arising due to the camera parameters is determined using the chekerboard calibration pattern. The chekerboard images are captured using the camera. These images are read into matlab and the pattern is read and compared with the corosponding world point projected into the same image. This is also knows as reprojection error.

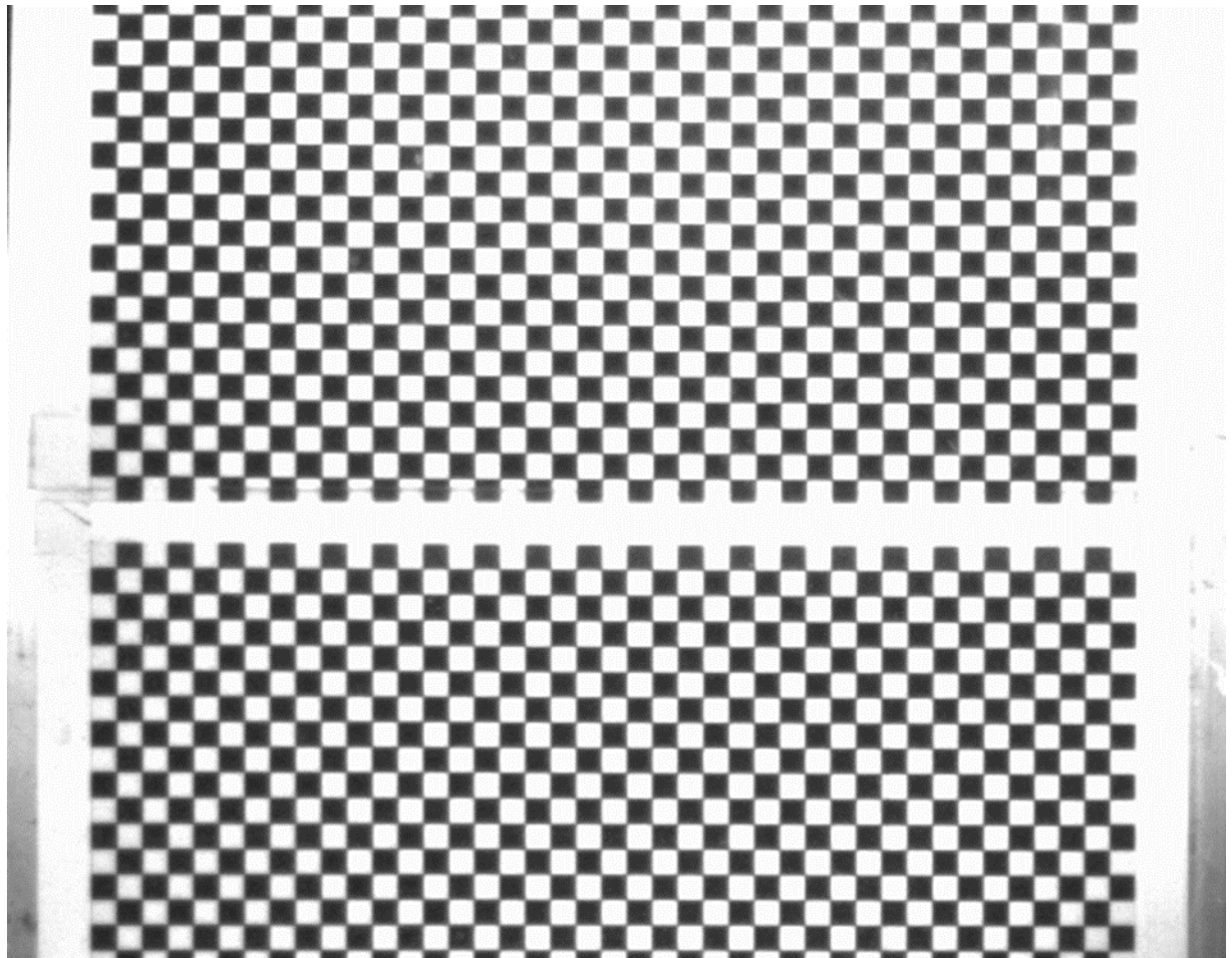


Fig.3.4 Checkerd pattern used for calibration of camera.

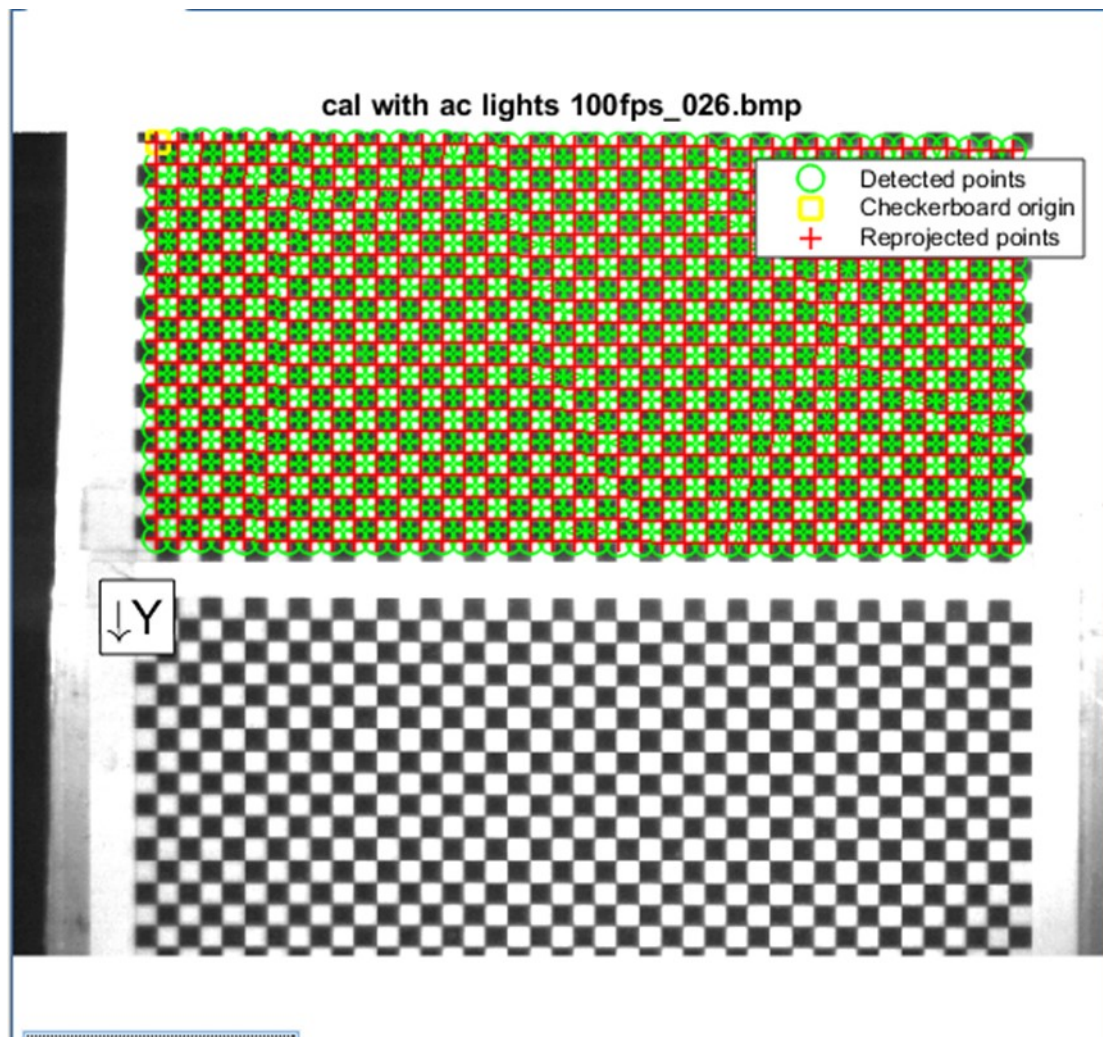


Fig.3.5 Matlab analysis of calibration images from camera.

Projection of the world point on the checkered plane to determine the distortion in image arising due to the camera.

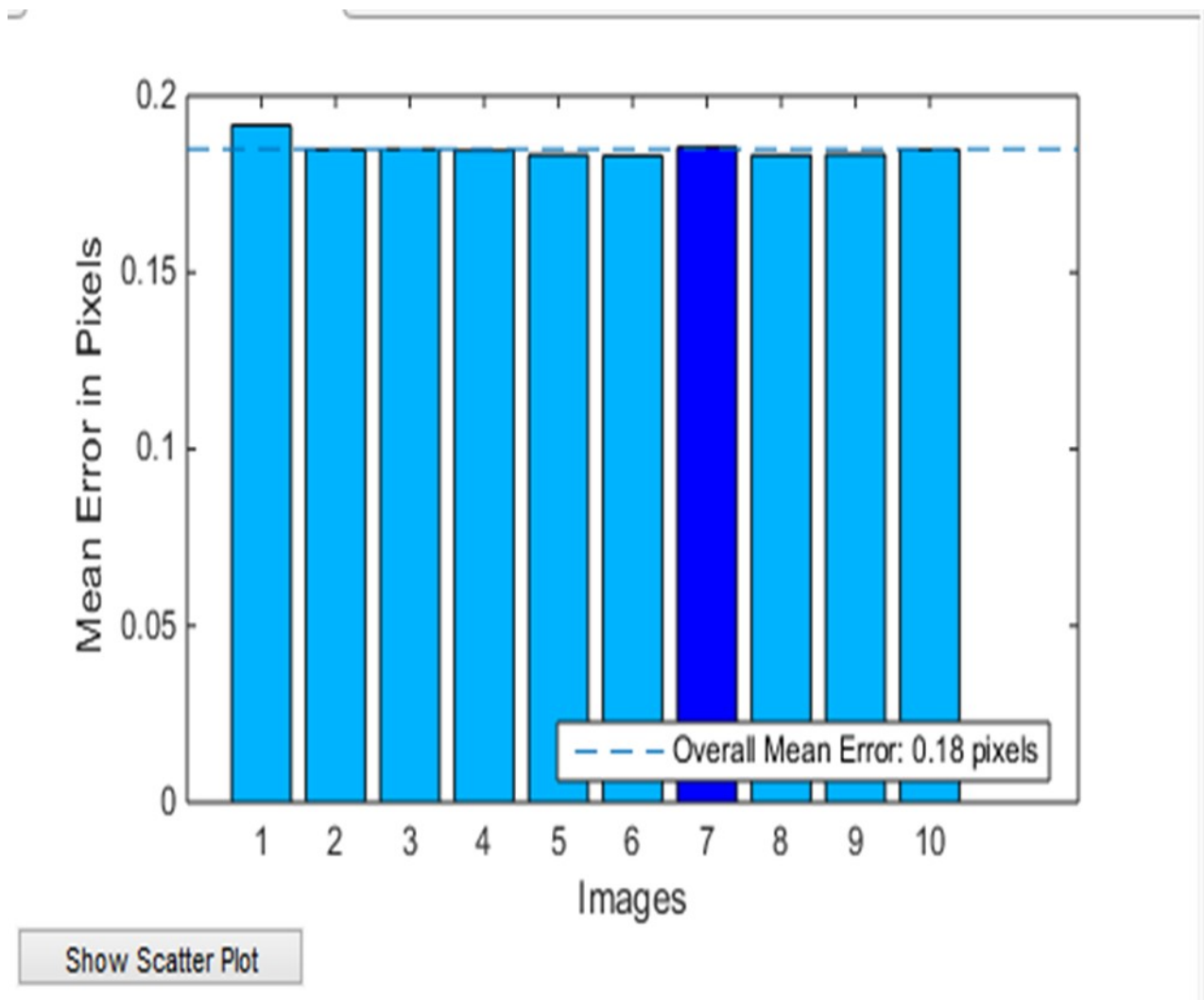


Fig.3.6 Mean error arising due to camera parameters in pixels

Mean overall error calculated using 10 images of checkered board for camera calibration was found to be around 0.18 pixels

CHAPTER 4 RESULTS

4.1 Displacement and velocity of Ice model from Matlab data.

Focusing on the first impact of ice model with the load cell plate. Considering $t=0$ as the time of contact, the displacement data can be divided into three groups: position before impact, position during impact and position after impact. Tests were conducted for six depths of release 2cm, 3.5cm, 5cm, 6.5cm, 8cm and 10cm respectively. Due to the limited availability of high speed camera only 2cm and 5cm depth tests were repeated twice.

a) Depth 2cm release test:

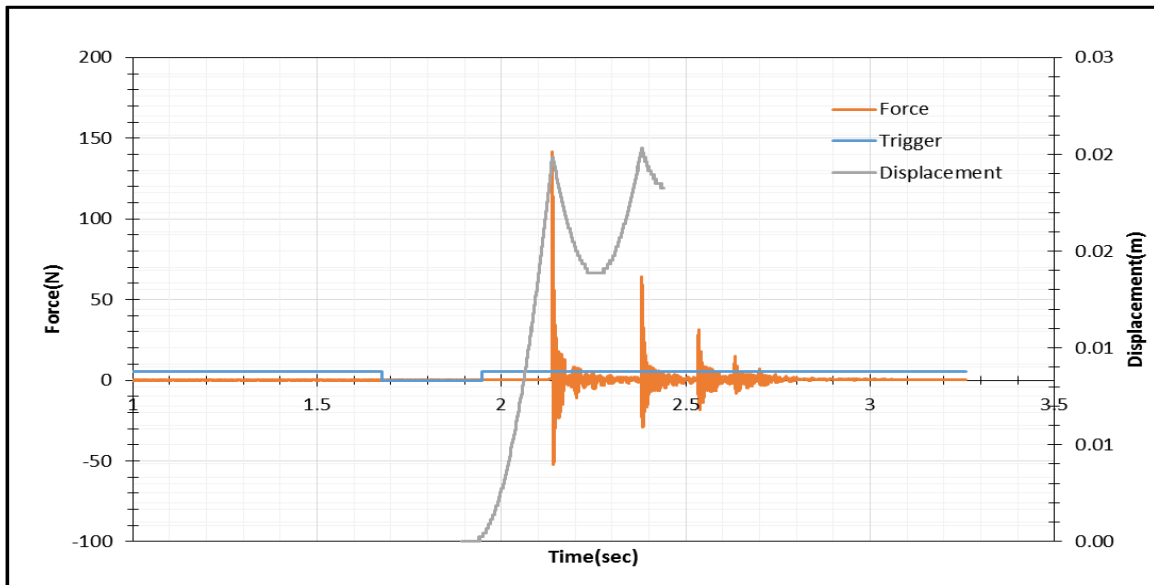


Fig 4.1 Force, displacement experimental data 2cm depth.

Both high speed camera (30,000 FPS) and data aquisition system(25Khz) were connected with a trigger in order to achieve a syncronised data for displacement and impact force respectively.

For each test it was made sure that the fluid was stationary, before the recording starts. For 2cm depth the maximum force at the first impact was 140N.

b) Depth 3.5 cm release test:

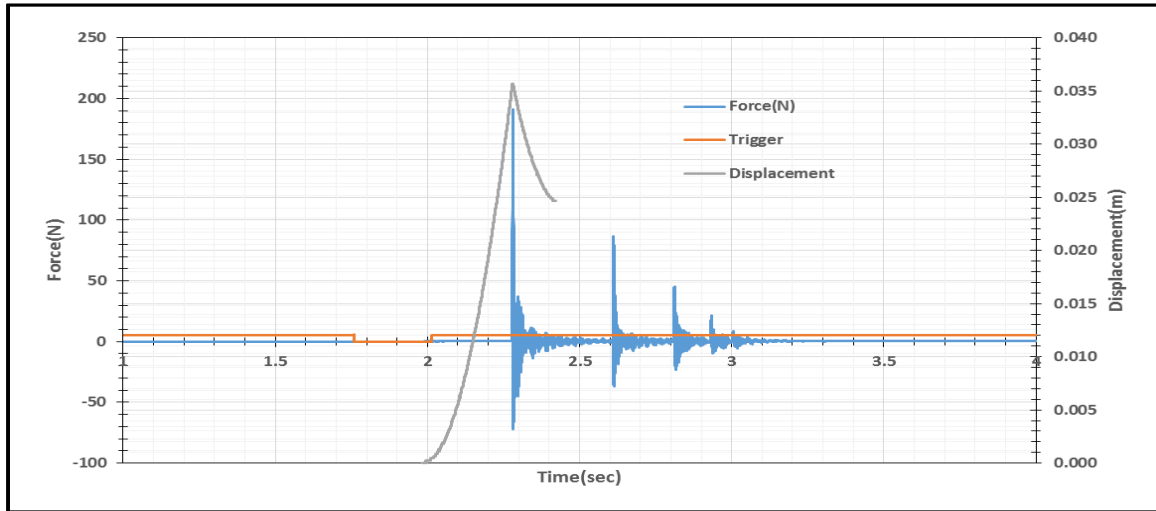


Fig 4.2 Force, displacement experimental data 3.5cm depth.

For 3.5cm depth test the maximum force at first impact was 210N.

c) Depth 5 cm release test:

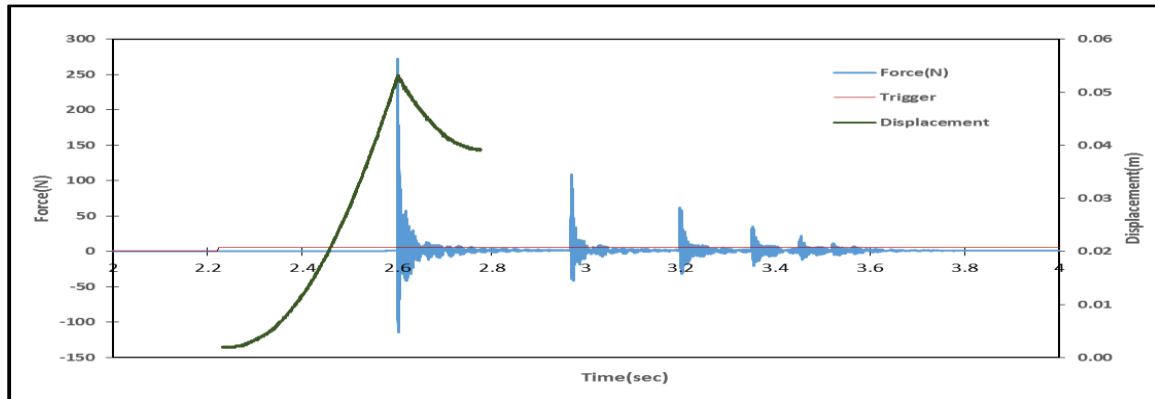


Fig 4.3 Force, displacement experimental data 5cm depth

For 5cm depth test the maximum force at first impact was 270N.

d) Depth 6.5 cm release test:

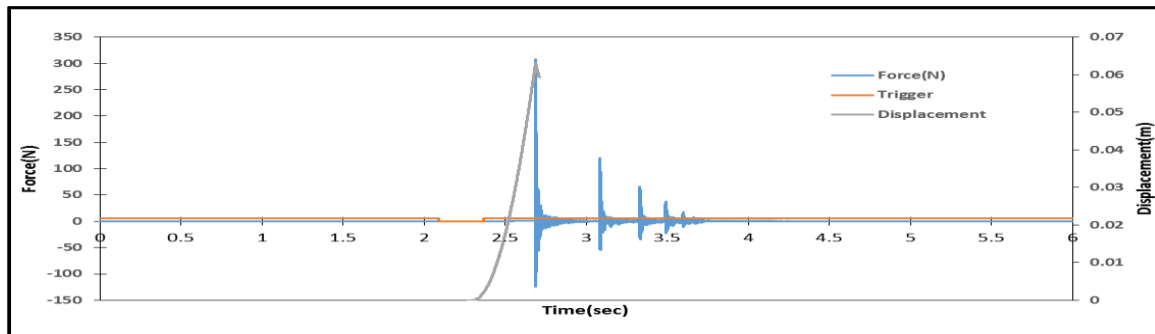


Fig 4.4 Force, displacement experimental data 6.5cm depth.

For 6.5cm depth test the maximum force at first impact was 310N.

e) Depth 8cm release test.

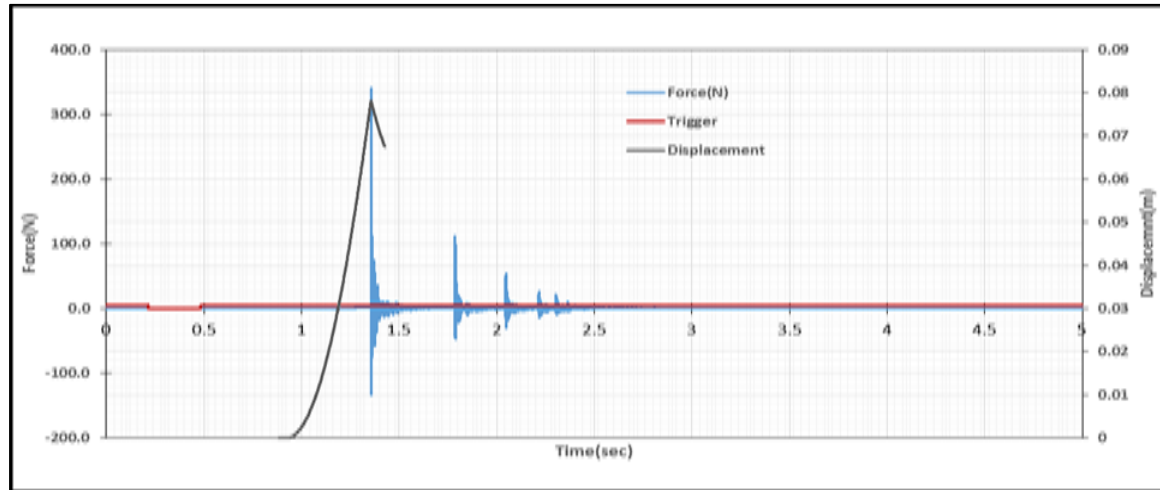


Fig 4.5 Force, displacement experimental data 8cm depth.

For 8cm depth test the maximum force at first impact was 337.9N.

f) Depth 10cm release test:

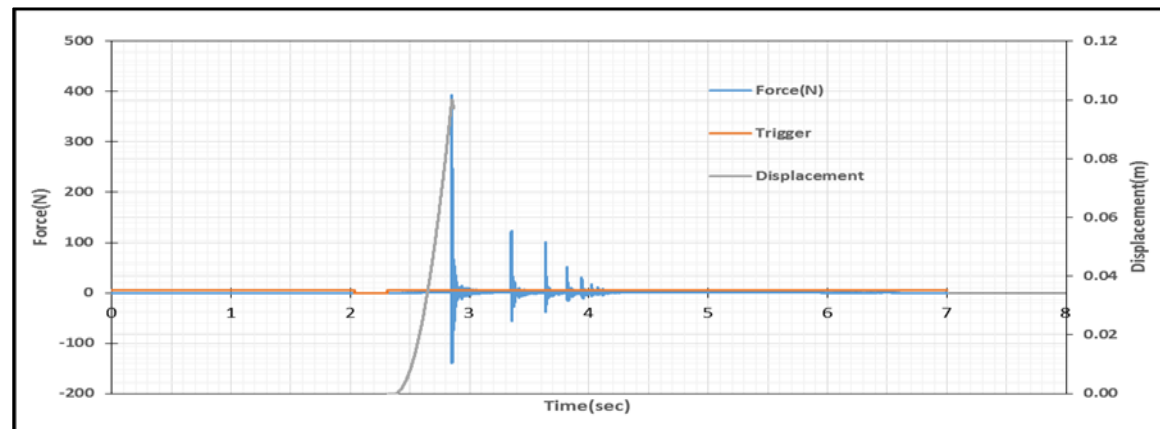


Fig 4.6 Force, displacement experimental data 10cm depth.

For 10cm depth test the maximum force at first impact was 393.5N

The results shows that the impact force increases gradually with the increase in depth. Since at higher depths the model is able to achieve higher impact velocity and hence the larger value of momentum being transferred to the structure during collision.

This data is used to further calculate the velocity and accelerations for each test, and determine the hydrodynamic forces.

4.2 Experimental Data Analysis.

Displacement data from image analysis was stepwise, the noise in the data was not easily detectable due to very small time step, but on differentiating the data the noise got amplified which was further intensified while calculating acceleration. Various filtering methods were tried to smooth the data without the loss of information. Moving trend line method was used to filter the data and find the velocity. It is used to smooth out short-term fluctuations and highlight longer-term trends or cycles. Moving trend line method can be viewed as an example of a low-pass filter used in signal processing.

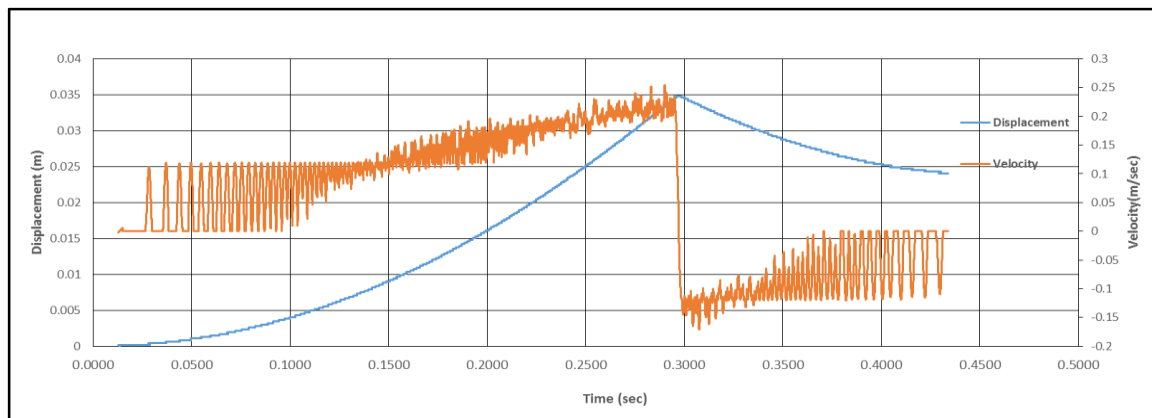


Fig 4.7 Data Filtering using moving average.

Each set of displacement data was fitted with a quadratic equation. For example selected first 0 to n data points were fitted with a quadratic curve to interpolate the value of displacement, velocity at the point $n/2$. Next the data set moves from 1 to $n+1$, to interpolate the value at $n/2+1$, these steps are repeated throughout the data points of each experiment. The quadratic equation at each time interval was differentiated to calculate the velocity.

Thus the velocity obtained by this method is weighted averaged over short time intervals.

Cubic and quadratic polynomials were used to get the best fitting curve to calculate accelerations from velocity.

Data for each experiment is grouped into data before collision and data during collision, in order to accurately determine the velocity and acceleration values during the collision since the duration of collision or the time for which the model stays in contact with the aluminium plate is as low as 1 milisecond.

4.2.1 Depth 2 cm Analysis.

Considering $t=0$ as the point of impact, data for 2cm depth is grouped as before collision and after collision.

4.2.1a Before Collision.

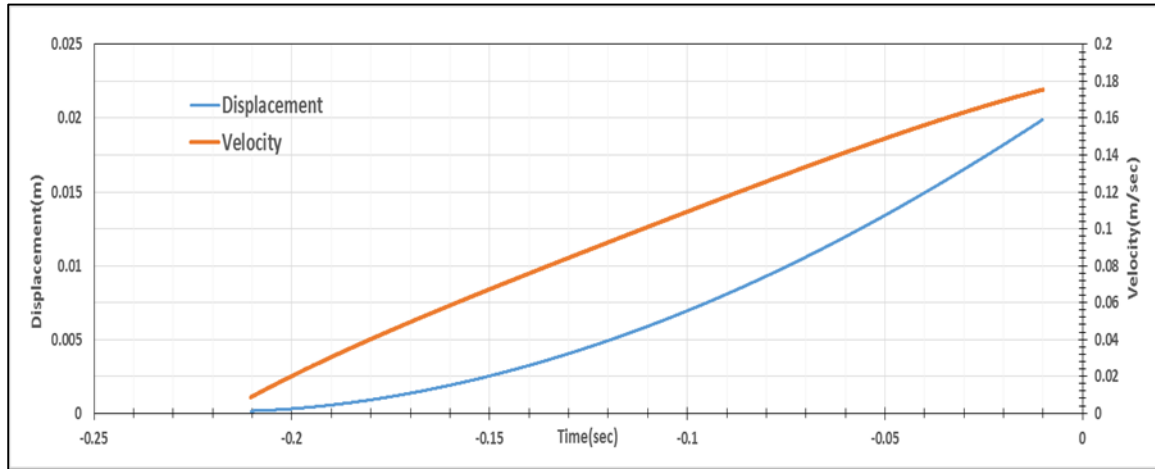


Fig 4.8 Displacement, Velocity before collision for 2cm depth.

The displacement data is used to determine velocity and acceleration and Eq. 1.9 is used to calculate the C_A values at each time step.

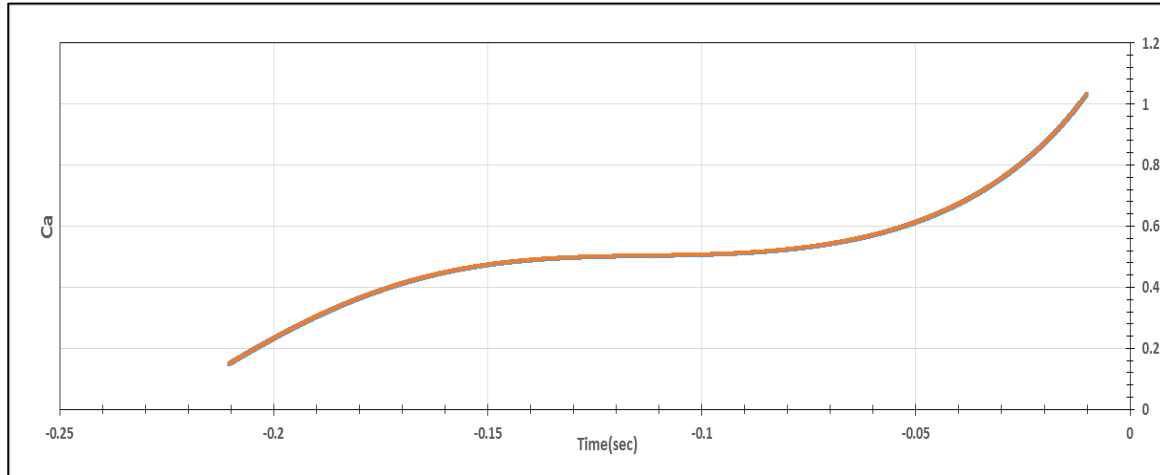


Fig 4.9 Ca added mass coefficient before collision for 2cm depth.

The added mass coefficient rises gradually as the ice model starts to move vertically towards the aluminum plate and attains a value close to 0.5. C_A starts to rise again as the ice model approaches close to the plate.

4.2.1b During Collision.

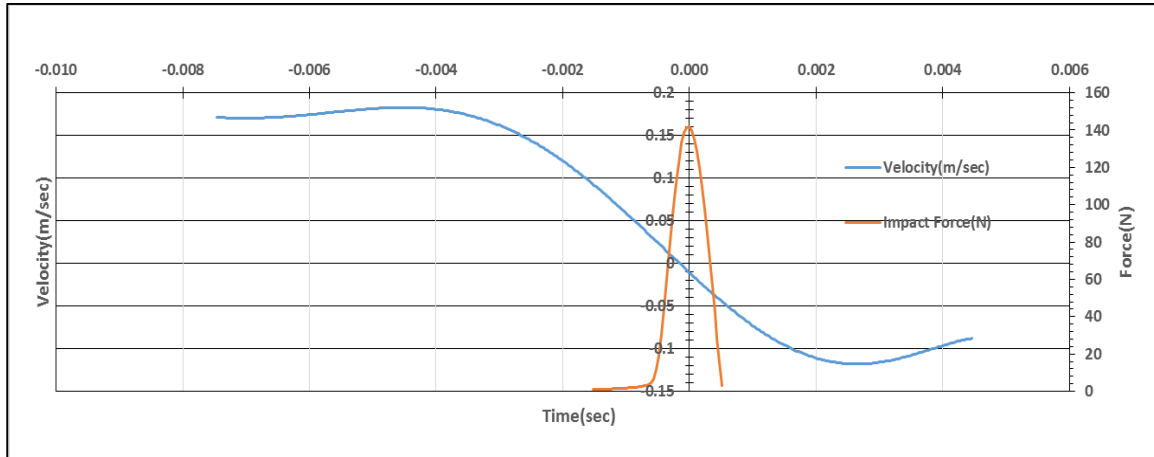


Fig 4.10 Impact force, Velocity during collision for 2cm depth.

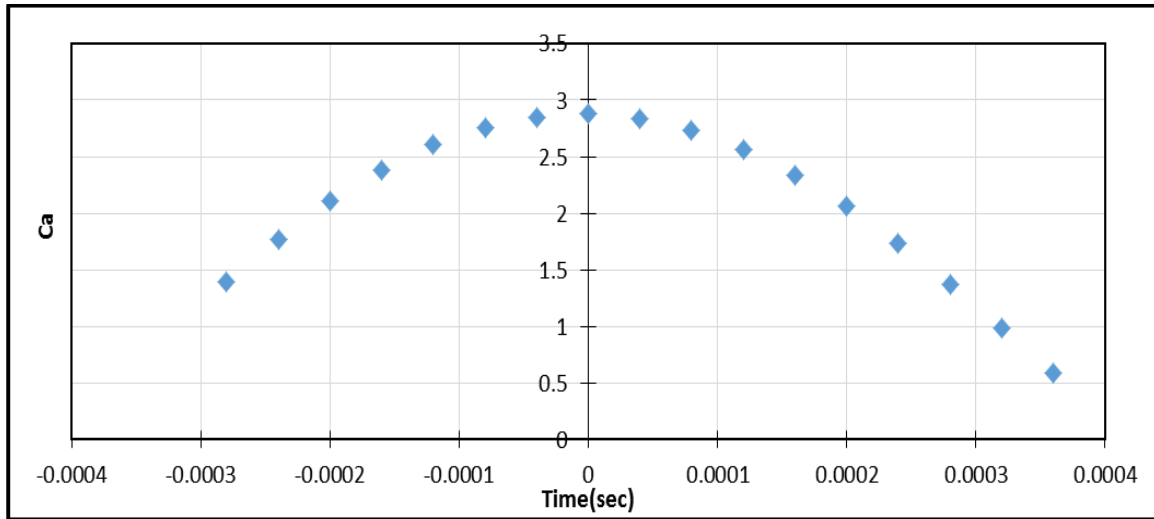


Fig 4.11 C_a added mass coefficient during collision for 2cm depth

Analysing the data for 2cm depth test during collision, the impact force reaches a maximum value of 140N in a short time interval of 0.001 sec. The moving trendline method is used

to determine the velocity and acceleration values at each time step, which are used in Eq (1.10) to calculate the added mass values during the collision.

The added mass coefficient values during collision rises rapidly and attains its maximum value around 2.9 at the point of impact and drops down gradually.

4.2.2 Depth 3.5 cm Analysis.

4.2.2a Before Collision

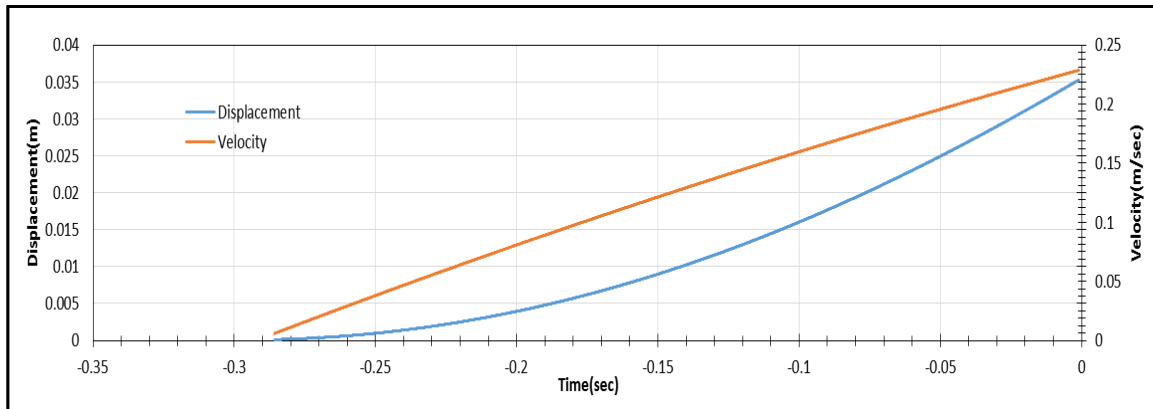


Fig 4.12 Displacement, Velocity before collision for 3.5cm depth.

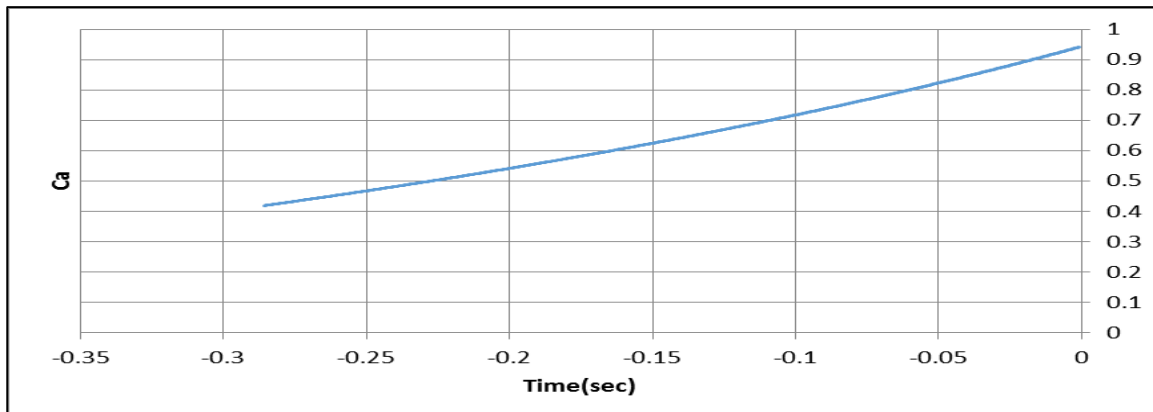


Fig 4.13 C_a added mass coefficient before collision for 3.5cm depth.

The Ca values before collision for 3.5cm were determined in a similar fashion as explained in case of before collision for 2cm.

Initial Ca values lies between 0.4-0.5 and rises rapidly as the ice model approches closer to the aluminum plate.

4.2.2b During Collision.

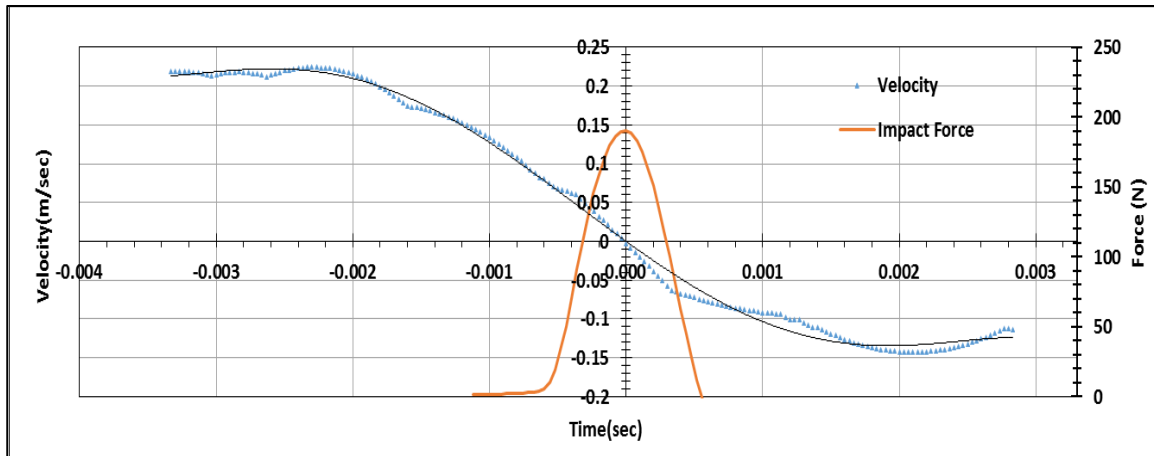


Fig 4.14 Impact force, Velocity during collision for 3.5cm depth.

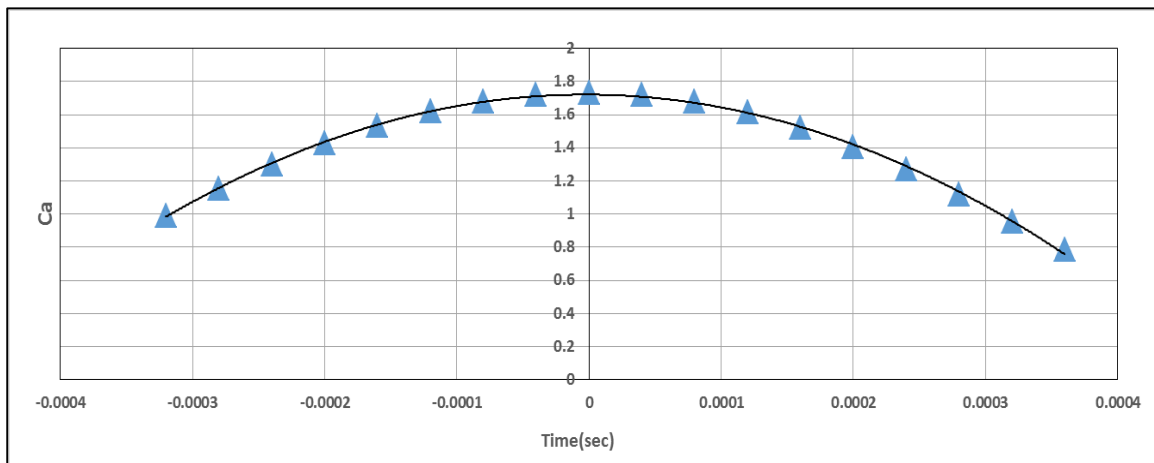


Fig 4.15 Ca added mass coefficient during collision for 3.5cm depth.

Analysing the data for 3.5cm during collision using equation (1.10) , we see that the added mass coefficient values rises and attains its maximum value around 1.7 at the point of impact and drops down gradually.

4.2.3 Depth 5cm Analysis.

4.2.3a Before Collision

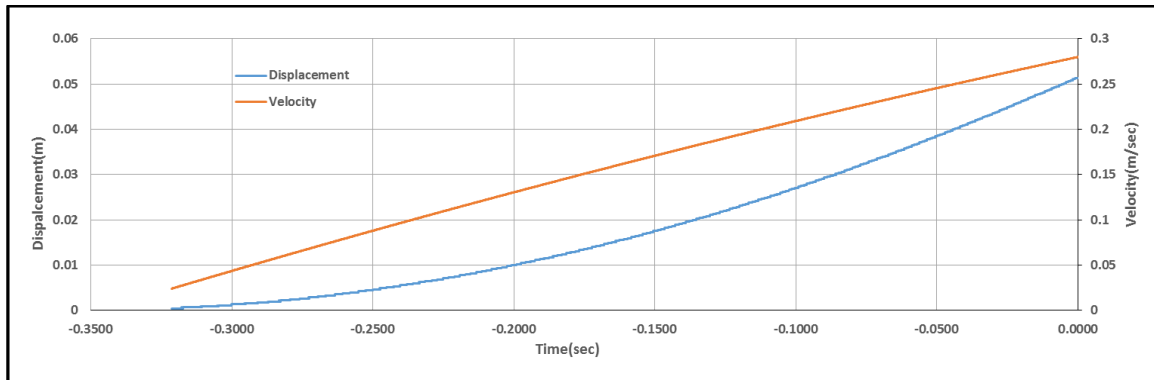


Fig 4.16 Displacement, Velocity before collision for 5cm depth.

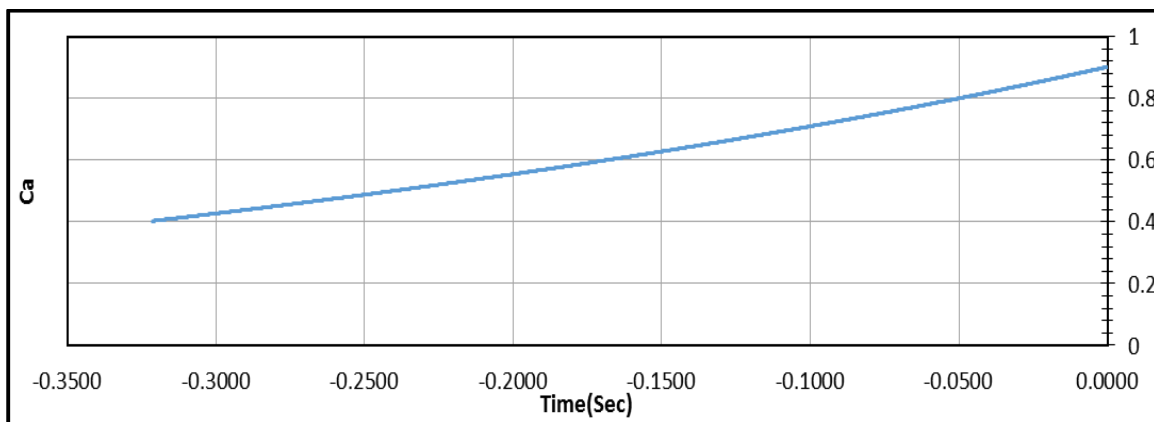


Fig 4.17 Ca added mass coefficient before collision for 5cm depth.

Initial Ca values lies between 0.4-0.6 and rises rapidly as the ice model approches closer to the aluminum plate.

4.2.3b During Collision.

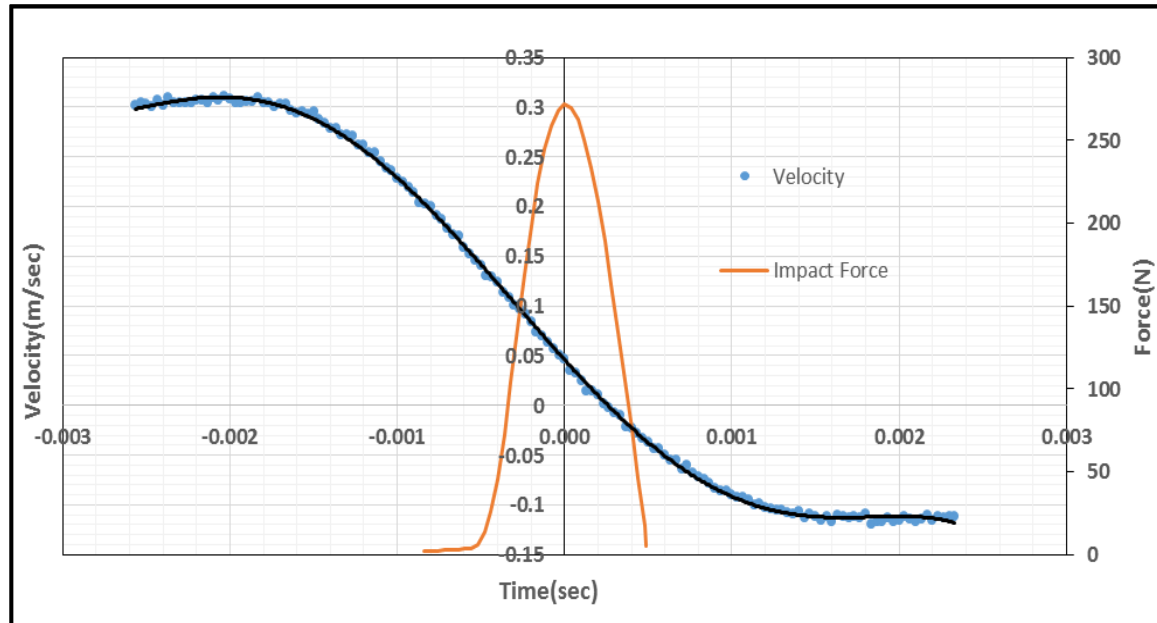


Fig 4.18 Impact force, Velocity during collision for 5cm depth.

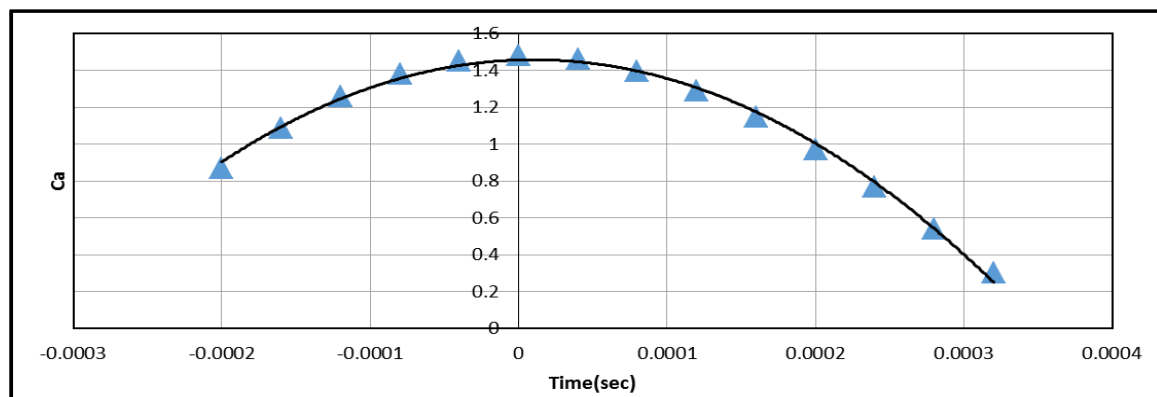


Fig 4.19 Ca added mass coefficient during collision for 5cm depth.

For 5cm depth during collision the added mass coefficient values rises gradually and reaches its maximum value close to 1.47 at the point of impact.

4.2.4 Depth 6.5cm Analysis.

4.2.4a Before Collision

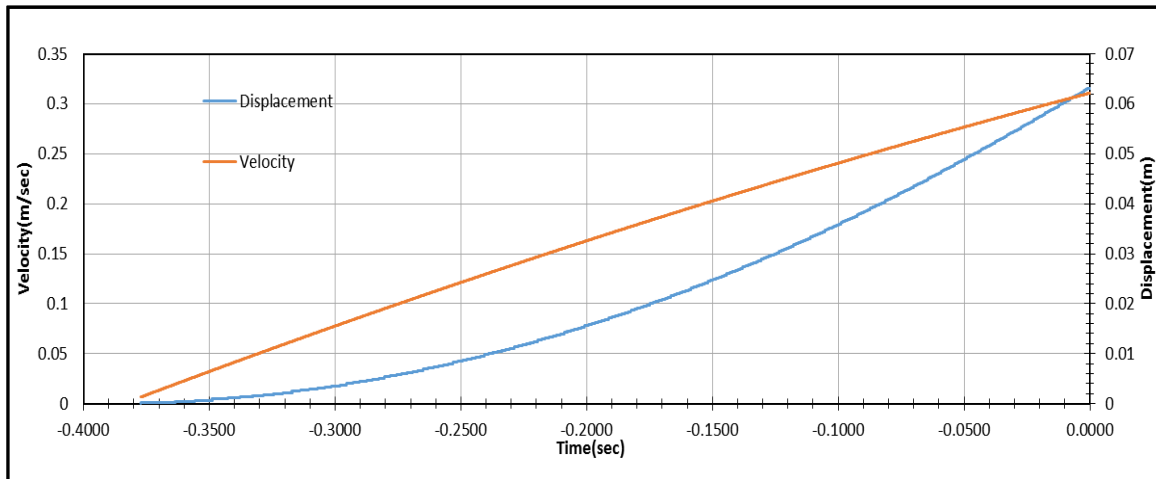


Fig 4.20 Displacement, Velocity before collision for 6.5cm depth.

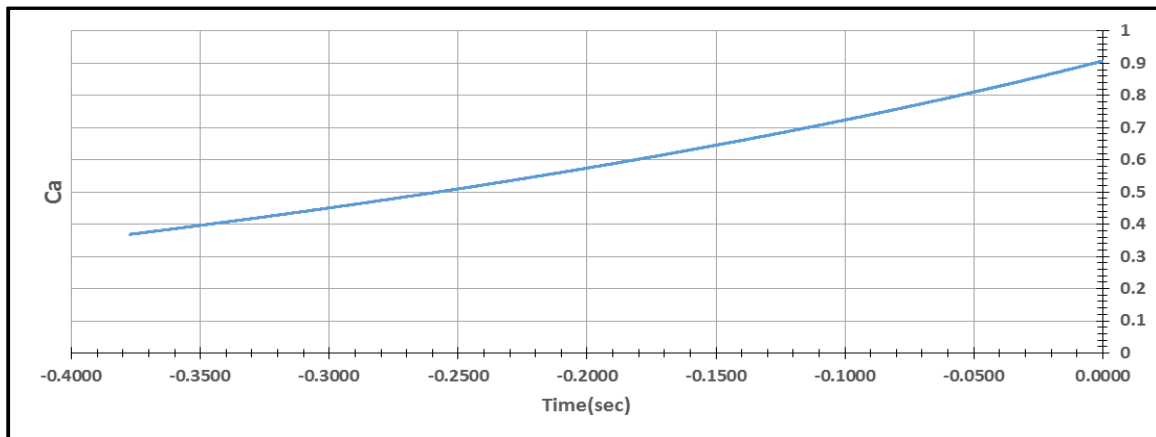


Fig 4.21 C_a added mass coefficient before collision for 6.5cm depth.

Initial Ca values for 6.5cm before collision lies between 0.4-0.6 and rises rapidly as the ice model approaches closer to the aluminum plate.

4.2.4b During Collision

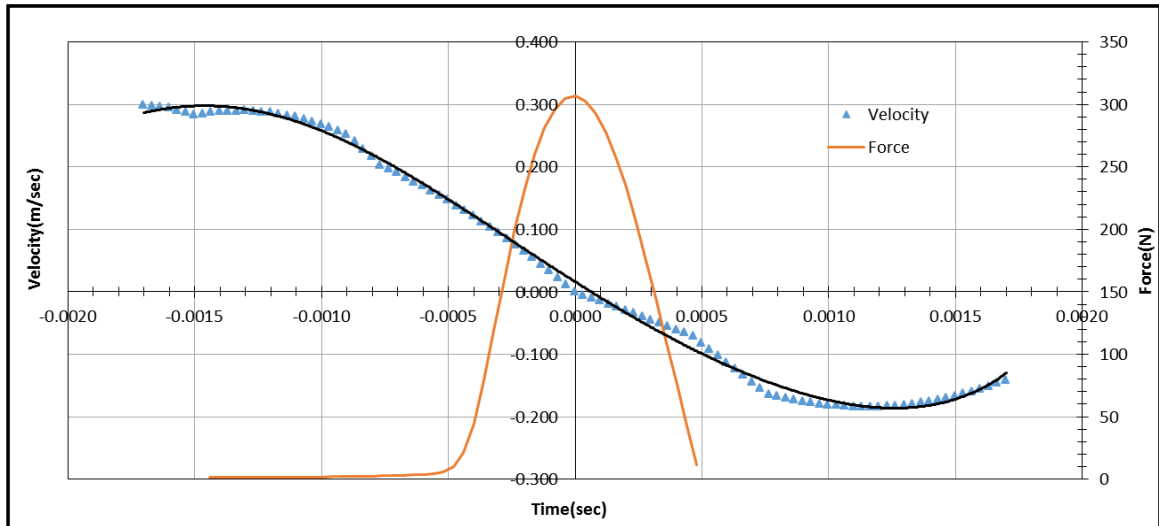


Fig 4.22 Impact force, Velocity during collision for 6.5cm depth.

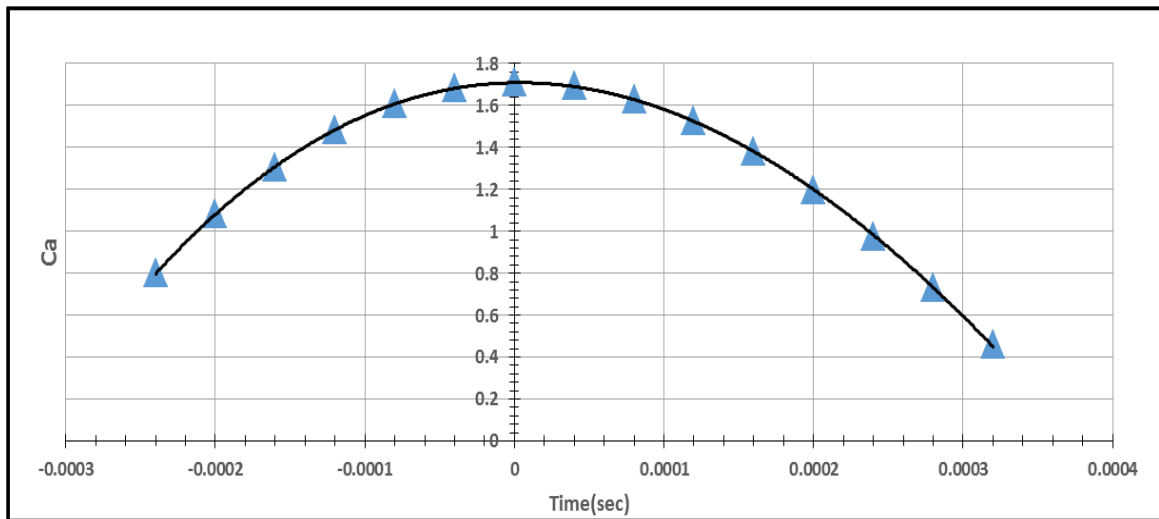


Fig 4.23 Ca added mass coefficient during collision for 6.5cm depth

For 6.5cm depth during collision the added mass coefficient values rises gradually and reaches its maximum value close to 1.709 at the point of impact.

4.2.5 Depth 8cm Analysis.

4.2.5a Before Collision

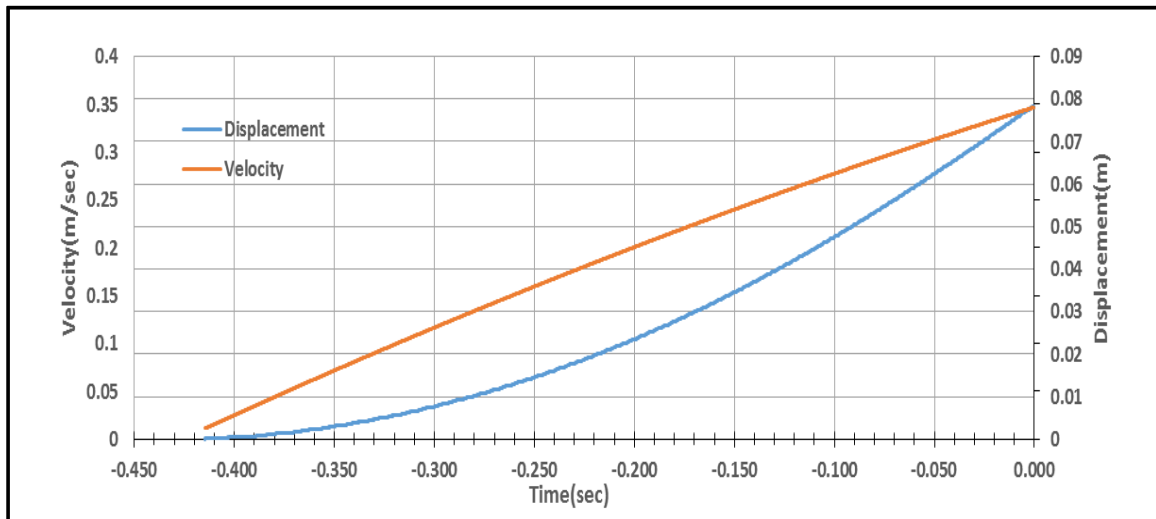


Fig 4.24 Displacement, Velocity before collision for 8cm depth.

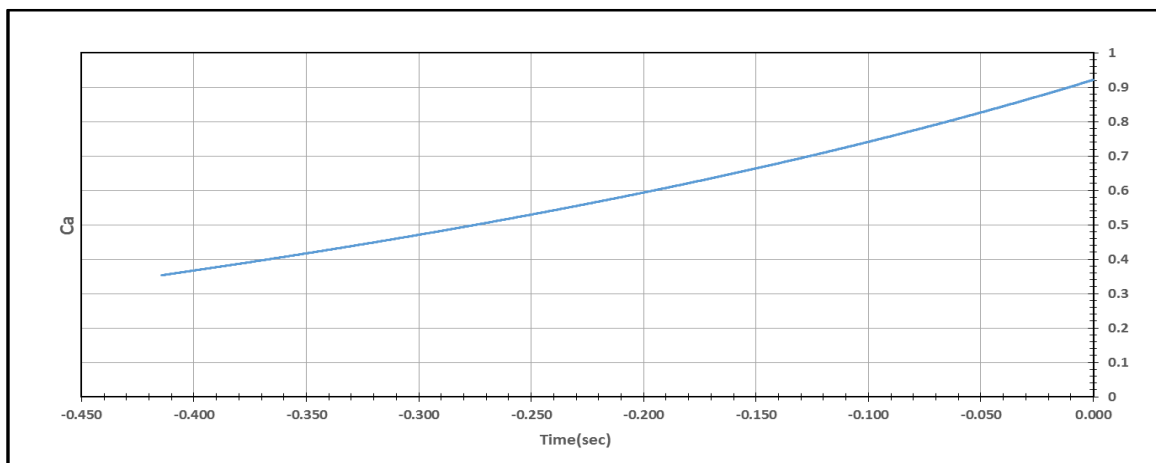


Fig 4.25 Ca added mass coefficient before collision for 8cm depth.

Initial Ca values for 8cm before collision lies between 0.4-0.6 and rises rapidly as the ice model approaches closer to the aluminum plate.

4.2.5a During Collision

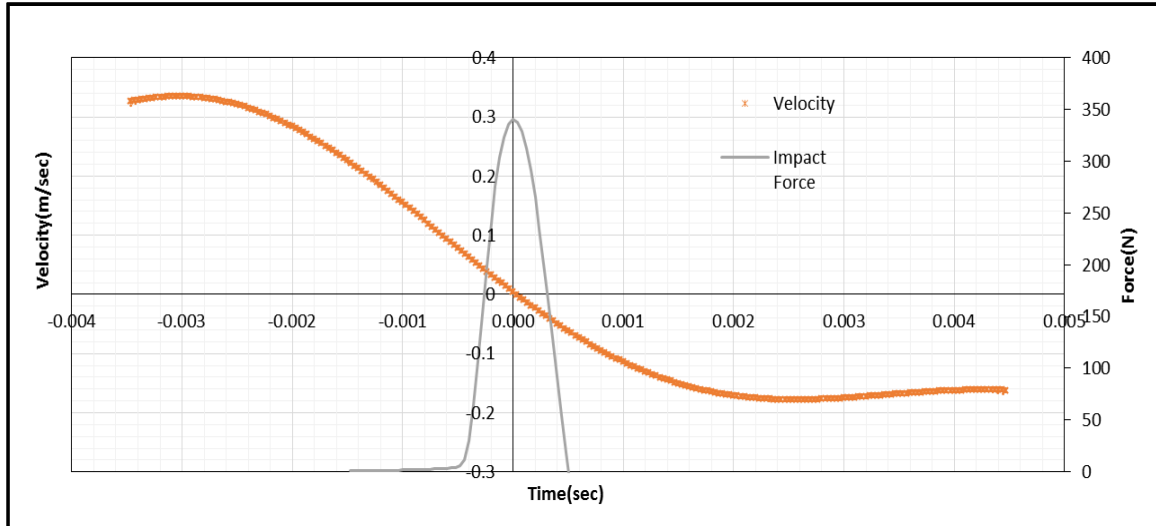


Fig 4.26 Impact force, Velocity during collision for 8cm depth.

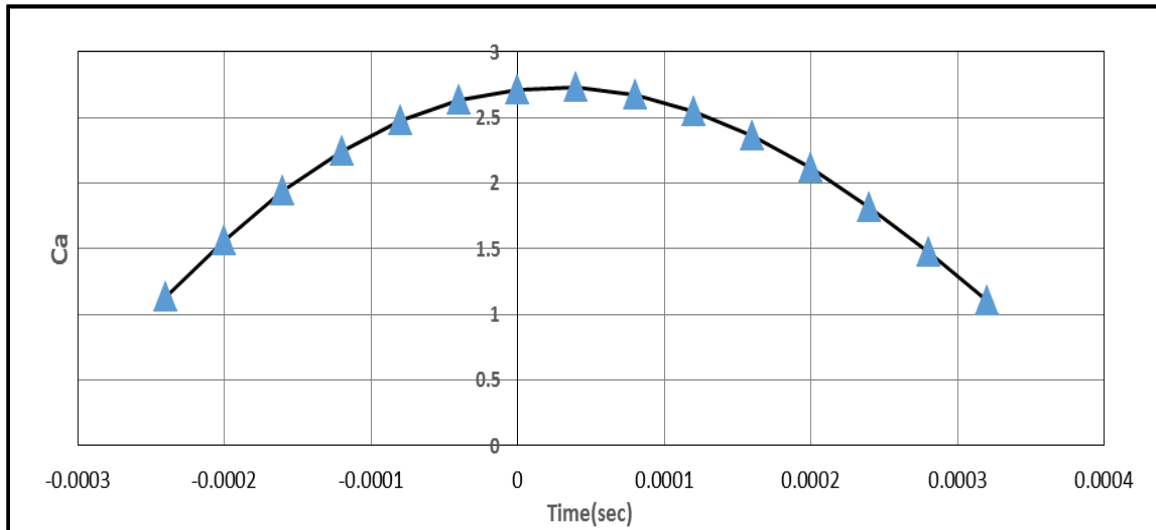


Fig 4.27 Ca added mass coefficient during collision for 8cm depth.

For 8cm depth during collision the added mass coefficient values rises gradually and reaches its maximum value close to 1.709 at the point of impact.

4.2.6 Depth 10cm Analysis.

4.2.6a Before Collision

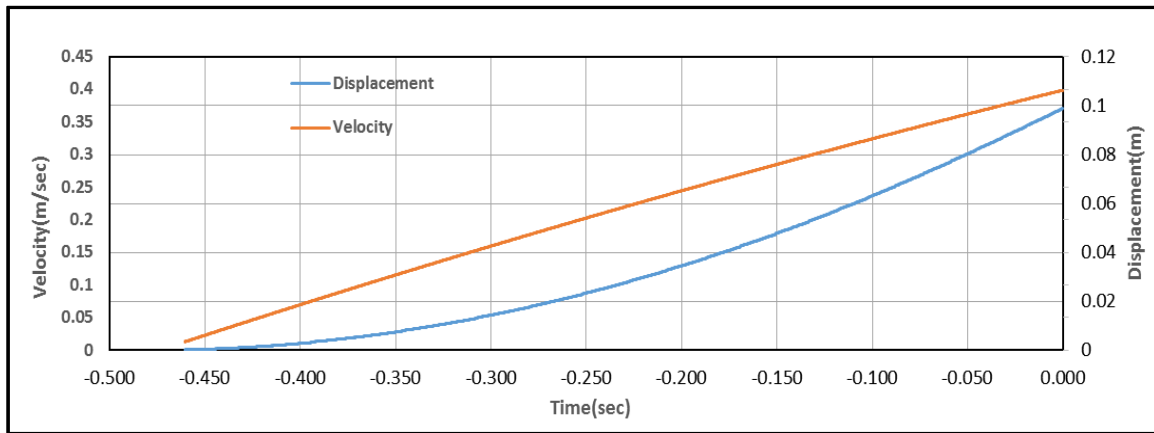


Fig 4.28 Displacement, Velocity before collision for 10cm depth.

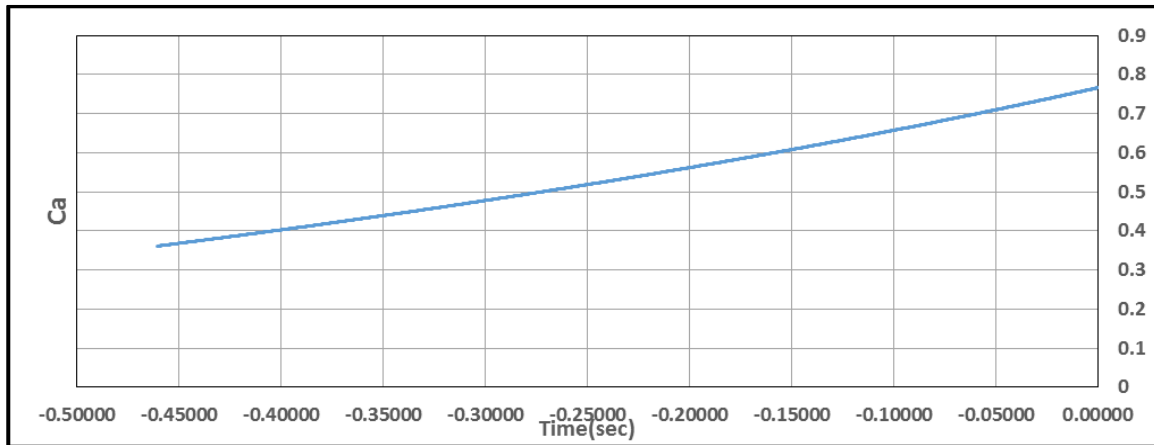


Fig 4.29 Ca added mass coefficient before collision for 10cm depth.

Initial Ca values for 10cm before collision lies between 0.35-0.6 and rises rapidly as the ice model approaches closer to the aluminum plate.

4.2.6b During Collision.

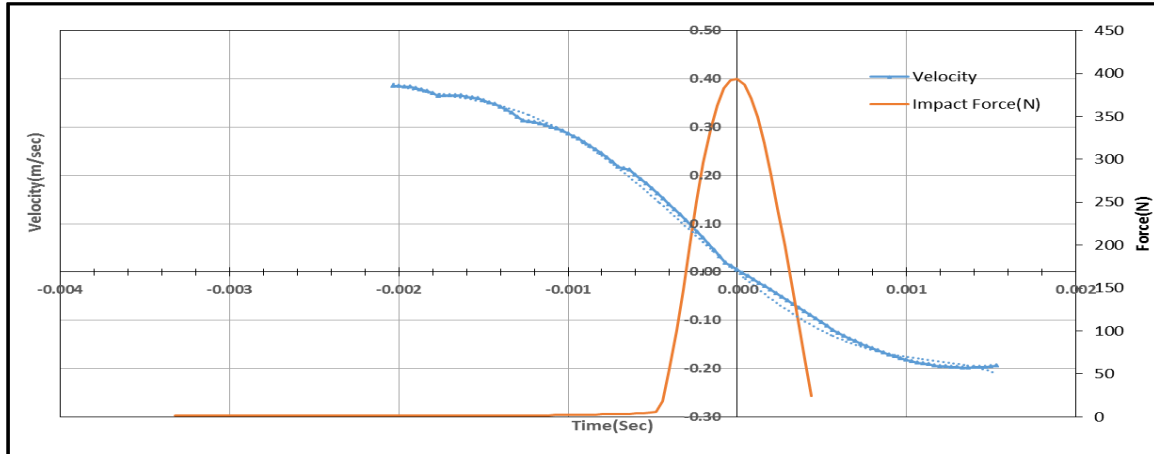


Fig 4.30 Impact force, Velocity during collision for 10cm depth.

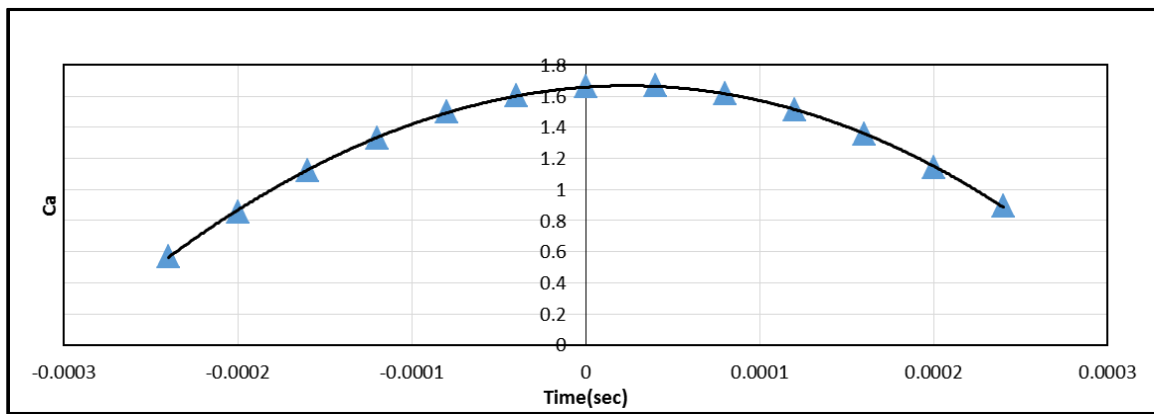


Fig 4.31 Ca added mass coefficient during collision for 10cm depth.

For 10cm depth during collision the added mass coefficient values rises gradually and reaches its maximum value close to 1.63 at the point of impact.

Comparing the added mass coefficient values of before hit tests with the numerical and theoretical study mentioned above we can conclude that the results are in close agreement with the previous research. The velocity in the beginning is very low which gradually increases as the sphere travels towards the plate. For the sub critical reynolds number added mass coefficient values satisfy the potential field theory values. But as the ice model moves close to the aluminum plate, we see a rise in the Reynolds number values. Indicating the onset of turbulent flow around the model.

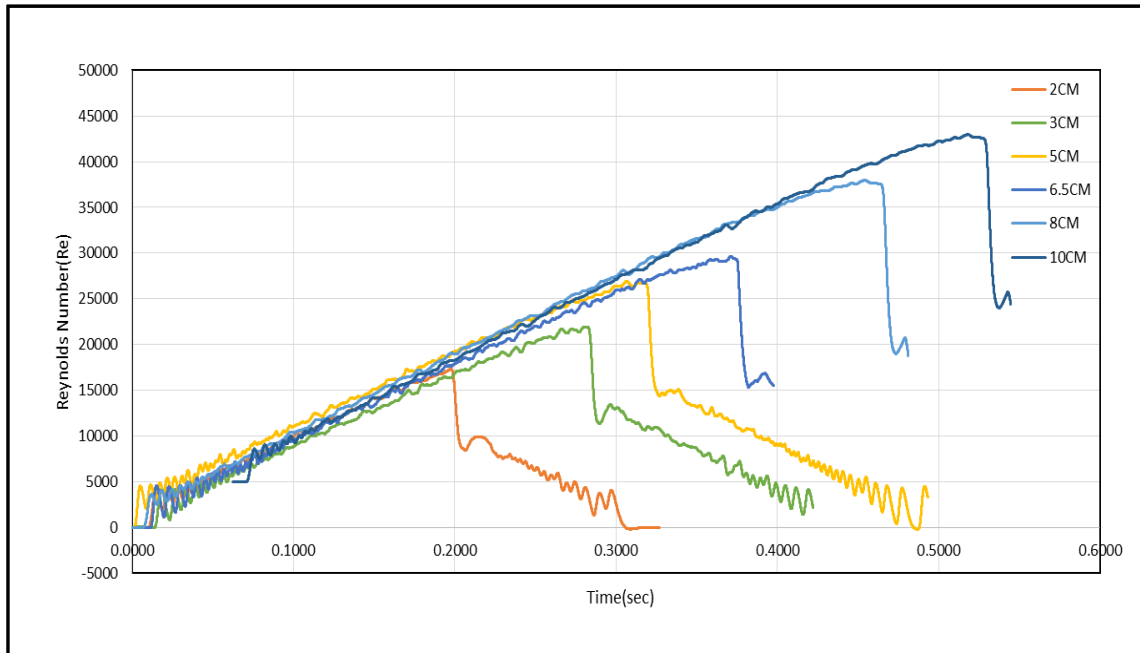


Fig 4.32 Reynolds Number v/s time

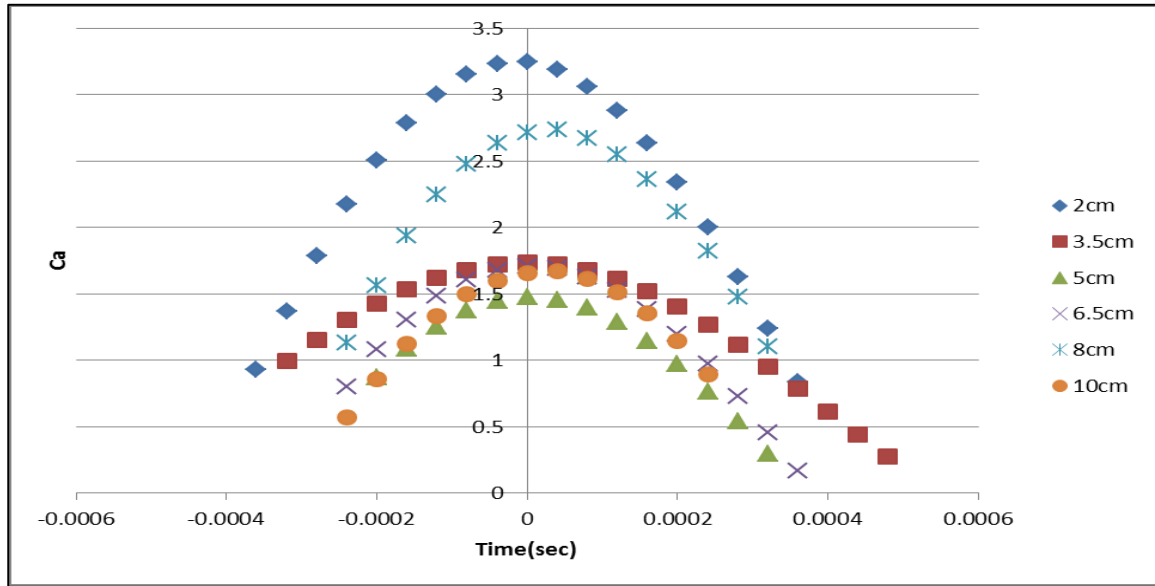


Fig 4.33 Added mass coefficient C_a values during collision.

The collision happens in a very short time interval around 0.001 sec. Most of the numerical studies using potential flow theory do not include this case. The added mass coefficient during collision was determined experimentally using Odar and Hamilton equation for high reynolds number Fig(4.33).

C_a value for 2cm was exceptionally higher compared to other depths. For lower depths the ice model has less distance to cover before it hits the aluminum plate, this gives less time for the development of a turbulent boundary layer, while for higher depths the flow around the sphere gets enough time to achieve a turbulent boundary layer leading to a drop in pressure and further rise in the form drag, the turbulent flow around the body leads to the loss in kinetic energy being transferred to accelerate the fluid around the sphere and hence a sudden drop in added mass coefficients. Also as the ice model moves towards the plate it

creates a pressure wave which gets reflected due to the presence of the boundary and further interacts with the flow around the ice model moving towards the plate. These effects have a significant effect in higher depth tests. Although it was noticed 8cm depth added mass coefficient are exceptionally higher.

4.3 Error Analysis.

Due to the limited availability of the high speed camera only 2cm and 5cm depth tests are repeated twice. While 3.5cm, 5cm, 8cm and 10cm tests are conducted only once. So the error analysis is discussed only for 2cm and 5cm depth.

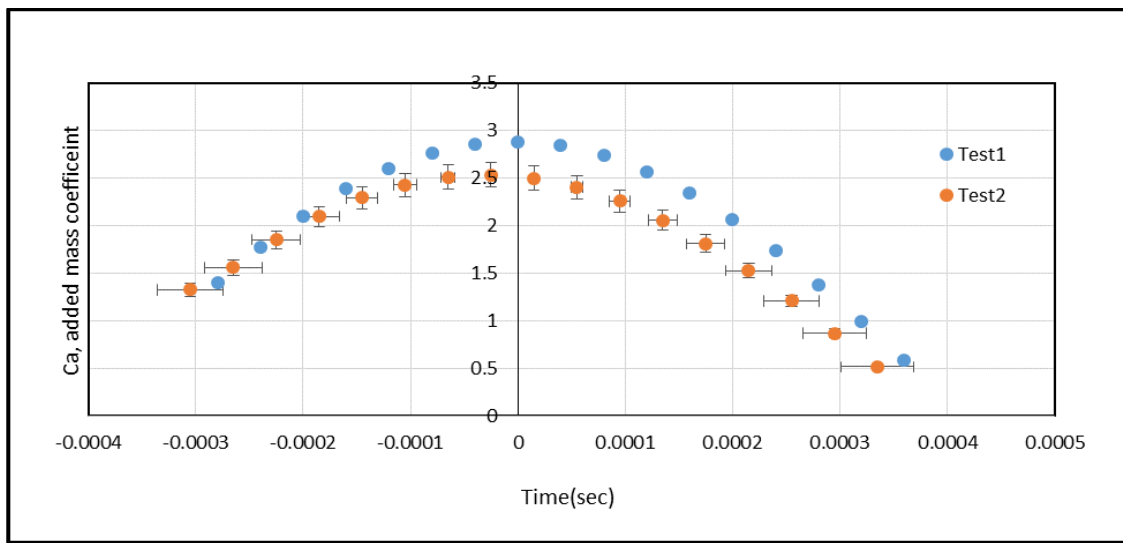
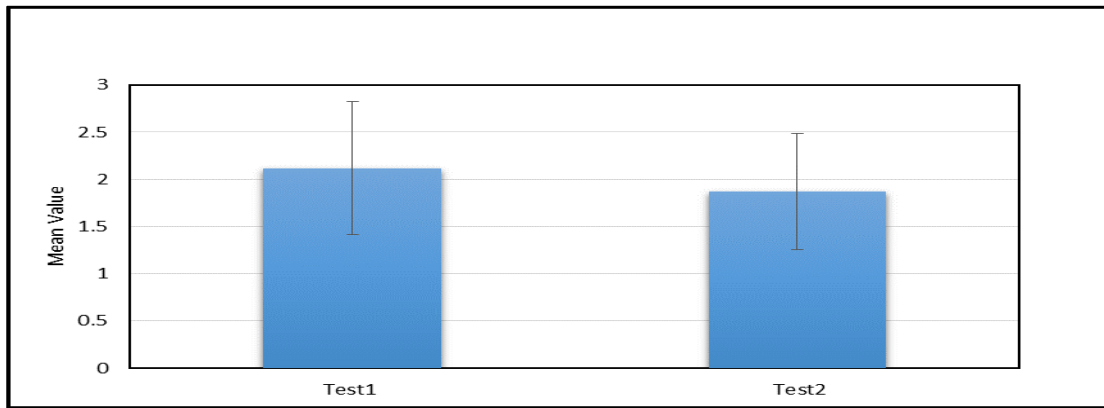


Fig.0) Added mass coefficient plot for tests at 2cm depth .

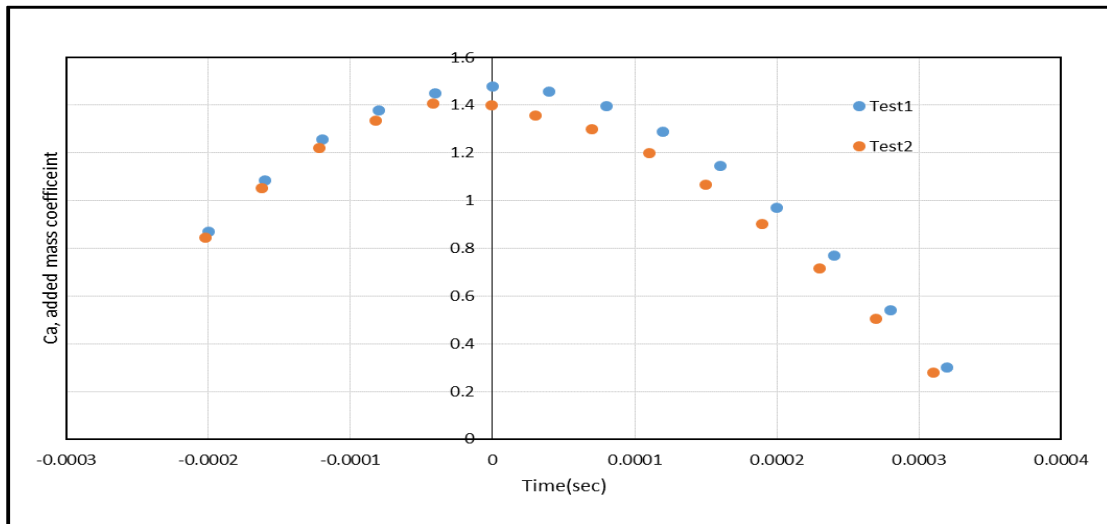


Fig() Mean value of added mass for two tests at 2cm depth

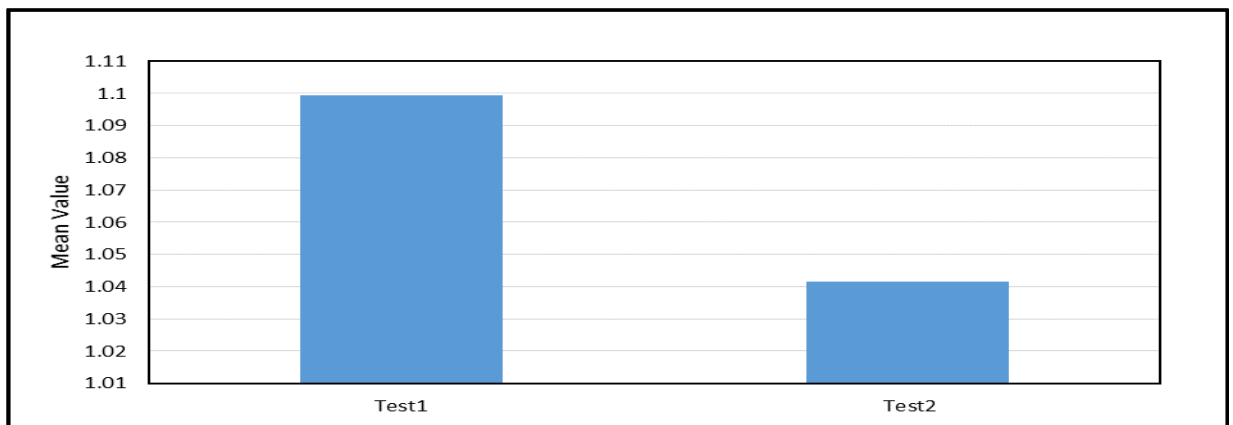
T-test is used to compare the two sets of added mass coefficient values obtained from repeating the 2cm depth test. Where we are assuming null hypothesis, that there is no difference between the two means.

t-Test: Two-Sample Assuming Equal Variances			
		Test 1	Test2
Mean		2.116837	1.868571
Variance		0.495693	0.376688
Observations		17	17
Pooled Variance		0.436191	
Hypothesized Mean Difference		0	
df		32	
t Stat		1.095942	
P(T<=t) two-tail		0.281284	
t Critical two-tail		2.036933	

$P > 0.05$, t-test gives the probability that the null hypothesis is true and there is no significant difference between the means.



Fig(0) Added mass coefficient plot for tests at 5cm depth .



Fig(0) Mean value of added mass for two tests at 5cm depth.

Assuming null hypothesis that there is no difference in the mean of the two tests results.

t-Test: Two-Sample Assuming Equal Variances			
		Test1	Test2
Mean		1.0995	1.041601626
Variance		0.13488	0.123633642
Observations		14	14
Pooled Variance		0.129257	
Hypothesized Mean Difference		0	

df	26	
t Stat	0.42608	
P(T<=t) two-tail	0.673556	
t Critical two-tail	2.055529	

$P > 0.05$, t-test gives the probability that the null hypothesis is true and there is no significant difference between the means

4.4 COEFFICIENT OF RESTITUTION.

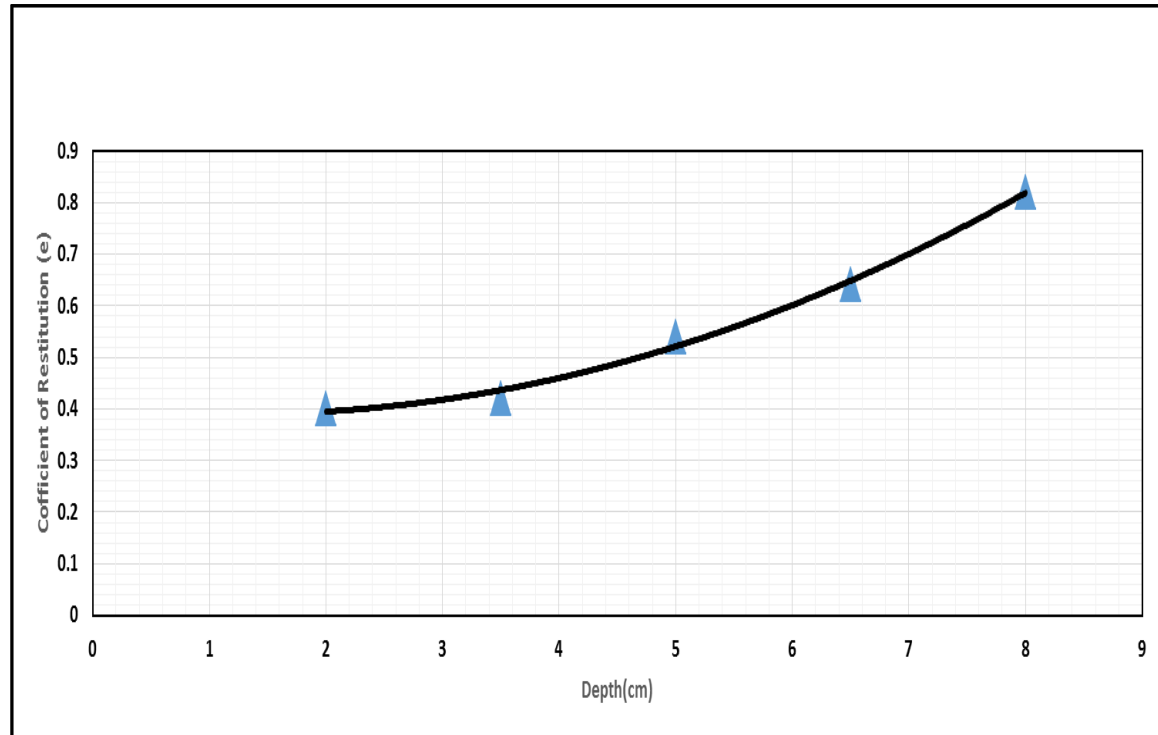


Fig 4.38 Effective Coefficent of Restitution.

The coefficient of restitution characterizes the energy losses during collisions. During the collision, the initial kinetic energy is transformed into elastic strain energy stored in the bodies and then restored into kinetic energy of the rebounding ice model. Under conditions of negligible fluid resistance, the coefficient of restitution can be approximately unity ($e \approx 1$) when the collision is elastic and a negligible amount of energy is absorbed by the interacting bodies as elastic waves. In general, a constant coefficient of restitution is assumed, although it is possible to allow the coefficient to vary due to the presence of fluid effects. The values however are often obtained from idealized experiments that may not be representative of the conditions encountered in applications.

In a similar manner an effective coefficient of restitution may be useful in describing a collision in which the effects of the interstitial fluid are important.

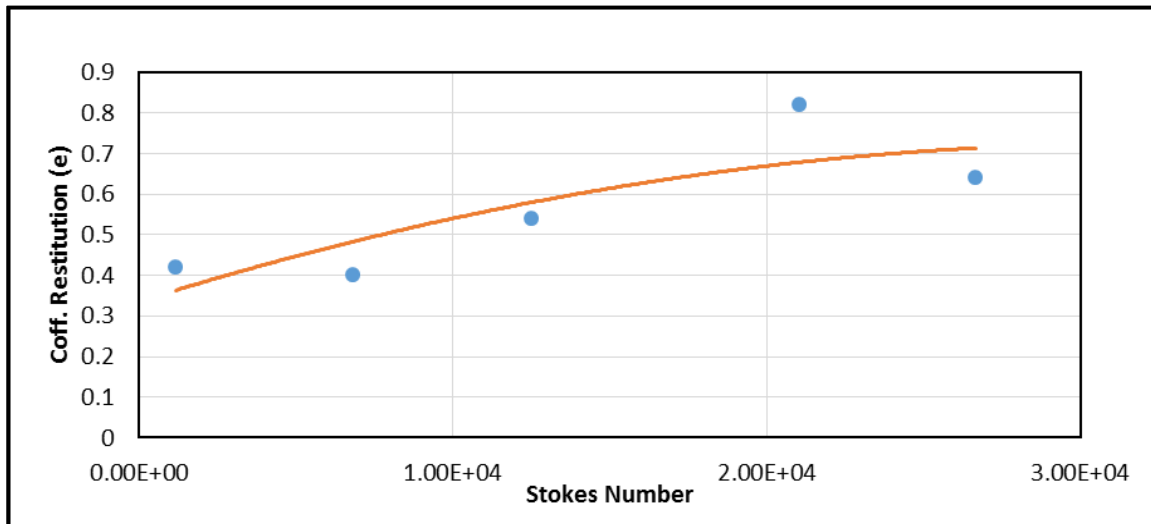


Fig 4.39 Effective Coefficient of restitution of ice model versus Stokes number.

Due to the presence of surrounding fluid the coefficient of restitution values are effected.

As shown in fig.(4.35) the coefficient of restitution increases with the increase in Stokes Number . The coefficient calculated in these experiments is an effective macroscopic value, since velocity is calculated from displacement recorded at 30,000fps which was filtered using the moving average method.

CHAPTER 5 NUMERICAL MODEL

5.1 Meshing.

Flow-3d™ software is used to simulate the motion of underwater spherical ice model moving toward a fixed steel plate. This model is used to conduct numerical experiments and determine the kinematics of the ice model. Flow3d™ uses finite difference method approach to solve the equations of fluid dynamics which is based upon the use of local Taylor expansion to approximate differential equations. The mesh grid is created for the fluid region representing the tank, the mesh is rectangular consisting of hexahedral elements. Mesh planes were used near the ice model and fixed plate boundary. Different mesh sizes were studied. After sensitivity analysis, it was decided to use 6.25 mm mesh along z-axis and 0.028mm mesh near the interface. For X and Y axes we used 5.5mm mesh near the ice model mesh planes and 29mm outside. Although there was a possibility of using much finer mesh size but due to the limited computational resources. FLOW-3D uses FAVOUR™ method to determine the fraction of cell occupied by liquid or solid. This is computed for every cell in the mesh. Before calculating the new velocity field at each time step solid and fluid interface are recomputed, this leads to significant computational burden and longer simulation time.

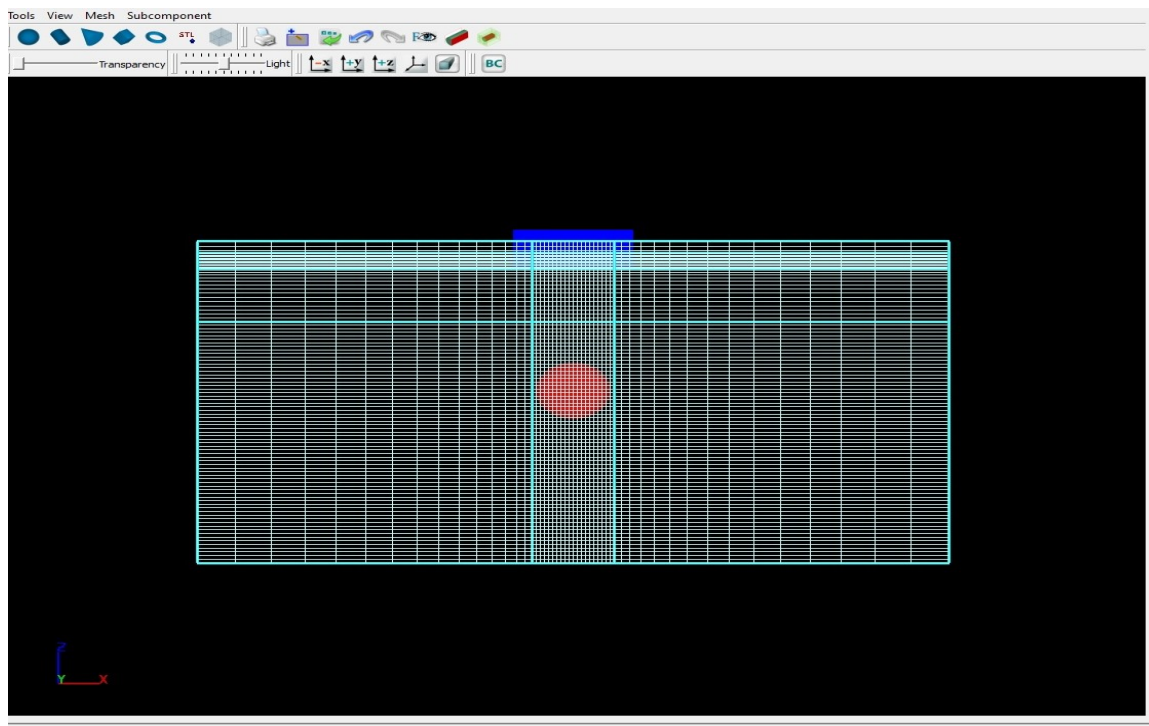


Fig 5.1 Mesh for the underwater ice collision with the aluminum plate.

5.2 GMO Model .

General Moving Object (GMO) model is used to simulate the motion of ice model, which is dynamically coupled with the fluid motion. It uses a 6-dof solver to determine the rigid object (ice-model) motion through the fluid. The coupled motion allows for the multiple

collisions with a fixed plate. For 6-DOF motion, the GMO model selects the object's mass center G as the base point. Equations of motion governing the two separate motions for 6-DOF motion are (Goldstein et al., 2002)

$$\vec{F} = m \frac{d\vec{V}_G}{dt}$$

$$\vec{T}_G = [J] \cdot \frac{d\vec{\omega}}{dt} + \vec{\omega} \times ([J] \cdot \vec{\omega})$$

\vec{F} = Total Force.

m= Mass of the body.

\vec{T}_G = Total torque about G.

[J]= moment of inertia tensor.

\vec{F} = Total force.

$$\vec{F} = \vec{F}_g + \vec{F}_h + \vec{F}_c + \vec{F}_{ni}$$

\vec{F}_g = Gravitational force.

\vec{F}_h = Hydraulic force which is the net effect of pressure and wall shear forces on the moving object.

\vec{F}_c = Net control force such as propulsive thrust force and axis force to control or restrict the object's motion.

\vec{F}_{ni} =Net non-inertial force if the object moves in non-inertial space system.

5.3 VOF Method

Volume of fluid (VOF) method is used to track the free surface location at the water-air interface by solving a set of momentum equations. For each computational cell in a grid a variable for volume of fraction for each phase is introduced. For any given control volume the volume fraction of all phases sums to unity.

If the n^{th} fluid's volume fraction in the cell is denoted by C_n , then ((Flow Inc., User Manual v10).

$$C_n = \begin{cases} 0 & : (\text{the cell is empty of } n^{\text{th}} \text{ fluid}) \\ 1 & : (\text{the cell is full of } n^{\text{th}} \text{ fluid}) \\ 0 < C_n < 1 & : (\text{the cell contains the interface}) \end{cases}$$

Pressure based solver is used to solve the continuity equation in order to use the VOF method.

We are using explicit GMRES (Generalized Minimal Residual) solver, since the number of iterations required are comparatively less compared to other solvers.

5.4 FAVOR (Fractional Area Volume Obstacle Representation)

Flow-3D utilizes TruVOF method for computing free surface motion, and complex geometric regions are modeled using the area/volume obstacle representation (FAVOR) method. In the TruVOF method, a special advection technique is used that gives a sharp definition of the free surface and does not compute the dynamics in the void or air regions. The portion of volume or area occupied by the obstacle in each cell is defined at the beginning of the analysis, and the fluid fraction in each cell is also calculated. The continuity and momentum equations of the fluid fraction are formulated using the FAVOR

function, and the finite volume method or a finite difference approximation is used for the discretization and solving of each equation (Flow Inc., User Manual v10). The program uses a simple grid of rectangular elements, so it has the advantages of ease of generation, regularity for improved numerical accuracy, and requires very little memory storage.

Geometry is then defined within the grid by computing the fractional face areas and fractional volumes of each element that are blocked by obstacles. This Fractional Area Volume Obstacle Representation (FAVOR) method requires that we store three area fractions and one volume fraction for each element, which is relatively little information compared with body-fitted grids.

Although Flow3d™ has superior two-phase modeling capabilities and simulations were easy to setup and simulate it took a lot of time to run the simulations. This is because as FLOW-3D advances a simulation forward in time the FAVOR method is used to determine how much of a cell is occupied by liquids, gases, and solids. This is computed for every cell in the mesh. The solids (walls, moving objects etc.) and fluid interface are then recomputed before the new velocity field is calculated. These extra steps significantly increase the computational burden and result in longer simulation times.

5.5 Boundary Conditions.

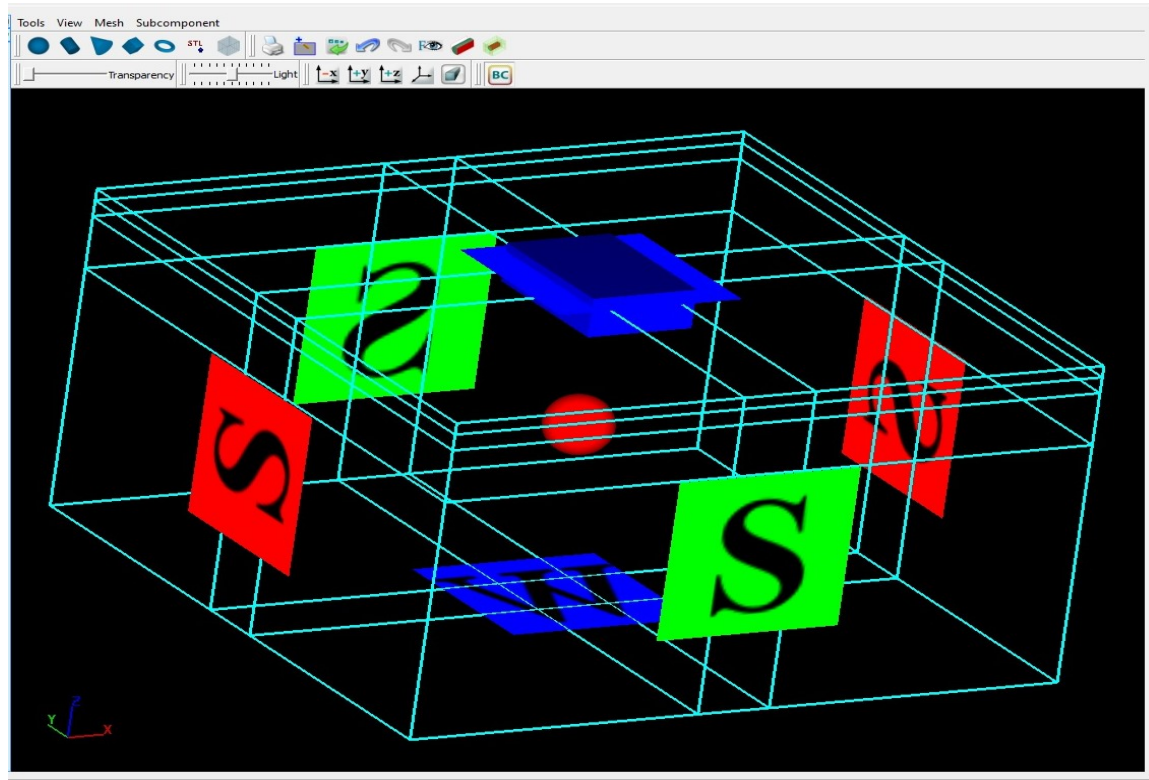


Fig 5.2 Boundary Conditions

A Symmetry Boundary condition was used for adjacent faces of mesh to define the tank boundaries. The bottom mesh plane was defined as a wall boundary condition while the top face was defined as a specified pressure boundary condition with pressure set as a stagnation pressure of 1 atmospheric pressure. Fluid fraction was set to zero for this boundary condition.

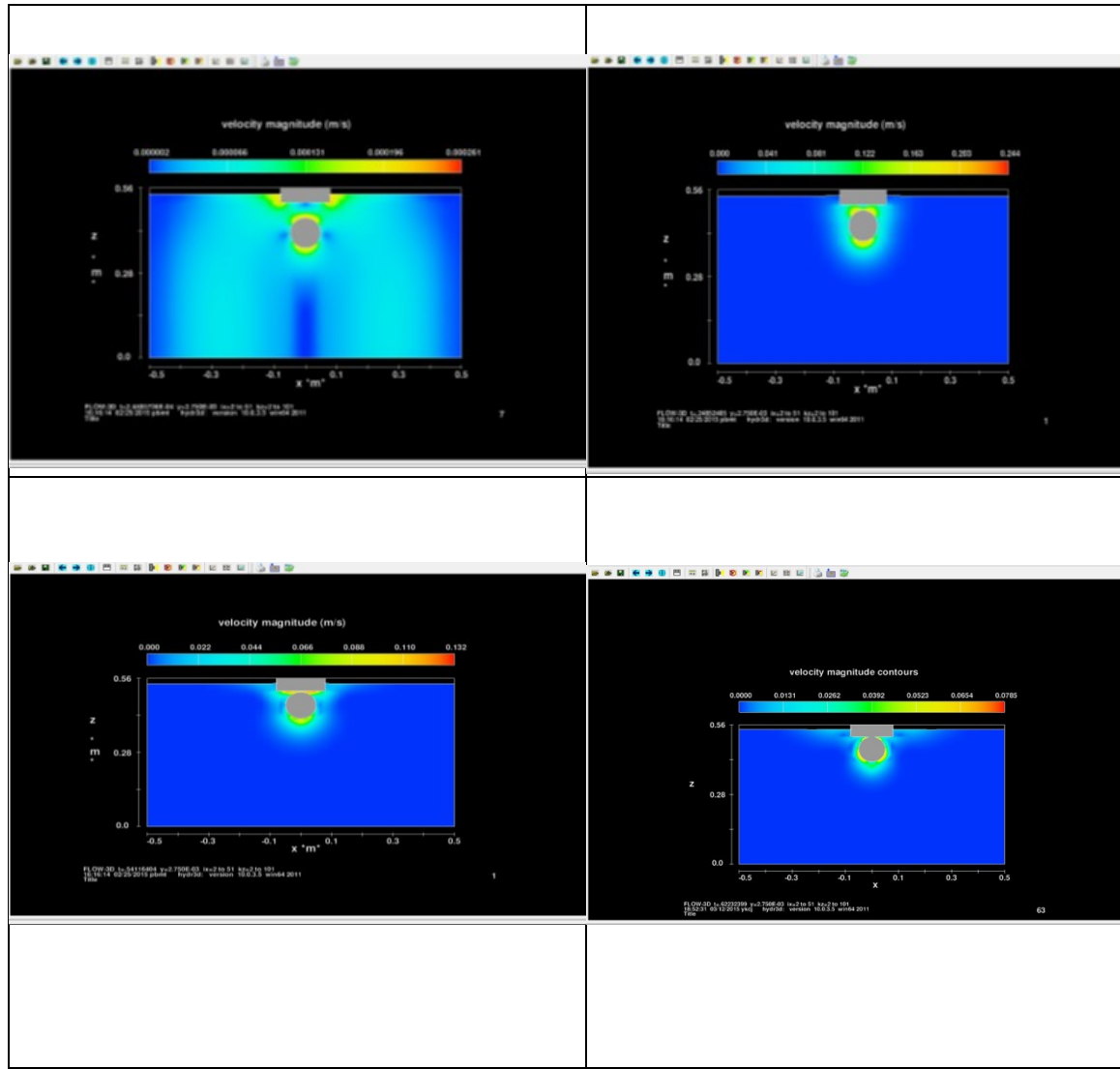


Fig 5.3 Flow3d™ simulation of submerged ice sphere colliding with a solid aluminum plate.

5.6 Comparison of Flow3d Results with Experimental data.

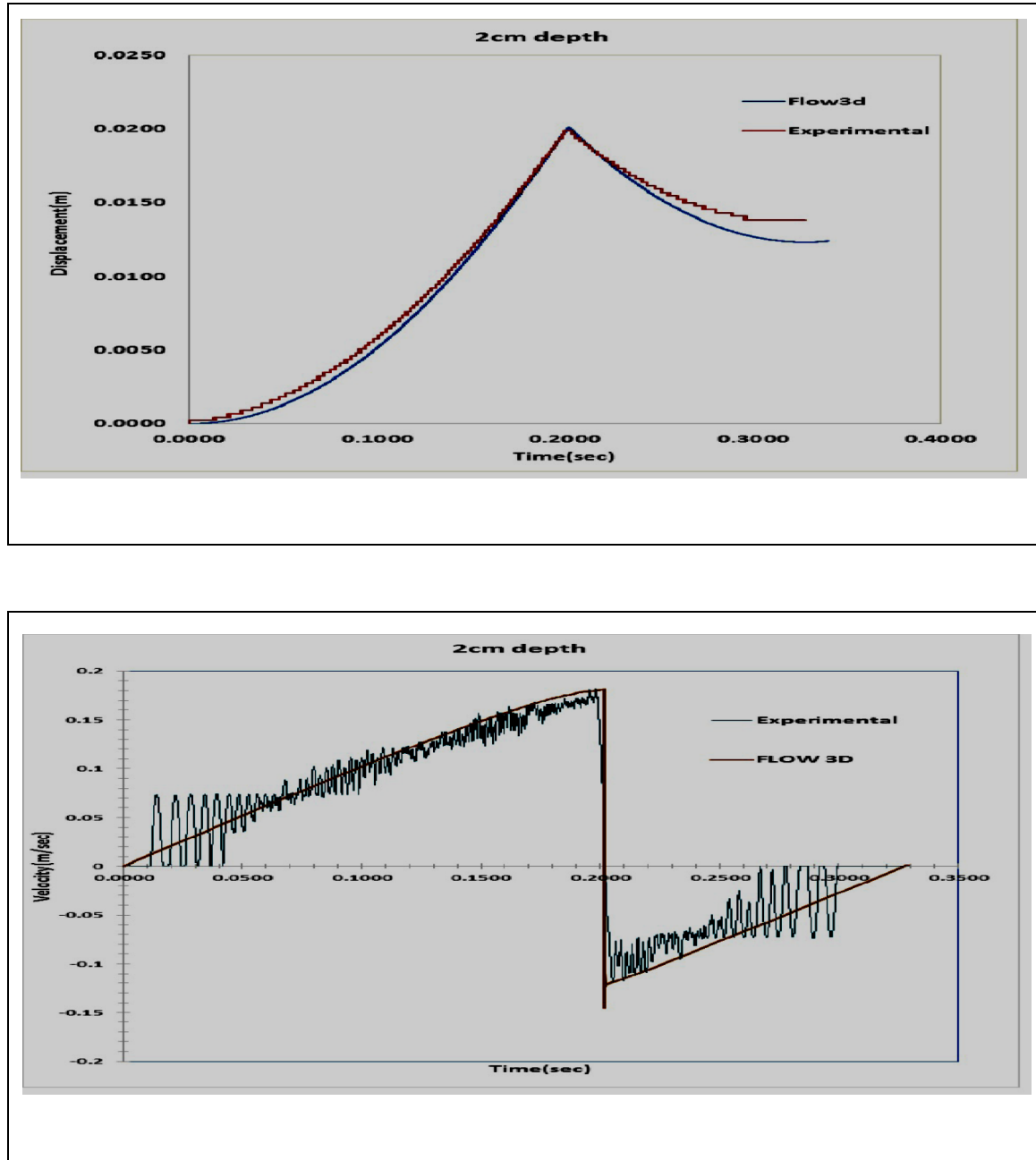


Fig 5.4 Flow3dTM / experimental displacement, velocity data comparison for 2cm depth.

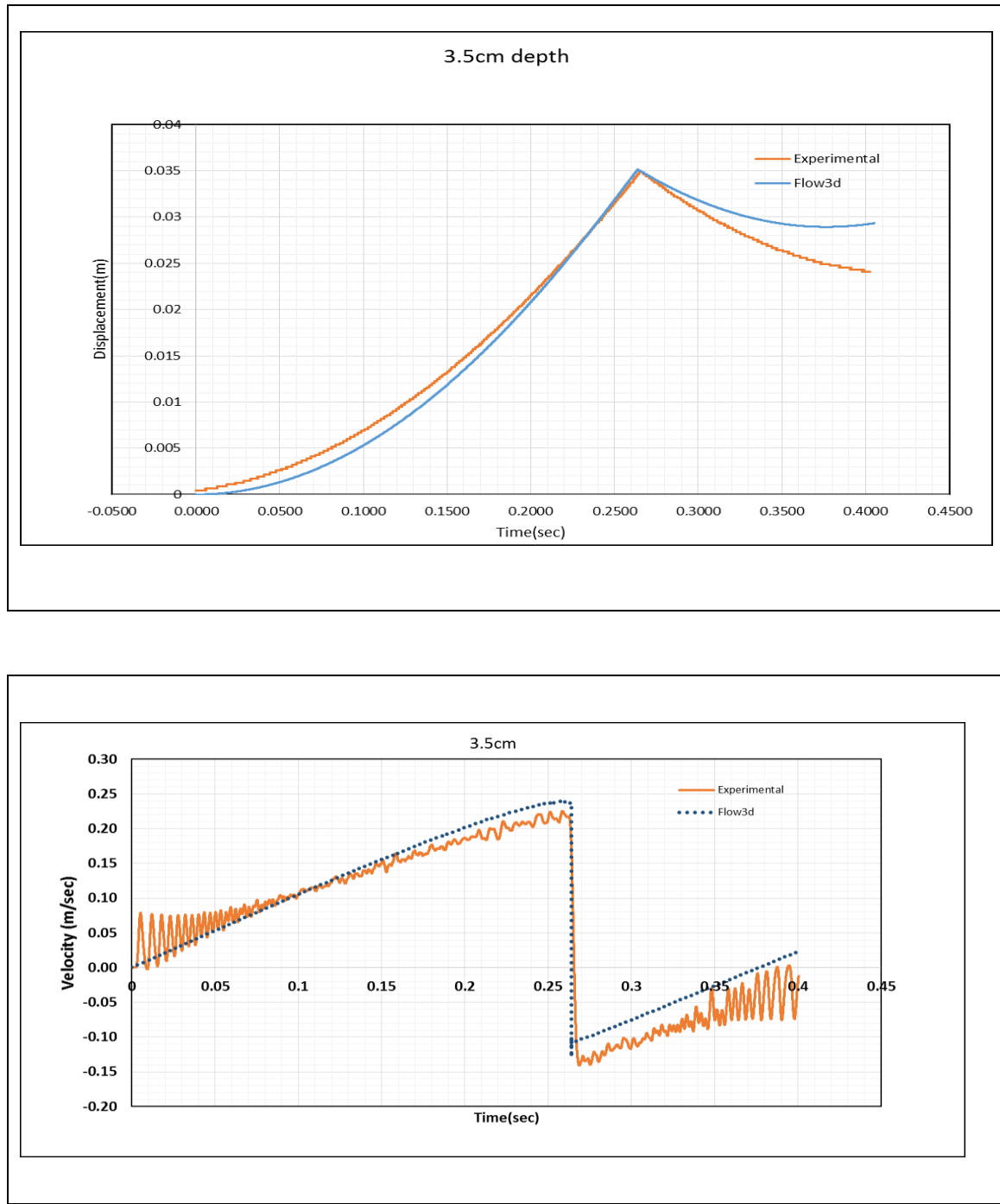


Fig 5.5 Flow3d™/experimental displacement, velocity data comparison for 3.5cm depth.

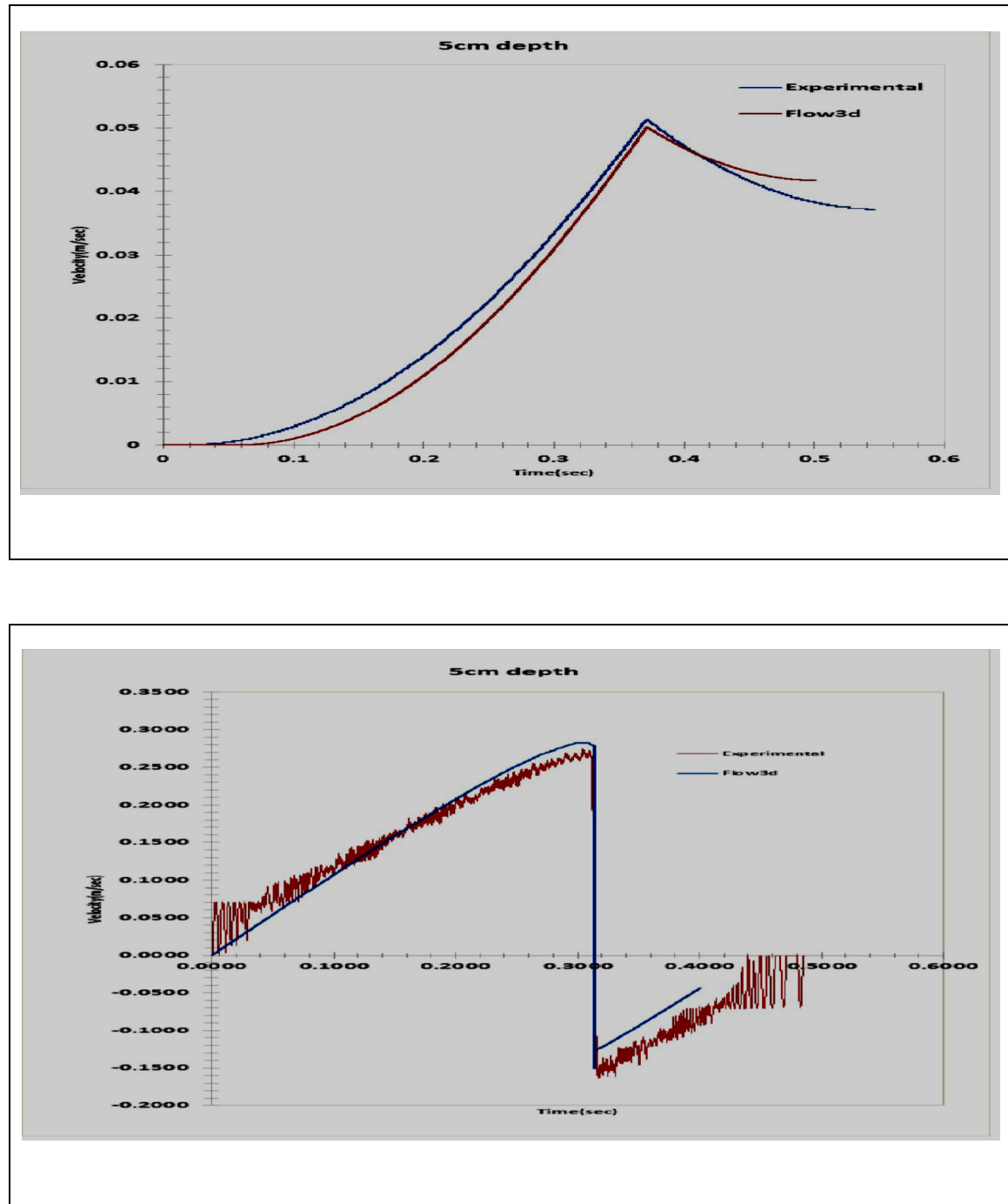


Fig 5.6 Flow3d™/experimental displacement, velocity data comparison for 5cm depth.

On comparing the displacement and velocity data of Flow3d™ simulation of submerged ice collision with a stationary plate for depths 2cm, 3.5cm, 5cm we see a close resemblance in the values of displacement and velocity with the experimental values especially at the point of impact.

The kinematics of this process is an essential determinant of the energy that is available to drive the ice crushing process during the collision. Flow3d™ results were in close agreement with the real values, so this model can be used to further study the kinematics of submerged ice collision with the moving plate, although it does not calculate the impact force values.

CHAPTER 6 CONCLUSION & RECOMMENDATIONS

This research presents an experimental study on the effect of hydrodynamic forces acting on a spherical ice mass at different Reynolds numbers. The purpose of this research was to study the significance of hydrodynamic effects during underwater ice- ship collisions with particular emphasis on added mass and the kinematics of the collision.

The actual indentation of the ice model was not included in this research in order to simplify the hydrodynamic calculations.

The results show that the added mass is influenced by the presence of a solid boundary, and the surrounding fluid flow. Added mass was equivalent to the theoretical values in the low Reynolds number region. In general added mass increases as the spherical model approaches the plate. This was consistent with the numerical studies done using potential flow theory. There was a noticeable rise in added mass coefficient values for lower depth tests compared to the higher depths which was due to the onset of turbulent flow during higher depth tests. This indicates that the change in added mass will be influenced by the velocity of approach and possibly the distance traveled before impact.

The numerical results of displacement and velocity using Flow3dTM shows a close correspondence with the experimental data. Although Flow3dTM does not calculate the impact forces during the collision but the kinematics results were in close agreement with the experimental data.

The results show that the added mass coefficient of an ice model in close proximity to the hull is not only dependent on the geometry of the ice but also on the distance from the hull, the velocity of approach and the nature of fluid flow.

The impact velocity for each test 2cm, 5cm, 8cm were calculated from the experimental data and a numerical model using LS DYNA™ to calculate the impact forces using the experimental impact velocity but excluding the hydrodynamic effects was designed by a fellow researcher Xiaoli Gao. The LS DYNA™ model was validated using drop tests data of spherical ice model in air from different depths on the plate connected with load cell unit. The idea was to determine the impact forces for the similar impact velocity as calculated from experimental data for different depths of submerged collisions but excluding the hydrodynamic effects, in order to compare the impact forces in both the cases. On comparing the LS DYNA™ impact force data, which excludes the hydrodynamic forces, with the load cell data from the submerged collision, which includes the effect of hydrodynamics, it was found that due to the presence of the fluid the impact force has much higher value compared to the model where hydrodynamic forces were excluded.

	LS-Dyna Model No Hydrodynamic Effects	Experimental data With Hydrodynamic effects
Depth(cm)	Force(N)	Force(N)
2	105.2	140
5	180.9	270
8	210.2	337.9

During the submerged collision the impact force values were higher than the impact force without the fluid effects. This can be explained due to the additional term added mass which

increases the total momentum being imparted to the structure during collision. These tests shows that the added mass coefficient value stays close to 0.5, at a distance 2 times the radius of sphere, which is similar to that of a spherical object moving in an unbounded fluid region, but as the model approaches close to the aluminium plate the added mass coefficient values starts rising and attains it maximum value at the point of collision. These tests show that the added mass increases the impact force during the submerged collision, although effects of wave and velocity due to the moving model have not been included.

This research gives an initial starting point to understand the submerged ice collision with the underwater portions of a ship hull. To understand the effects of the motion of ship model and the interaction of waves, the model should be towed in the towing tank at different velocity and ice model released to collide with the underwater load cell unit attached to the hull, further the model can be towed on top of the floating ice pieces to study the effects of submergence and friction on the impact. The different bow shapes are designed which can be easily attached to the hull and can be used to study the effect of bow angle on the sliding and friction of ice pieces during submergence.

Another future work can be improving the image analysis methodology in order to reduce the noise in data and more accurate values of velocity and acceleration at the point of impact.

Although FLOW3D™ models the kinematics of collision correctly, numerically calculating the impact force value for submerged ice collision which includes the hydrodynamic effects is still a challenge.

Bibliography

Du Buat, C., 1786. Principles D'hydraulique, Paris.

Barnocky, G. & Davis, R. H. 1988. Elastohydrodynamic collision and rebound of spheres: experimental verification. *Phys. Fluids* **31**, 1324.

Basset, A.B., 1910. Descent of a Sphere in Viscous Liquid. *Nature*. Vol. 83, pp. 369-381.

Clift, R., Grace, J. R. and Weber, M. E., 1978. Bubbles, Drops, and Particles. *Academic Press, New York, NY*.

Lamb, H., 1945. Hydrodynamics, 6th Ed.. *Dover Publications, New York, NY*.

Colbourne, D.B., 1989. A three component method of analyzing icebreaking resistance. *Ph.D. thesis Memorial University of Newfoundland, Canada*.

Cox, S.J. & Cooker, M.J., 2000. Potential Flow past a sphere touching a tangent plane. *Journal of engineering mathematics* 38:355-370.

Chung, S. & Chen, S.S., 1976. Hydrodynamic Mass. *Component Technology Division, Argonne National Laboratory, Argonne, Illinois.*

Daley, C., 1999. Energy based ice collision forces. *15th International conference on ports and ocean engineering under arctic conditions, Finland.*

Davis, A.M.J., 1976. High frequency limiting virtual mass coefficient of heaving half immersed sphere. *Journal of Fluid Mechanics, Vol.80, part-2, pp. 305-319.*

Gao, X., 2015 Assessment of Modeling Underwater Impact Using ICFD of LS-DYNA. *Master thesis (unpublished manuscript), (2015).*

Goldstein, H., Poole, C., Safko, J., 2002. Classical Mechanics 3rd edition. *Addison Wesley, San Francisco, CA.*

Hicks, W.M., 1880. On the motion of two spheres in a fluid. *Roy. Soc. Lond. Trans. Ser. A, 171: 455-492. 1880.*

Hamilton, W. and G. Courtney, 1977. Added Mass of Sphere Starting Upward Near Floor. *ASCE J Eng Mech Div, Vol. 103, No. 1, 79-97.*

Joesph, .G.G., Zenit, R., Hunt, M.L. & Roesninkel A.M., 2001. Particle wall collision in a viscous fluid. *Journal of Fluid Mechanics, Vol 433, 329-346.*

Lamb, H., 1945. Hydrodynamics, 6th Ed., *Dover Publications, New York, NY.*

Odar, F. & Hamilton, W.S., 1964. Forces on a sphere accelerating in a viscous fluid.
Journal of fluid mechanics, Vol.18, Issue 2, pp302-314.

Patton, K.T., *Tables of Hydrodynamic Mass Factors for Translational Motion*, in
American Society of Mechanical Engineers - Meeting WA/UNT-2, American
Society of Mechanical Engineers (ASME), New York, NY, United States, 1965

Pederson, P.T., Zang, S., 2015. The mechanics of ship impacts against bridges.
Proceedings of International symposium on advances in ship collision analysis,
Copenhagen.

Rostami, M., Ardeshir, A., Ahmadi, G., Thomas, P.J., 2006. On the motion of high
Reynolds particle in a quiescent fluid. *AmairKabir Journal of science and technology,*
Vol.17, No.64-B(Mechanical Engineering).

Stokes, G.G., 1843. On some cases of fluid motion. *Camb. Phil. Soc. Trans. 8:* 105-137.

Sarpkaya, T. and Isaacson, M., 1981. Mechanics of Wave Forces on Offshore Structures,
Van Nostrand Reinhold Company, NY.

Thomson, M., 1968. Theoretical Hydrodynamics 5th Edition. *Dover Publications, New York, NY.*

REFRENCES

Alexander, P., 2004. High order computation of the history term in the equation of motion for a spherical particle in a fluid. *J.Sci. Comput.* 21 (2004) 129134

Brennen, C.E., 1982, A review on added mass and fluid inertial forces. *Naval civil engineering lab, California*

Fernandes, P.C., Risso F., Ern P, Magnaudet J. 2007. Oscillatory motion and wake instability of freely-rising axisymmetric bodies. *J. Fluid Mech.* 573:479–502.

Lee, T., Chartrand, R., and Asaki, T.J.,2007. A vibrational approach to reconstructing images corrupted by Poisson noise. *J. Math. Imaging Vision*, vol. 27, pp. 257–263.

McLaughlin,M. An experimental study of particle-wall collisions relating to flow solid particles in a fluid. *Ph.D. Thesis, California Institute of Technology (1968)*.

Meyerhoff, W.K., 1970. Added masses of thin rectangular plates calculated from potential theory. *J Ship Res* 1970;14(2):100–11.

Masmoudi, M., Lecoq, L., Anthore, R., Bostel, F., Feuillebois, F., 2002. Accurate measurement of hydrodynamic interactions between a particle and walls. *Experiments in Fluids* 32, Springer-Verlag.

Patton, K.T., 1965. Tables of Hydrodynamic Mass Factors for Translational Motion, *American Society of Mechanical Engineers - Meeting WA/UNT-2, American Society of Mechanical Engineers (ASME), New York, NY, United States.*

Sarpkaya, T., 1977. In-Line and Transverse Forces on Cylinders in Oscillatory Flow at High Reynolds Numbers. *Journal of Ship Research*, Vol. 21, No. 1, pp. 200-216.

Sarpkaya, T., 1975. Forces on Cylinders and Spheres in a Sinusoidally Oscillating Fluid. *Journal of Applied Mechanics, Transactions ASME*, Vol. 42, No. 1, pp. 32-37.

Sarpkaya, T., 1966. Separated Flow about Lifting Bodies and Impulsive Flow about Cylinders. *AIAA Journal*, Vol. 4, No. 3, pp. 414.

Appendices

Appendix A: Matlab Code For Image Processing And Object Tracking.

```

clear all
clc

directory = 'C:\Hydrodynamic Tests\5.0cm\' ;
directory1 = 'C:\Hydrodynamic Tests\5.0cm\results\' ;

FPS = 2000;
N_of_frames_begin = 1;
N_of_frames_delta = 1;
N_of_frames_end = 4500;

f1 = 'July 3_5cm_3_';
for i = N_of_frames_begin:N_of_frames_delta:N_of_frames_end
    if i < 10
        fnames(i,:) = strcat(f1, '0000',num2str(i),'.bmp');
    elseif i < 100
        fnames(i,:) = strcat(f1, '000',num2str(i),'.bmp');
    elseif i < 1000
        fnames(i,:) = strcat(f1, '00',num2str(i),'.bmp');
    else
        fnames(i,:) = strcat(f1, '0',num2str(i),'.bmp');
    end
    file_path = strcat(directory,fnames(i,:))
    I=imread(file_path);
    %figure(1); imshow(I)
    I4 = I(13:240,215:410,1);

    figure(1); imshow(I4)

    H = image(I);
    my_map = get(gcf,'Colormap');

    I5 = ind2gray(I4,my_map);

    figure(2); imshow(I4)

    %adding contrast%
    ad=im2double(I4);
    x=ad;

```

```

[r,c]=size(ad);
factor=2.5;
for m =1:r
    for n =1:c
        x(m,n)=factor*log(1+ad(m,n));
    end
end

figure(3), imshow(x);
I6 = imadjust(x);
imshow(I6)

I3 = imadjust(I6);
figure(3), imshow(I3);

level = graythresh(I3);
bw = im2bw(I3,level);
bw = bwareaopen(bw, 2000,8);
figure(4), imshow(bw)

imwrite(bw,strcat(directory1,fnames(i,:)));
bw_1 = edge(bw,'sobel');
figure(99);      imshow(bw_1)

cc = bwconncomp(bw, 8);

cc.NumObjects;

if cc.NumObjects > 0
    N =1;
    grain = false(size(bw));
    grain(cc.PixelIdxList{N}) = true;
    figure(103), imshow(grain);

graindata = regionprops(cc, 'basic');
graindata(N).Area;
graindata(N).Centroid;
graindata(N).BoundingBox;

```

```
Area(i) = graindata(N).Area;
Centroid_x(i) = graindata(N).Centroid(1);
Centroid_y(i) = graindata(N).Centroid(2);
BBox_1(i) = graindata(N).BoundingBox(1);
BBox_2(i) = graindata(N).BoundingBox(2);
BBox_3(i) = graindata(N).BoundingBox(3);
BBox_4(i) = graindata(N).BoundingBox(4);
end
end

figure(201);
plot(BBox_1,'r.')
figure(202);
plot(BBox_2,'r.')
figure(203);
plot(BBox_3,'r.')
figure(204);
plot(BBox_4,'r.')

t = (1/FPS) * [0:N_of_frames_end-1];
cd(directory1);

save('test_999.txt','t','Centroid_x','Centroid_y','BBox_1',
'BBox_2','BBox_3','BBox_4',' -ascii',' -tabs')
```

Appendix B: Matlab code to filter data using “Moving Trend line Method”.

```
clc  
clear all  
directory ='C:\Users\Subodh\Documents\MATLAB\data6p5.txt';  
load data6p5.txt  
t= data6p5(:,1);  
d = data6p5(:,2);  
  
l = 10      %Specify the number of initial data points to be selected%  
deg = 2;    % degree of fitting curve%  
n = length(d);  
start_point = l +1 % minimum should be l+1  
new_d = zeros(size(d))-1.e3  
  
  
for i = start_point:n-1  
    i  
    x = t(i-l : i+l);  
    y = d(i-l : i+l);
```

```
p = polyfit(x,y,deg)

my_p(i-start_point+1,:) = p;

new_d(i) = polyval(p, t(i));

y_est = polyval(p,x);

plot(t,d); hold on

%plot(x,y);

plot(x,y_est,'r.')
plot(t(i),new_d(i),'g*')

pause

hold off

clear p

end
```

```
clear i

for i = n-l+1:n

[i i-l n-i n-l+1]

x = t(i-l : n);

y = d(i-l : n);

p = polyfit(x,y,deg)

my_p(n-l+1,:) = p;

new_d(i) = polyval(p, t(i));

y_est = polyval(p,x);
```

```
plot(t,d); hold on  
%plot(x,y);  
plot(x,y_est,'r.')  
plot(t(i),new_d(i),'g*')  
pause  
hold off  
clear p  
end
```

```
hold off
```

```
figure(11);  
plot(t,d)
```

```
figure(12);
```

```
plot(t,d)
```

```
hold on
```

```
plot(t,new_d,'r.')
```

```
figure (13)
```

```
range = find(new_d > -1.e3)  
plot(t(range),new_d(range),'g!')
```

APPENDIX C: Camera Calibration

```
clear all
```

```
clc
```

```
% Create a set of calibration images.
```

```
images = imageSet(fullfile(toolboxdir('cameracalib'), 'check'));
```

```
imageFileNames = images.ImageLocation;
```

```
% Detect calibration pattern.
```

```
[imagePoints, boardSize] = detectCheckerboardPoints(imageFileNames);
```

```
% Generate world coordinates of the corners of the squares.
```

```
squareSize = 10; % millimeters
```

```
worldPoints = generateCheckerboardPoints(boardSize,squareSize);
```

```
% Calibrate the camera.
```

```
[params, ~, estimationErrors] = estimateCameraParameters(imagePoints,worldPoints);
```

```
figure;
```

```
showExtrinsics(params, 'CameraCentric');
```

```
figure;
```

```
showExtrinsics(params, 'PatternCentric')
```

